# POLITECNICO DI TORINO

Department of Mechanical and Aerospace Engineering

MSc Thesis
in Automotive Engineering

# Development of simplified vehicle models for impact to barrier

**Tutor**

Prof. Eng. Alessandro Scattina

**Candidate**

Alessandro Ravedati

December 2023

# Acknowledgments

I cannot deny that this course of study was a path without difficulty and fatigue but, at the end of these five years, I can say that it has allowed the formation of my person both in the professional and character sphere by revealing to myself a tenacity that even I did not know to have.

I therefore want to thank all the people who have been by my side during this journey and who have supported me in the most difficult moments, in which they were able to listen to me patiently or they had the sensitivity to leave me in silence with my thoughts. Special thanks go to my mom, my dad, my brother and all my family who have made sacrifices to help me over the years. I also want to thank all my friends and my girlfriend who allowed me to distract myself from my studies by spending carefree moments.

A sincere thanks goes to Professor Scattina for his availability and professionalism that allowed me to complete my education as an engineer. I would also like to thank Dr. Damijan Markovich for the stimulating collaboration he has carried out with us over the past months and the hospitality showed during the visit to the JRC in Ispra. My thanks also go to my colleague Annibale, with whom I was sincerely happy to collaborate in this thesis work.

Alessandro

December 2023

# Abstract

This thesis is the result of the collaboration between the Politecnico di Torino and the Joint Research Centre (JRC) which aims to verify the reliability and improve the modeling of a N2/N3 category FEM vehicle model for testing security barriers with an anti-terrorist purpose. Further validation of the vehicle model will be carried out by reproducing a real experiment in a simulation of an impact between a N3C vehicle model and a bollard. An analysis will then be carried out on studying the influence that the relative position of the bollard barrier has during the impact; the objective is to analyze how the main structural components behave in absorbing the impact. In preparation to this work, a comparison between LS-Dyna and Europlexus software was performed; this activity was made comparing results obtained with LS-Dyna versus those obtained on Europlexus on the same case of study. This research was focused on the investigation of the different contact formulation and how the contact stiffens scale factors in LS-Dyna can affect the results.

# Index

## List of Figures

## List of Tables

# 1 Introduction

The main objective of this thesis is to show the work done by the Politecnico di Torino in collaboration with the Joint Research Centre (JRC) [1]; in terms of virtual simulations that recreate the impact between a FEM vehicle model and a security barrier. The main purpose is to test the reliability and improve the modelling of a FEM vehicle model of the N2/N3 category by simulating impact conditions against barriers used for anti-terrorism protection of public spaces. The vehicle model will be tested through explicit FEM simulations carried out on LS-Dyna R12 SMP software version. The model will first be subjected to a further validation that reproduces a real-life experiment of impact against a security barrier; after the validation, a sensitivity analysis on the influence of the barrier position with respect to vehicle impact will be performed; particular attention will be paid to the study of the influence that some structural components of the vehicle have in absorbing the impact.

A second contribution that the Politecnico di Torino has made in this collaboration concerns the validation of Europlexus [2], a FEM software used by the Joint Research Centre. In fact, the first part of the thesis (Chapters 2 and 3) focuses on the comparison analysis of the results obtained with LS-Dyna versus those obtained on Europlexus with the same simulation set up. To better understand the differences between the two software, the comparison is performed on two simple cases: the first involves the shock of a squared tube against a rigid flat wall while the second involves a tube crushing against a rigid flat barrier. The work is mostly carried out studying the results obtained with different contact formulations in LS-Dyna and the parameters that acts directly on the contact, especially the linear scaling factors of the contact stiffness.

In the next paragraphs there will be a brief discussion on anti-terrorism barriers with a specific attention to the bollard vehicle barrier. Moreover, an introduction to the LS-Dyna contacts theory will follow to allow a better understanding of the topics covered in Chapters 2 and 3.

## 1.1 Vehicle barriers: the bollard

Terrorist attacks often target critical public spaces and infrastructures which are characterized by limited protection measures. From the recent years several terrorist attacks aimed unprotected places by means of ramming vehicles that are driven at high speed against the public to maximize human casualties or are used to transport an improvised explosive device (IED) close to a facility [3]. There is therefore a growing need for designing and implementing an approach that supports the selection of simple and effective perimeter protection measures. These barriers should be specifically designed and capable of stopping an ill-intentioned vehicle; they are placed across roadways and passages and can be active or passive, permanent or temporary and come under various technical and commercial names as bollards, wedge barriers, beam barriers, concrete Jersey barriers, ha-ha barriers etc. The process of vehicle barrier selection is shown in Figure 1.

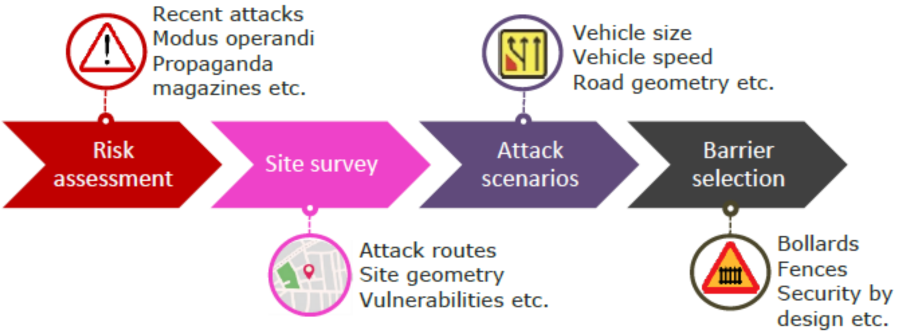

*Figure 1 - Selection approach for anti-ramming vehicle barrier*

For selecting appropriate mitigation measures, several parameters need to be taken into account like velocity and mass of the vehicle and as a consequence its kinetic energy. The main objective of the security barriers is to absorb the threat vehicle's kinetic energy and halting its penetration to the protected zone. In fact, in the analysis carried out in the Chapter 4, regarding the impact simulations between the N3C vehicle model and the bollard, one of the main results of the analyses concern the kinetic energy and the momentum of the vehicle during the impact. Vehicle barrier solutions can be divided into two broad categories regarding their operation: passive (static) and active (moveable). They differentiate in shape, size, material and scope; they can be made of concrete, steel, rock, wood or any other stiff material that can effectively sustain the impact of a moving vehicle. As mentioned, there are many types of vehicle barriers but in this brief discussion will be described in detail the bollard, which is used as a barrier both in the validation and in the sensitive analysis on the barrier position in Chapter 4. The bollard is present in the market with either a passive (static) and an active (movable) version.

- Passive bollards (Figure 2): they are not equipped with moving parts and can absorb the impacting energy through their proper foundation. They constitute one of the most commonly used solutions for limiting the access of unauthorized vehicles in pedestrian areas, city centers and street pavements. They are usually fabricated from steel, reinforced concrete or a combination of the two materials (concrete core surrounded by a steel casing). Their narrow form and small size make them less intrusive in comparison with other solutions. Their performance also depends on their foundation depth and size. Large foundations may be in conflict with underground utilities, so modern innovative solutions equipped with shallow bases are available, requiring smaller penetration depths [3].

*Figure 2 - Static bollard*

- Active bollards (Figure 3): the retractable bollards during their operation should remain in a raised position and can be lowered to allow vehicle entrance after completion of the screening process. They can be either manually lowered, which is common in case of infrequent traffic, or by using a hydraulic or pneumatic unit, such as in site entrances with heavy traffic requirements. One of their greatest advantages is the fact that they permit pedestrian entry independently of their position (raised or retracted), but are usually an expensive option as they require deep and wide foundations [3].

*Figure 3 - Retractable bollard*

## 1.2 Contacts in LS-Dyna

In LS-Dyna software, a distinction is made between slave nodes and aster segments in the definition of contact (sliding or impact) between surfaces. The slave nodes are the nodes of the part that moves and makes contact with the fixed part that is defined as Master. Contact is then defined by identifying what locations are involved in a potential penetration of a slave node through a master segment [4]. A simplified diagram of the slave-master distinction is shown in Figure 4.

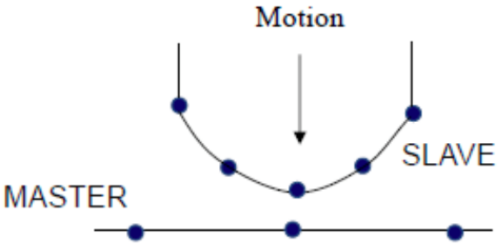

*Figure 4 – Slave-master distinction*

In LS-Dyna the method used for handling the contact between surfaces is the penalty-based method. In the case of a penalty-based contact, when a penetration is found, a force proportional to the penetration depth is applied to resist and eliminate the penetration [4]. This method consists of placing normal interface springs between all penetrating nodes (slave nodes) and the contact surfaces (master). The virtual springs stiffness is used to resist the penetration of the salve nodes into the master ones. The springs are subjected only to an elastic compression in the normal direction [5]. A representation of this method is observable in Figure 5.

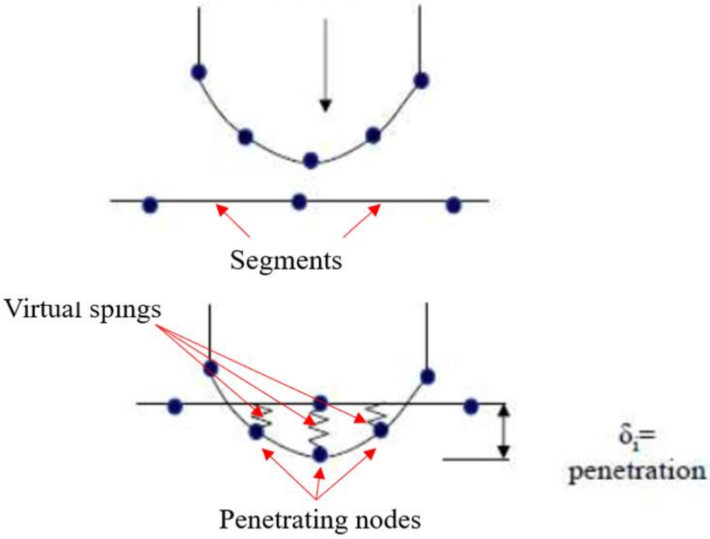

*Figure 5 - Penalty based method*

Since the contact treatment is represented by linear springs between the slave nodes and the master segments, the stiffness of these springs will determine the force that will be applied to the slave nodes and the master nodes. In LS-Dyna there are three methods of calculating the contact spring stiffness: the Standard penalty formulation (SOFT = 0), the Soft-constraint penalty formulation (SOFT = 1) and the Segment-based penalty formulation (SOFT = 2) discussed below [6]. Since the SOFT=1 will be never used in this presented thesis work, it will not be further discussed.

**Standard Penalty Formulation (SOFT = 0)**

This method is the default method and uses the size of the contact segment and its material properties to determine the contact spring stiffness and correspond to the SOFT parameter equal to 0. As this method depends on the material constants and the size of the segments, it works effectively when the material stiffness parameters between the contacting surfaces are of the same order of magnitude [6]. The calculation of the contact stiffness depends on the type of element.

For Solid elements the contact stiffness is calculated with the Equation 1:

$$k = \frac{\alpha K A^2}{V}$$

*Equation 1*

For Shell elements the contact stiffness formulation is shown in the Equation 2:

$$k = \frac{\alpha K A^2}{\max shell\ diagonal}$$

*Equation 2*

In the Equations 1 and 2 $k$ is the contact stiffness, $K$ the material bulk modulus, $A$ the segment area and $\alpha$ the contact stiffness scale factor (SFS). Regarding this last parameter it is a linear scale factor that allows to directly act on the contact stiffness by increasing or decreasing it.

In LS-Dyna software this scale factor is found within the Card "CONTACT_AUTOMATIC_SURFACE_TO_SURFACE" with the name SFSA (for the master part) and SFSB (for the slave part). During the analysis described in Chapters

2 and 3, the influence of this parameter on the simulation results will be deeply analyzed.

**Segment-based Penalty Formulation (SOFT = 2)**

SOFT=2 involves a segment-based contact algorithm which has its origins in Pinball contact method developed by Belytschko [6]. With this contact algorithm, contact between segments is considered rather than using the usual node-to-segment treatment. A segment is the face of an element included in the contact; in fact, LS-Dyna converts the surface defined by 3 or 4 nodes into segments during a contact analysis; as a consequence, the segment corresponds to the face of a 4-node shell or a 3-node shell or a side of a solid [7]. In Figure 6 it can be observed a schematization of the segments.

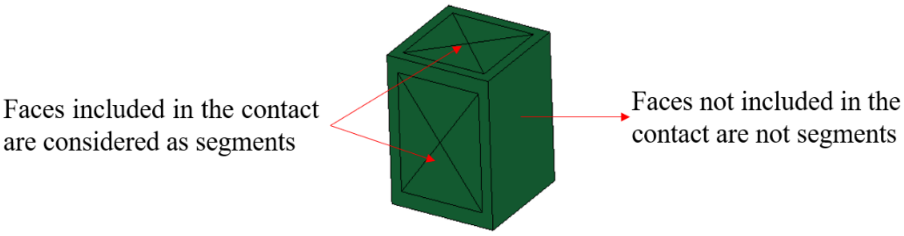

*Figure 6 - Segments diagram*

When two 4-noded segments come into contact, forces are applied to eight nodes to resist segment penetration. This treatment has the effect of distributing forces more realistically.

The contact stiffness is evaluated with the Equation 3:

$$k_{cs}(t) = 0.5 \cdot SLSFAC \cdot \begin{Bmatrix} SFS \\ or \\ SFM \end{Bmatrix} \left( \frac{m_1 m_2}{m_1 + m_2} \right) \left( \frac{1}{\Delta t_c(t)} \right)^2$$

*Equation 3*

In the Equation 3 $k_{cs}$ is the contact stiffness, *SLSFAC* is a scale factor for sliding interface penalties (defaulted 0.1) and SFS and SFM are respectively the slave and master contact stiffness scale factors which correspond to SFSA and SFSB in the contact card. The parameters $m_1$ and $m_2$ are the segment masses and $\Delta t_c$ is the Contact Time Step which is set to 1.05 ×$\Delta t$ where $\Delta t$ is the initial solution Time Step. If during the calculation, $\Delta t$ rises above $\Delta t_c$, then $\Delta t_c$ is reset as 1.05 times the current solution [6].

# 2. Tube shock case

The main objective of this analysis is the comparison between two different software in terms of explicit simulations with the Finite Element Method. In particular, the comparison took place between the LS-Dyna (LSD) and the Europlexus (EPX) software, used by the JRC. To have a more effective comparison between the two software, it was decided to compare them on a very simple model. In this way it was possible to better analyze the similarities and differences in terms of the results.

The first case analyzed concerns an elastic steel tube with a square section that moves at a fixed speed against a rigid flat barrier. After the impact the tube bounces and moves upward in the opposite direction. The comparison of the results is done in terms of the internal, the kinetic, the total energy and the momentum along the z-axis. It was decided to analyze these results because they correspond to the physical components that allow to analyze in details an impact between parts.

## 2.1 Model set up

As previously mentioned, the model is made up of two elements: a tube (the red part) with a square section and a flat barrier (the blue part) also square in shape that is shown in Figure 7.

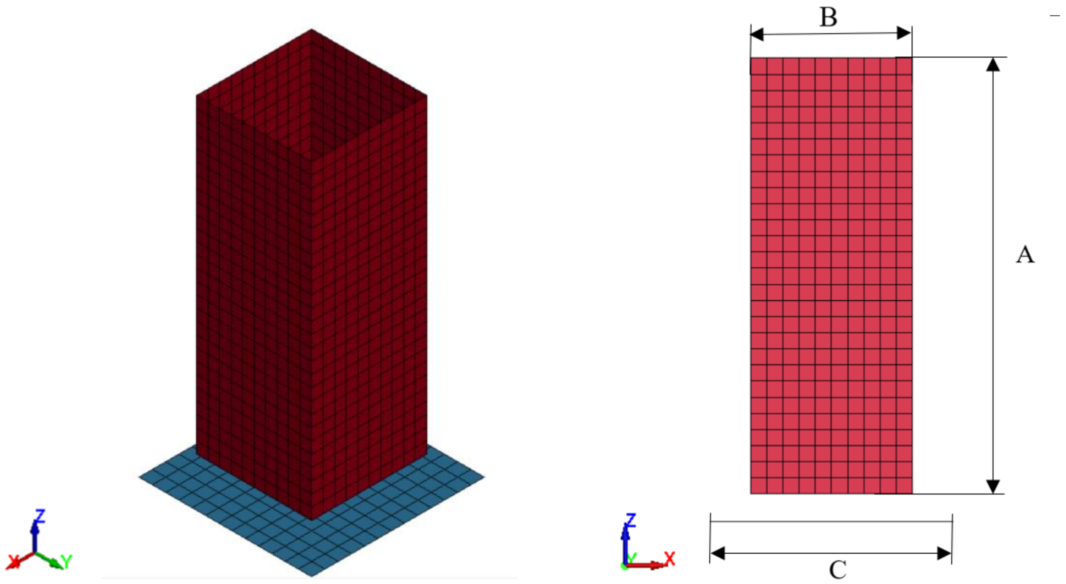

*Figure 7 - Model configuration*

The dimensions of the two components are summarized the in Table 1:

*Table 1 – Tube and barrier dimensions*

| Dimensions (mm) | TUBE | BARRIER |
|---|---|---|
| Height | 270 (A) | - |
| Length | 100 (B) | 150 (C) |
| Width | 100 | 150 |
| Thickness | 1 | 1 |

As regards the mesh, the two components were modelled with shell element configuration and, regarding the mesh size, two different mesh sizes for the two components were used:

- Tube: 10 mm
- Barrier: 11.5 mm

This choice was due to the fact that by using two meshes with identical dimensions at the moment of impact the tube's elements could have overlapped perfectly on the external edges of the barrier elements that came into contact. It is advisable to avoid this situation since it could compromise the results of the simulation. The element formulations used are:

- Tube: F16 (Fully integrated shell element)
- Barrier: F2 (Belytschko-Tsay formulation) [6]

As regards the materials, both the tube and the barrier are made of steel, in particular the tube has been assigned an elastic property while the barrier has been defined as a rigid part and consequently not subjected to deformations. The characteristic values of the material used in the model are listed in the Table 2.

*Table 2 –Tube and barrier material properties - steel*

| | |
|---|---|
| Density (kg/m$^3$) | 7830 |
| Young’s modulus (GPa) | 200 |
| Poisson’s ratio (-) | 0.3 |
| Yield stress (MPa) | 207 |
| Effective plastic failure limit (-) | 0.75 |

The Figure 8 shows the stress - plastic strain curve of the material, theta has been used in the model setup of the simulation.

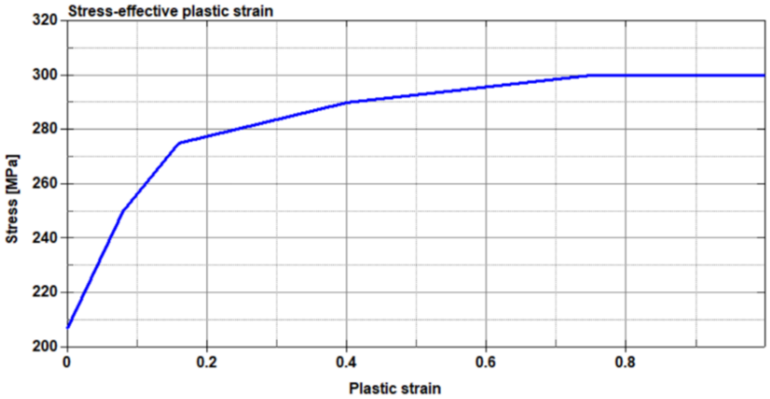

*Figure 8 - Material stress - plastic strain curve*

Concerning the boundary conditions, the model has been set in this way: a speed of -10 m/s was imposed on all the nodes of the tube towards its longitudinal axis (Z axis); as far as the barrier is concerned, it has been completely constrained by locking all the six d.o.f.. The total simulation lasts 10 ms.

## 2.1.1 Contacts set up

Once the model set up was completed, it was necessary to define the contact between the tube and the rigid barrier. In particular, the parameters that has been defined in the contact card are those relating to the Contact Penalty Formulation (SOFT) and the Contact Stiffness Scale Factors (SFS). For more information see Chapter 1, paragraph 1.2.

In particular two different Contact Penalty Formulation are analyzed:

- Standard penalty formulation: SOFT 0
- Pinball Contact Penalty Formulation: SOFT 2

For each of these two different Contac Penalty Formulations, different values of Contact Stiffness Scale Factors were analyzed in order to act directly on the stiffness of the contact. In this way it was able to obtain a series of results, corresponding to different combinations between SOFT and SFS, useful for comparing with the results coming from the EPX software. It was also possible to observe which configurations were more consistent with the results coming from EPX and which were less. The values assigned to the SFS parameters were chosen in a range between 0.5 and 4; between these values only the ones that brought greater changes in the results will be shown in the following analysis; the different configurations of SFS and SOFT are listed in Table 3.

*Table 3 – SOFT and SFS configuration*

| Case studied | SFS values | | |
|---|---|---|---|
| SOFT 0 | 0.5 | 1 | 2 |
| SOFT 2 | 1 | 2 | 4 |

## 2.2 Results comparison

Since the objective of this study is the comparison between the results coming from simulations obtained on LS-Dyna with those coming from EPX, the results obtained with the EPX software were provided with two different contact configurations: liaj 0 and liaj 1. They correspond to two different contact stiffness configurations in particular liaj 1 corresponds to the default configuration while liaj 0 corresponds to the configuration of maximum stiffness. The results were extracted and studied are:

- Internal energy
- Kinetic energy
- Total energy
- Z momentum

### 2.2.1 Influence of Standard Penalty Formulation (SOFT 0) and Contact Stiffness Scale Factors (SFS)

**Internal Energy – SOFT=0**

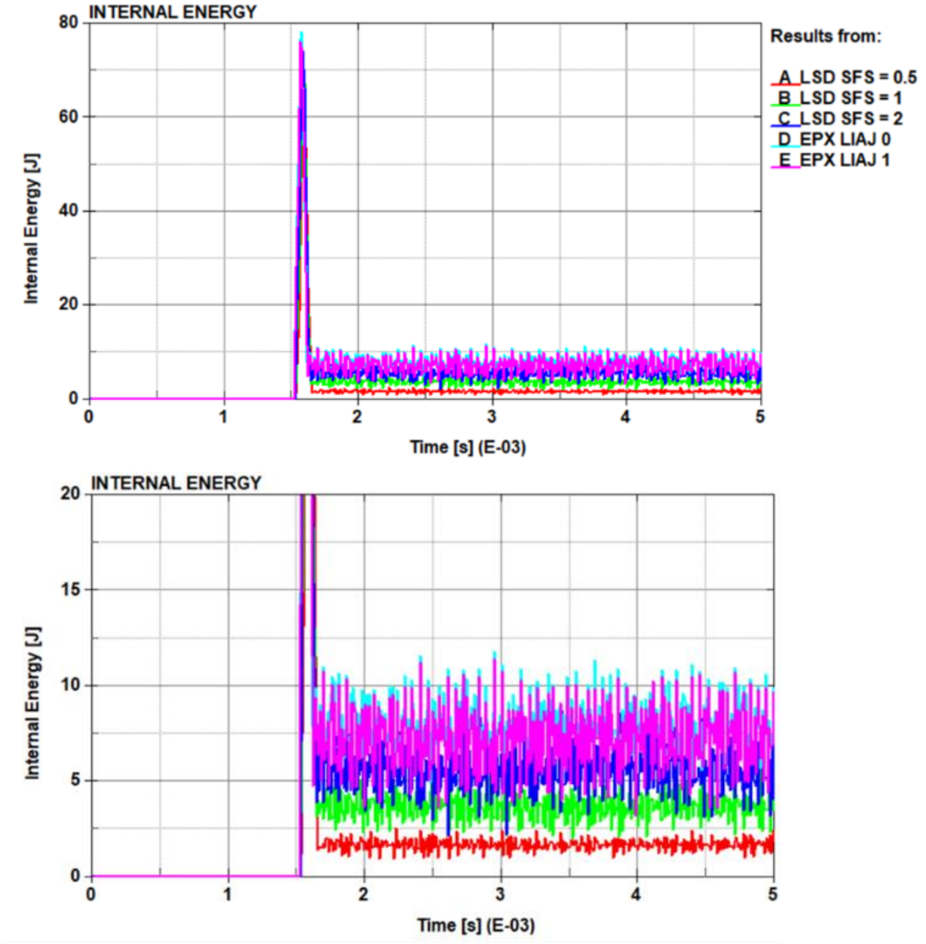

*Figure 9 - Internal energy comparison - SOFT=0*

The Figure 9 shows the trends of the internal energy registered in the different simulations carried out in LS-Dyna. The curves are compared with the ones obtained from the EPX simulations. Looking at the graph it can be seen that the LS-Dyna and EPX curves present similar and consistent trends each other. Analyzing the results, it can be observed that before the impact the internal energy of the tube was equal to 0 J. At the moment of the impact (1.6 ms) the internal energy undergoes a peak which stands between 70 and 80 J. This peak is explained by the fact that the internal energy is the measure of the energy absorbed by the tube during its deformation and therefore at the moment of impact. In this case the tube is made of an elastic material and consequently it does not deform itself permanently (no plastic deformation). In fact, it tends to regain its original shape. For these two reasons, after the peak recorded during the impact with the barrier, the tube bounces and its internal energy tends to return to the initial value (0 J). From the curves relating to the different SFS values it can be observed that as the value of the SFS increases the value of the internal energy increases as well. This means that the growth in value of the energy is caused by the increment the contact stiffness. To understand the reason for this trend, refer to the Chapter 1, paragraph 1.2 on the contact method used by LS-Dyna. In fact, in the case of penalty-based contact method, a force, proportional to the penetration depth and to the contact stiffness is applied to the penetrating nodes to resist and eliminate the penetration. If the scaling parameter is incremented, the contact stiffness increases linearly. By rising the contact stiffness, the algorithm will impose greater force on the penetrating nodes, reducing their penetration depth. The increase of the force applied to the penetrating nodes translates into greater deformation of the elements. A greater deformation of the elements explains the internal energy value increase as the SFS increases. A confirmation of what is explained above can be found also in A. Spizzirri's thesis "Development of simplified vehicle models for barrier impact" in Chapter 2, paragraph 2.3.4 where is also analyzed a tube impacting and bouncing perpendicularly on a rigid barrier. The simulations are carried out under the same conditions as those described above. The only difference is the plastic material from which the tube is made. In A. Spizzirri thesis the plastic strain values can be observed and they increase as the SFS values increase.

As for the comparison with the curves calculated by EPX software, they show the same trend as those calculated by LS-Dyna. It is observed that the two curves liaj 0 and liaj 1 are very similar to each other and are almost overlapping. They are most similar to the configuration with SFS = 2 calculated in LS-Dyna.

### Kinetic Energy – SOFT=0

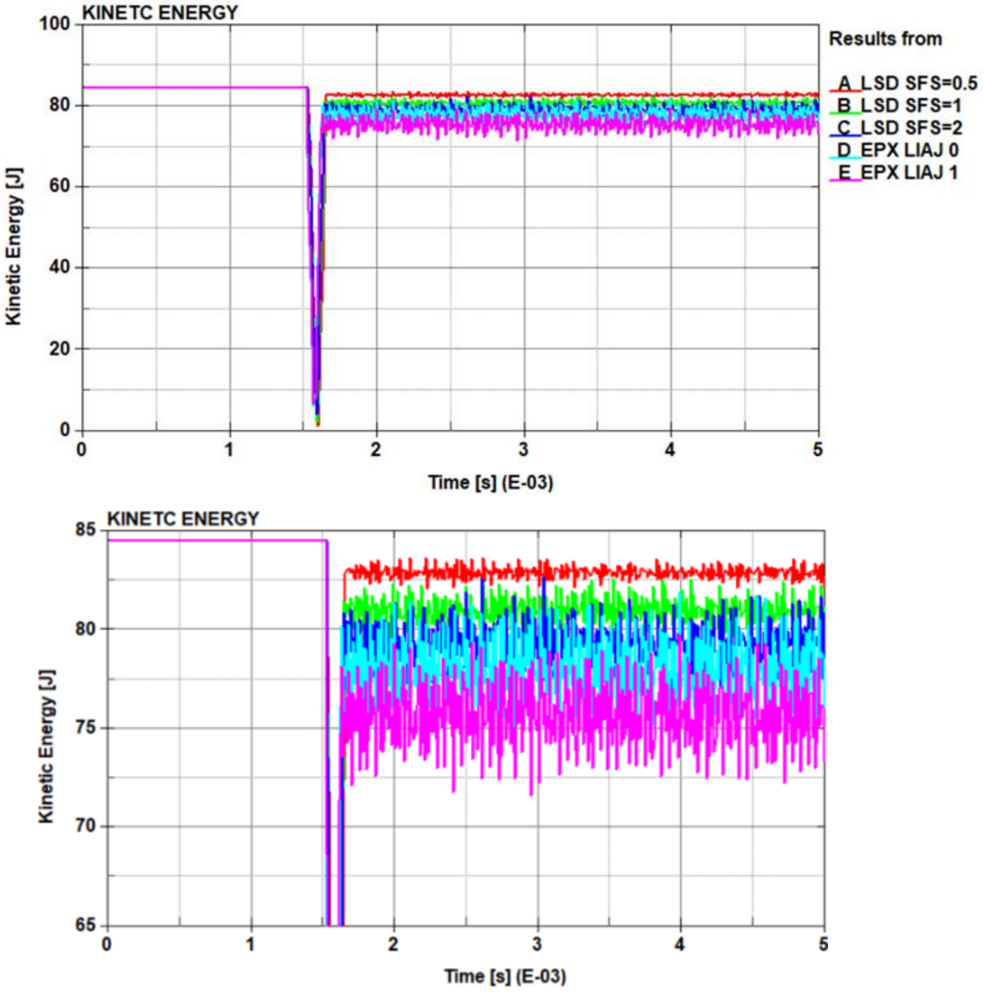

*Figure 10 - Kinetic energy comparison - SOFT = 0*

Figures 10 show the trend of kinetic energy curves and a magnification of them. As it can be immediately observed, the trend of kinetic energy appears specular to the trend of the internal energy. This specular trend can be associated with the principle of energy conservation. Before the impact zero internal energy is present since the tube is undeformed while a positive and constant kinetic energy is present. This is given by the fact that the tube moves with constant velocity before the impact against the barrier. At the moment of contact, the kinetic energy registers a dramatic reduction until it reaches the value of 0 J since for an instant of time the tube is stopped because it is arrested by the barrier. At the same time the internal energy undergoes the opposite effect since the tube is subjected to a sudden deformation. Similar to what happened to the internal energy, after the collision, the value of the kinetic energy tends to recover the same value before the contact and the tube bounces back in the opposite direction. Again, the effect of contact stiffness and thus SFSs values have considerable effect on the different trends of kinetic energy. It can be seen that by increasing the value of SFS, the value of kinetic energy decreases. This effect is related to the previous explanation: the increase of the contact stiffness implies more deformation to the elements. By the principle of conservation of energy, if the deformation increases the internal energy will increase and as a consequence the kinetic energy will decrease. Another aspect that is observable in both the kinetic and the internal energy graphs is the presence of oscillations after impact with the barrier. This phenomenon can be explained by observing in slow motion a body impacting and bouncing perpendicular to another rigid body. It will, after the impact, undergo into a deformation (in such case elastic) which will propagate within the body. The propagation of the deformation results in a series of alternating contractions and elongations. These deformations cause strain oscillations that alternate between compression and tensile stress conditions. As a consequence of that, the internal energy will register oscillations due to the different deformations to which the elements are subjected after impact. Moreover, the kinetic energy will also record oscillations specular to those seen in the internal energy.

In consideration of the curves calculated in EPX, they show consistent trends with those calculated in LS-Dyna. In this case, it is observed that liaj 0 and the SFS=2 configuration of LS-Dyna turns out to be externally similar since the two curves overlap almost completely.

## Z Momentum – SOFT=0

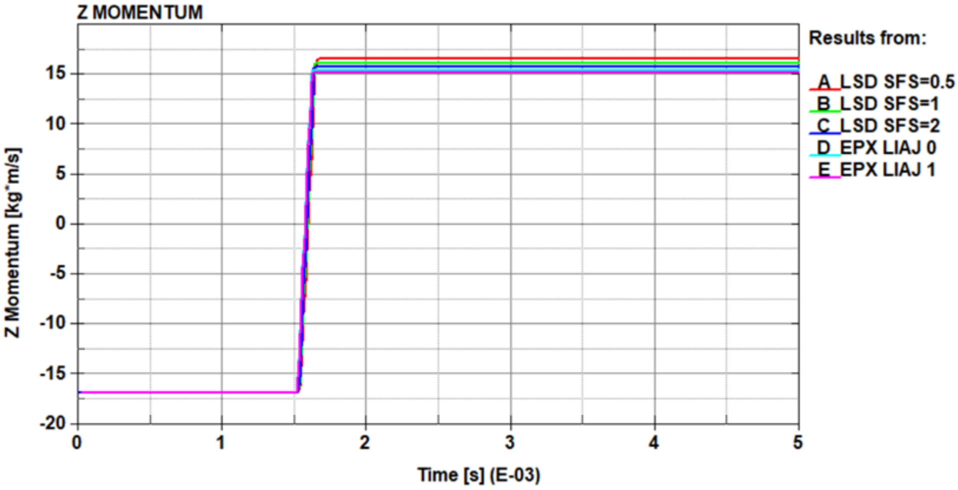

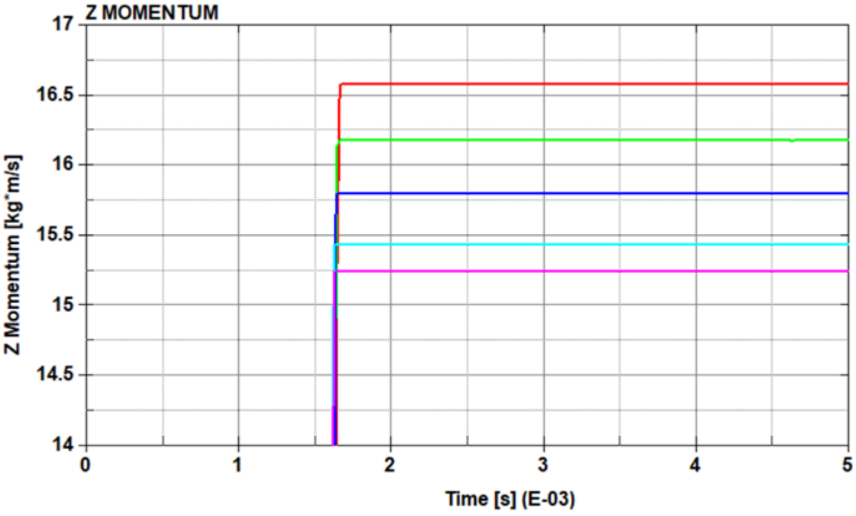

*Figure 11 - Z Momentum comparison - SOFT = 0*

The graphs in Figure 11 shows the curves for the Z momentum and its relative magnification. Analyzing the trend of the graphs, it can be seen that this is symmetrical respect to the time axis. In fact, before the impact (1,6 ms) the Z momentum presents a constant value of -16.9 (kg×m/s) since the tube is moving with a velocity of -10 m/s in the direction of the Z axis. At the instant of impact, the Z momentum curve reaches the value of 0 (kg×m/s) since its velocity is null. After the impact the momentum acquires positive values since its velocity has changed direction. As it can be seen, the momentum does not reach the same value in modulus as it did before the impact. This is caused by the presence of the deformations of the elements. In this case, the momentum presents a similar trend as the kinetic energy: after the impact a decrease in momentum is observed as the SFS increases. The reason for this trend is related to the different deformation of the elements as the contact stiffness changes. Momentum and kinetic energy are closely related and, as seen, an increase in internal energy (increase in deformations) is related to a decrease in kinetic energy and as a consequence also in the tube velocity.

**Total Energy – SOFT=0**

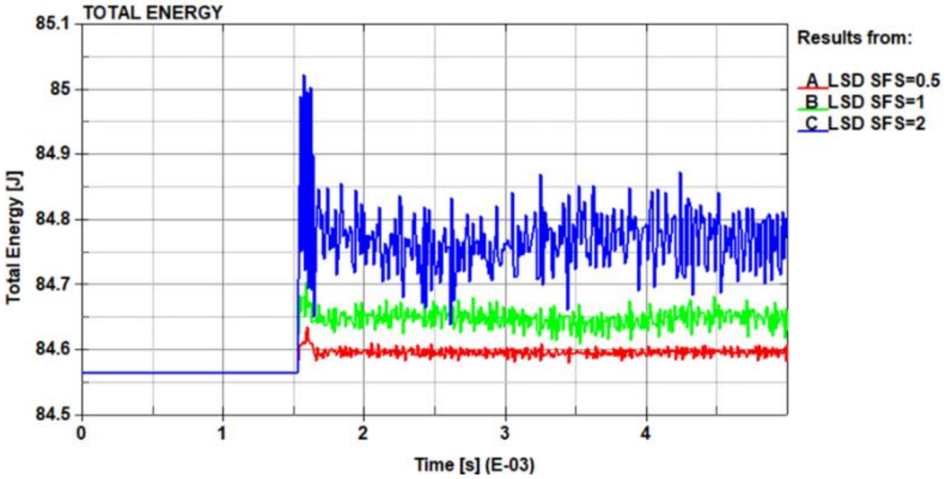

*Figure 12 - Total energy comparison - SOFT = 0*

Figure 12 depicts the total energy curves. In LS-Dyna, total energy is calculated as the sum of internal, kinetic and hourglass energy [6]. In this discussion only internal and kinetic energy have been analyzed up to now, but by observing the total energy graph, considerations can also be made about hourglass energy.

As mentioned earlier an increase in the SFS value is correlated with an increase in internal energy and a decrease in kinetic energy and vice versa. Consequently, it would be expected that the total energy remains constant for the duration of the simulation. However, by analyzing the results shown in Figure 6, it is observed that there is a small difference in the total energy before and after impact. In particular, it is observed that as the SFS value increases, the total energy after impact increases. This behavior can be associated with the variation of the hourglass energy. The hourglass energy is the work done by the forces to resist hourglass modes and it takes away from physical energy of the system. As a consequence, in this case, as the contact stiffness and the deformation of the elements increase, the hourglass energy will increase as well. This trend is related to an increment of hourglass distortion of the elements due to hourglass modes.

## 2.2.2 Influence of Pinball Contact Penalty Formulation (SOFT 2) and Contact Stiffness Scale Factors (SFS)

### Internal Energy – SOFT=2

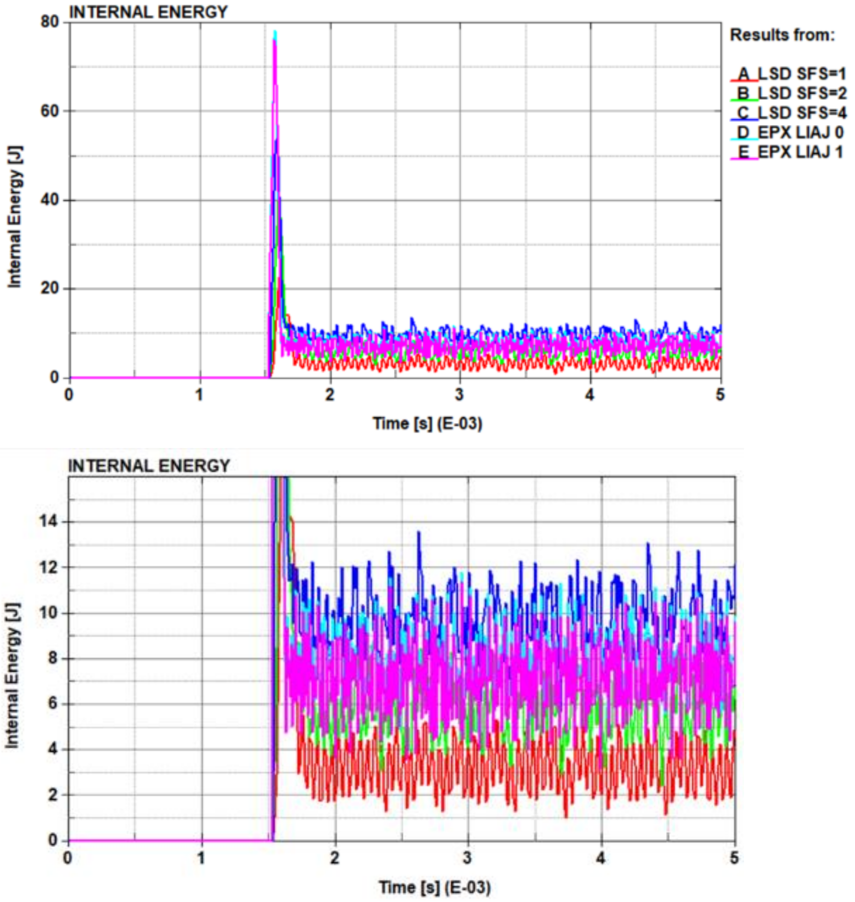

*Figure 13 - Internal Energy comparison - SOFT = 2*

Figure 13 shows the graph of the internal energy and its relative magnification calculated with the Pinball Contact Penalty Formulation (SOFT=2). It is observed how the trend of the curves is very similar to the one recorded with the Standard Penalty Formulation (SOFT = 0). The same correlation between SFS values and internal energy is also noted: the increase of the value of the SFS increases the value of the internal energy and thus also the deformation of the elements. This is a consequence of the fact that the SOFT = 2 formulation also bases its method on the penalty forces, which, in this case, are applied to the segments and not to the nodes as happens for SOFT=0.

With regard to the comparison with the curves of EPX liaj 0 and liaj 1, they tend to overlap with the curve with configuration SFS = 4 calculated in LS-Dyna. From this last observation it can be deduced that by increasing the contact stiffness the results obtained are more similar and consistent with those in EPX.

**Kinetic Energy – SOFT=2**

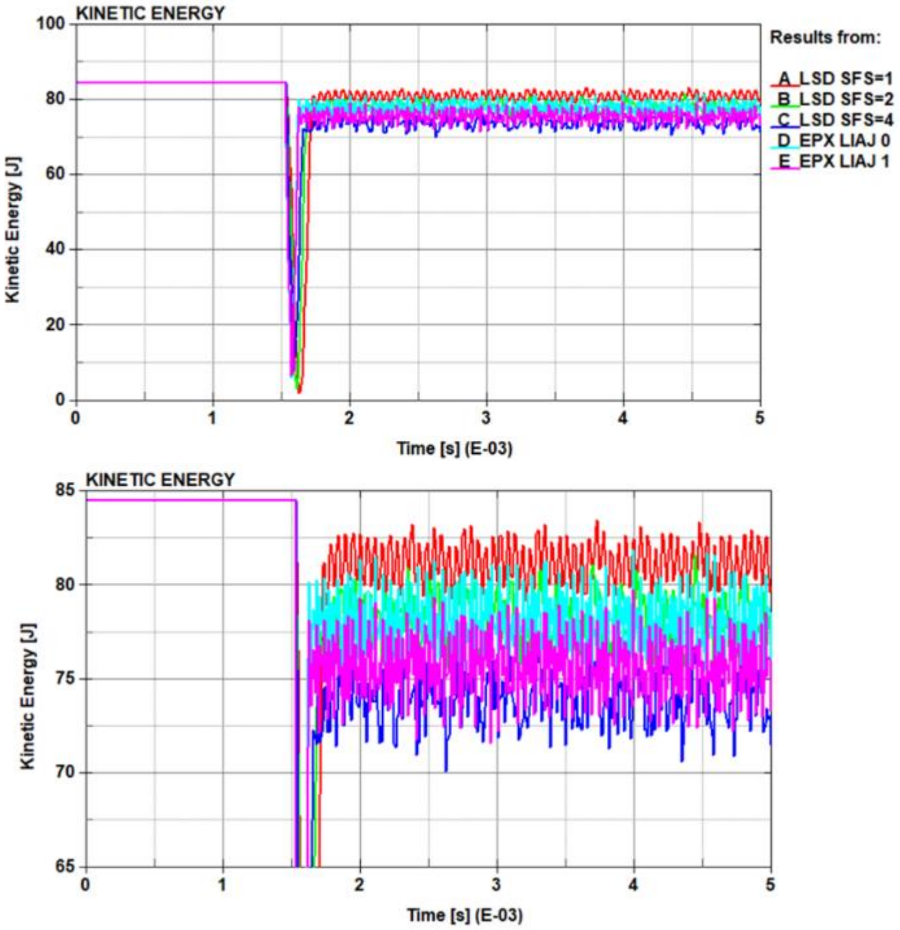

*Figure 14 - Kinetic energy comparison - SOFT = 2*

Figures 14 show the graph of kinetic energy and its relative magnification calculated with the Pinball Contact Penalty Formulation (SOFT=2). Analogous to the case analyzed with the SOFT = 0 configuration, a specular trend to the one of the internal energy is observed. Concerning the relationship between values of kinetic energy and different values of SFS, similar conclusions can be drawn as the ones described in section “Kinetic Energy - SOFT=0".

In this case it is observed that the curve calculated in EPX liaj 1 is almost superimposed on the curve of LS-Dyna presenting the configuration with SFS = 4, the one with higher contact stiffness. Also in this case, the curves calculated with higher contact stiffness turn out to be more consistent and similar to those in EPX.

### Z Momentum – SOFT=2

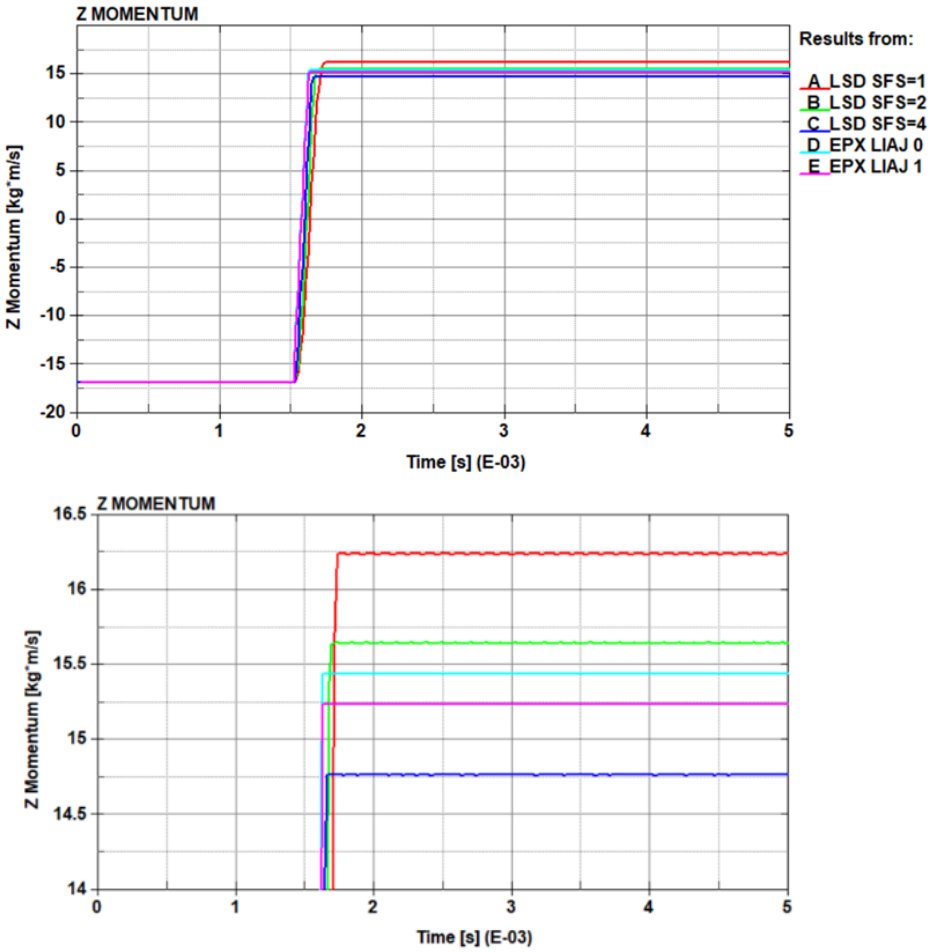

*Figure 15 - Z momentum comparison - SOFT = 2*

As for Z Momentum, its trend can be observed in Figure 15. The trend is the same described in the paragraph "Z Momentum - SOFT=0". As the values of the SFS increase the values of Z Momentum will decrease, in the same way that it was observed for the SOFT= 0 configuration. The motivation for this trend is the same to what described in the paragraph just mentioned.

Regarding the comparison with the curves calculated in EPX it is observable how in this case with the configuration SFS = 4 it can be obtained a value of Z momentum lower than those of liaj 0 and liaj 1; the configuration with SFS = 2 turns out to be more similar and consistent with the curves of EPX in particular way with the configuration liaj 0.

**Total Energy – SOFT=2**

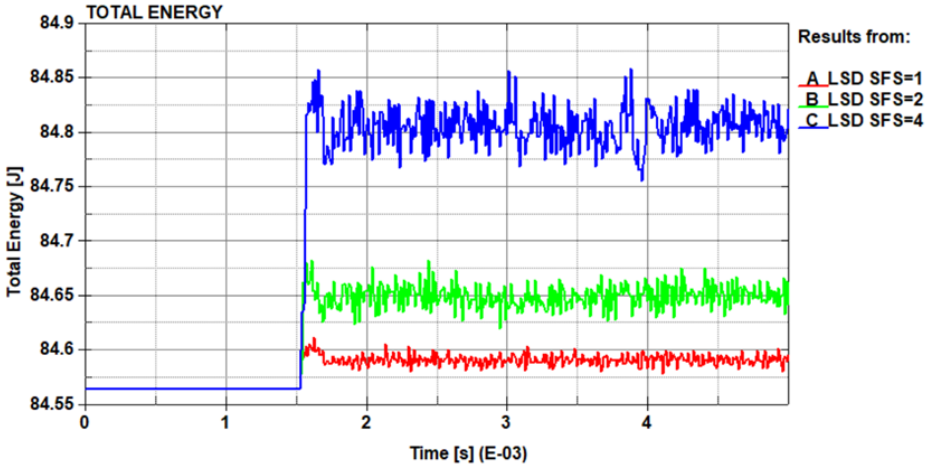

*Figure 16 - Total energy comparison - SOFT = 2*

Regarding the Total energy shown in Figure 16 a trend similar to that described in the section "Total Energy - SOFT=0" is observable. Also in this case, the trend of the total energy is not constant and, after impact, tends to increase as the SFS values increment. The configuration with SFS = 4 presents a significant higher increase in total energy than those obtained with the configuration SOFT = 0. This is due to the fact that by imposing the SFS parameter with a value of 4 the contact stiffness is quadrupled. Such high stiffness resulted in considerable deformation of the elements, which caused a substantial increase in hourglass mode displacement of the nodes and as a consequence in the hourglass energy.

### 2.2.3 Statistical analysis of the results

As observed earlier regarding the internal, the kinetic and the total energy, they show oscillations after the impact. To better compare the LS-Dyna values, with each other and with those obtained with EPX, the average values of all energy results were extracted over the time interval from 2 ms to 5 ms. The average values were used to perform a more analytical comparison between the various contact configurations studied.

*Table 4 – Mean values calculated between 2ms and*

| SOFT = 0 | Internal energy | Kinetic energy | Total energy |
|---|---|---|---|
| LSD SFS=0.5 | 1.68 J | 82.9 J | 84.5 J |
| LSD SFS=1 | 3.67 J | 81 J | 84.65 J |
| LSD SFS=2 | 5.95 J | 78.5 J | 84.75 J |
| EPX LIAJ=0 | 7.73 J | 78.1 J | 85.83 J |
| EPX LIAJ=1 | 7.26 J | 75.7 J | 83.96 J |
| SOFT = 2 | | | |
| LSD SFS=1 | 3.28 J | 81.2 J | 84.59 J |
| LSD SFS=2 | 5.89 J | 78.2 J | 84.65 J |
| LSD SFS=4 | 7.1 J | 77.2 J | 84.8 J |
| EPX LIAJ=0 | 7.73 J | 78.1 J | 85.83 J |
| EPX LIAJ=1 | 7.26 J | 75.7 J | 83.96 J |

Table 4 collects the average values for the configurations calculated with SOFT = 0 and with SOFT = 2. Analyzing the values of the internal energy the lowest value recorded is the one associated with the configuration SFS = 0.5. In fact, it halves the contact stiffness which will reduce the deformation that the elements undergo. Following the same reason, the highest value of internal energy is the one correlated with the highest SFS value analyzed: SFS = 4. The latter is also the value that is closest to the ones obtained with EPX. As previously analyzed, the kinetic energy shows an opposite trend to that of internal energy. In fact, the highest value is the one calculated with SFS = 0.5 while the lowest is the one with SFS = 4. The total energy shows a maximum value with the SFS = 4 configuration, which turns out to be the one closest to the values of liaj 1 calculated in EPX.

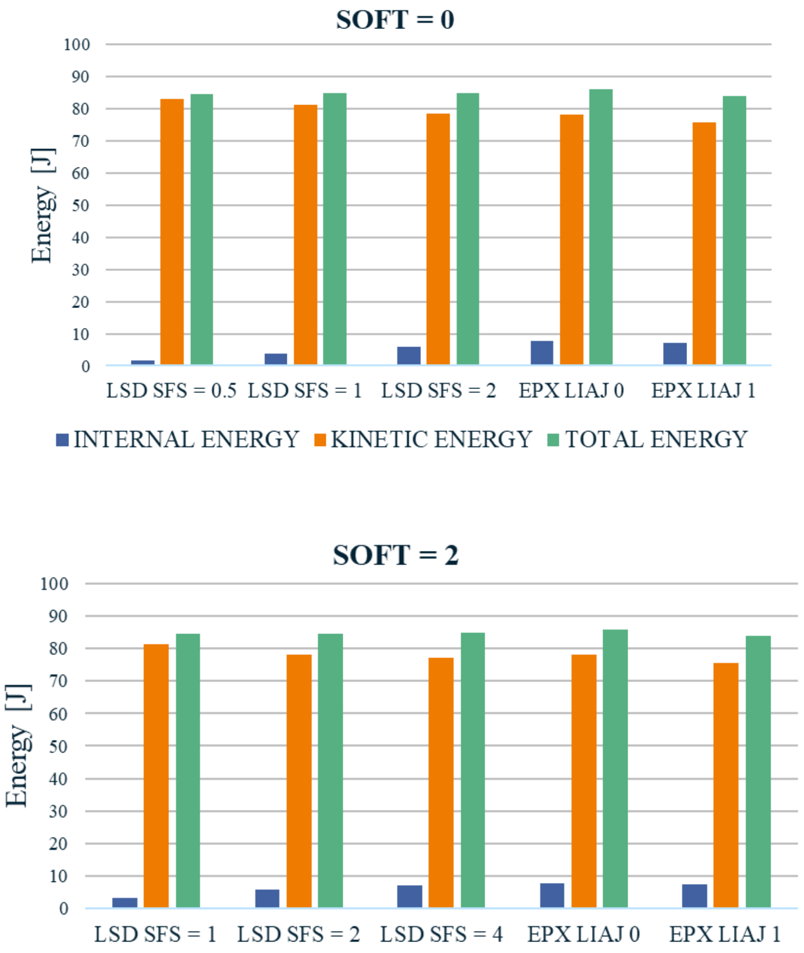

*Figure 17 - Mean values calculated between 2 ms and 5 ms for SOFT = 0 and SOFT = 2*

In Figure 17 it can be appreciated what has been said above through a histogram representation of the calculated mean values. From the histograms it can be appreciated qualitatively how much the scaling parameters affect the different energies. The columns of total energy turn out to have an almost constant height, which is an indication that the variation caused by the SFS values is an order of magnitude smaller than the variations that affect kinetic and internal energy. Regarding the latter two, a clear increasing trend is noticeable for the blue columns while a decreasing trend can be observed for the orange columns as the value of SFS increases. Regarding the comparison between LDS and EPX, a percentage difference between the results was calculated. The percentage difference has been calculated between the energy's values of LS-Dyna and EPX then related to the mean value of the total energy calculated in LS-Dyna. The mathematical formulation used is the Equation 4:

$$\frac{\left(LSD_{energy} - EPX_{energy}\right)}{LSD_{total\ energy}} \cdot 100$$

*Equation 4*

In order to better compare and analyze the values of the percentage differences, they are represented in histograms in Figure 11. Analyzing both graphs it can be observed how as the values of SFS increase the percentage differences tend to decrease.

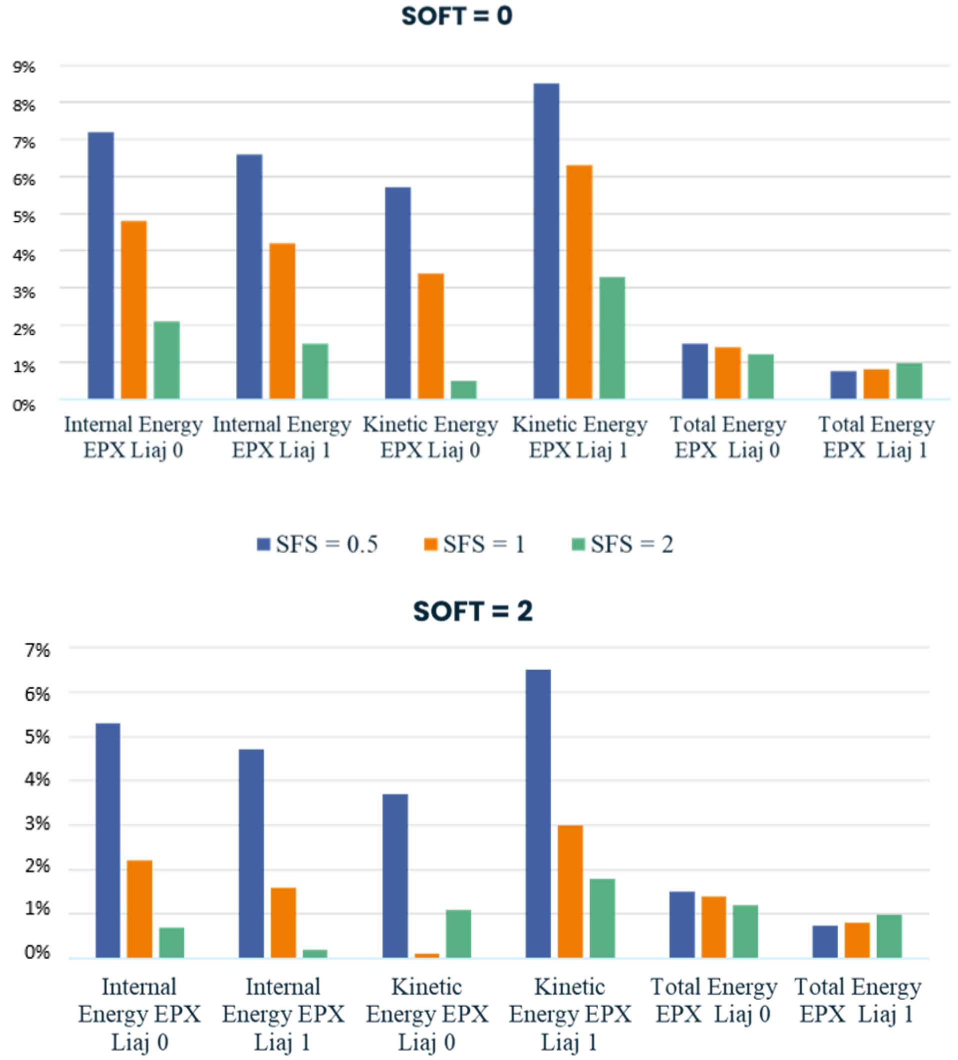

*Figure 11 – Percentual difference EPX values with respect to LSD total energy (LSD-EPX)/ LSD total energy*

Regarding the internal energy, it can be found that the liaj 1 configuration has a lower percentage difference than the liaj 0 configuration for both SOFT = 0 and SOFT = 2. Especially, the lowest percentage difference is recorded between the internal energy with the configuration SFS = 4 and liaj 1. Regarding kinetic energy, on the other hand, it can be seen an opposite trend. Liaj 0 shows lower percentage differences than liaj 1 for both of the two contact penalty formulations. The lowest percentage difference is recorded for the liaj 0 and the SFS = 2 configuration with SOFT = 2.

In conclusion from these tables and this analysis it can be deduced how both contact formulation SOFT = 2 and SOFT = 0 produce consistent and coherent results with those obtained in EPX. It can also be inferred how the SFS parameters allow to obtain results that are extremely similar to those in EPX when they are increased from their default value. In fact, in both contact formulations, the lowest percentage differences are obtained with the highest SFS value.

It can be argued that to obtain results showing a percentage difference of about 2 %, it is necessary to impose SFS value as a minimum of 2. It can also be concluded how the use of the SFS parameter with a value less than 1 results in a significant increase in percentage differences.

## 2.3 Time step and added mass analysis

A second analysis was carried out with the aim of investigating the time step during the tube impact simulation. This analysis, similar to the previous one, is focused on the different influences that the contact penalty formulation and the contact stiffness scale factors have on the time step. As second point, it was analyzed how the internal, the kinetic, the total energy and the added mass varies when a fixed time step is imposed to the simulation. Following this investigation on the fixed time step, it was noted how the added mass changes in relation to SOFT and SFS. As for the contact set up, it is the same as described in the paragraph “2.1.1 Contacts set up”.

### 2.3.1 Influence of Contact Penalty Formulation and Contact Stiffness Scale Factors (SFS) on Time Step Size

**Time step – SOFT = 0**

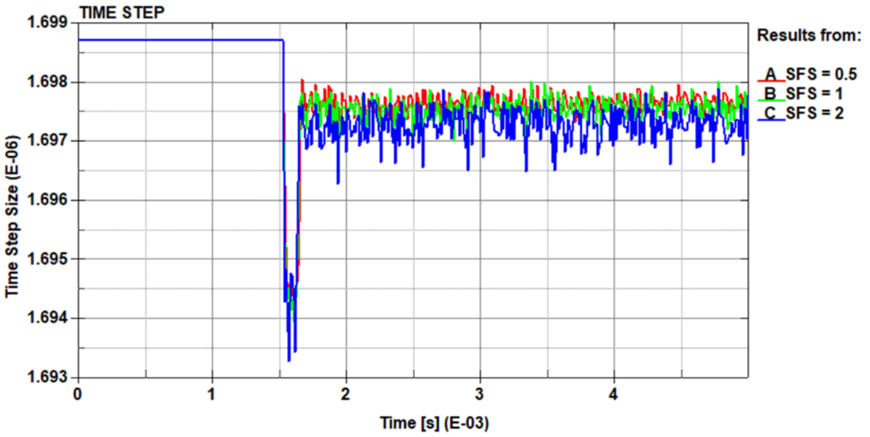

*Figure 18 - Time step size comparison - SOFT = 0*

Figure 18 shows the recorded time step trend of the simulations obtained with SOFT = 0 configuration. It can be noted how the time step trend is not constant but varies during the simulation. In particular, it can be observed how the time step presents a fixed value before the impact and then undergoes a drastic reduction at the moment of impact. After the impact, the time step recovers the same value that had before the impact. Moreover, it can be observed how, after the contact, the time step does not reach the same previous value. In addition, the time step, after the contact, decrease in magnitude as the SFS values increase. To better understand this trend, it is necessary to recall the method that is used in LS-Dyna to calculate the time step size. The time step for shell elements in LS-Dyna is defined as the time required for a shock wave to travel across the smallest distance in an element [6]. It is described by the following equation (Equation 5):

$$\Delta t_e = \frac{L_s}{c}$$

*Equation 5*

In the formula appears the term $\Delta t_e$ which is the time step size, $L_s$ is the characteristic length and $c$ is the sound speed [6]. Especially the speed of sound is calculated according to Equation 6:

$$c = \sqrt{\frac{E}{\rho(1-\nu)}}$$

*Equation 6*

In the Equation 6 $E$ is the elastic modulus of the material, $\rho$ is the material density and $\nu$ is the Poisson ratio. As for the characteristic length for quadrilateral elements, it is defined by Equation 7.

$$L_c = \frac{A_s}{\max\,(L_1, L_2, L_3, L_4)}$$

*Equation 7*

$A_s$ is the area and $L_i, (i = 1 \dots 4)$ is the length of the sides defining the shell elements [6]. Returning to the impact of the tube, its square-shaped elements will deform when they come into contact with the barrier. The tube elements are subjected to deformation due to compressive stress. As a result, the deforming tube elements will tend to assume a rectangular shape. For the same value of area, a deformed element will have a shorter characteristic length than an undeformed square-shaped element. In fact, the segments of the elements of the tube, during the impact, will be subjected to a compression which elongates the horizontal segments and contracts the vertical ones. It will therefore result that the maximum length present in the denominator in Equation 7 will be greater for a deformed element rather than for an undeformed one. Consequently, the characteristic length will be lower for a deformed element than for an undeformed one. According to Equation 5, the time step is directly proportional to the characteristic length of the element. Taking into account that the speed of sound $c$ remains constant, it is observed that the time step decreases in concordance with the deformation of the element.

Thus, looking at the graph in Figure 18 it becomes clear why the time step is drastically reduced at the moment of impact, i.e., the instant when the tube elements deform the most. After the impact, the time step does not reach the value it had before because of the deformations still present in the elements. Regarding the relationship between time step and SFS, a decreasing trend of time step is observed as the value of SFS increases. In fact, this trend is consistent with what was said in the paragraph above in Sections

2.2.1 and 2.2.2. As the value of the SFS increases, the deformation of the elements increases, and therefore the time step, after impact, tends to be at lower values.

**Time step – SOFT = 2**

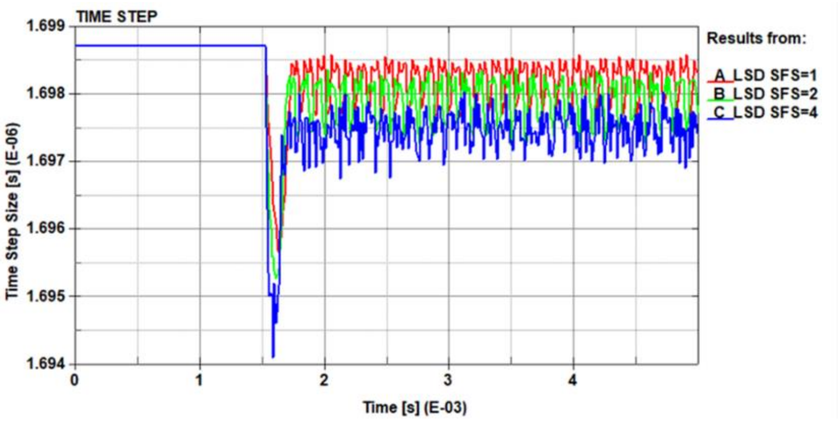

*Figure 19 – Time step size comparison - SOFT = 2*

Figure 19 shows the time step curves related to the SOFT = 2 configuration. For what concern the trend the same remarks as the in the section "Time step - SOFT = 2" remain valid. The main differences are due to a more pronounced distinction of the curves in relation to the different SFS. Indeed, it can be appreciated more clearly how the time step values decrease as the SFS values increase. The three curves are quite distinct both during the peak, at the time of impact, and after it. They also show constant and equal oscillations between them. This difference from the SOFT = 0 case is due to the values of the SFSs, that are more equally spaced (1,2,4).

## 2.3.2 Influence of Contact Penalty Formulation and Contact Stiffness Scale Factors (SFS) on Mass scaling

What was described in the sections 2.3.1 is the time step trend during simulations that is calculated directly by LS-Dyna during a simulation. In fact, the software modifies and updates the time step size in relation to the critical time step. It should be considered that for stable explicit analysis, the current time step should be less than the critical timestep. The critical time step is defined as the minimum time step determined by the ratio of minimum characteristic length of the element and the speed of the sound wave in the specified material (Equation 5). The current time step must be lower than the critical time step because it should not propagate across more than one element in each timestep. The smaller the time step, the more steps it takes to complete the analysis which means longer run time. Like it has been seen in the previous paragraphs as the deformations of the elements increase, the time step tends to decrease consequently. When simulations involve considerable deformations, they may incur a significant increase in computation time. It is therefore possible to impose the minimum time step. The DT2MS is where the desired minimum timestep can be imposed for the simulation. With this approach some artificial mass will be added to any elements which time step drops below the imposed one. In this way, adding the artificial mass to those elements, the time step will be increased to the imposed one value. This process is known as mass scaling. It is necessary to focus the attention to this process by calibrating the DT2MS and the TSSFAC (linear time step scale factor) parameters. Indeed, anytime that the software adds nonphysical mass to increase the time step, the results are affected by that (e.g., $F = m \times a$) [8]. Sometimes the effect is insignificant and, in those cases, adding nonphysical mass is justifiable. Usually, nodal added mass is generally allowed up to 5% of the total mass.

Therefore, to analyze the relationship between added mass, contact penalty formulations and contact stiffness scale factors, a time step with a value higher than the one observed and shown in the section 2.3.1 was imposed. The imposed timestep value is calculated as the product of the parameter DT2MS and its scale factor TSSFAC. A value of DT2MS equal to 1.9 e-06 s is imposed while the parameter TSSFAC has been left at the default value of 0.9. As a consequence of this, the value of the time step will be equal to 1.71 e-06 s. The trend of the imposed time step, shown in Figure 20 will be constant at the value of 1.71 e-06 s throughout the duration of the simulation. Since the value of the imposed time step is higher than the time step shown in Figures 18 and 19, LS-Dyna will start a process of mass scaling on the tube elements.

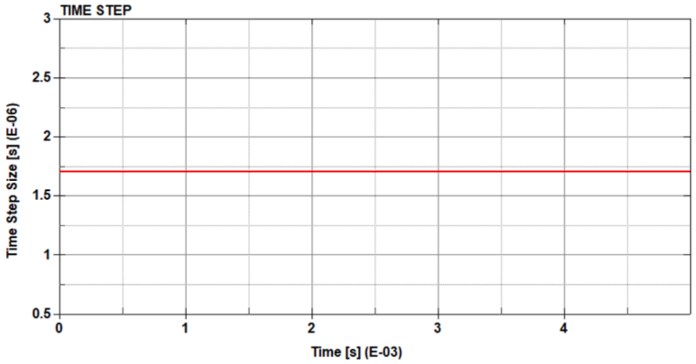

*Figure 20 - Imposed time step*

To facilitate the future explanation, it will be referred to the constant time step imposed by the DT2MS parameter with "fixed time step" while the time step calculated by LS-Dyna during the simulations and, shown in Figures 18 and 19, with “Variable time step”

## Added Mass– SOFT = 0

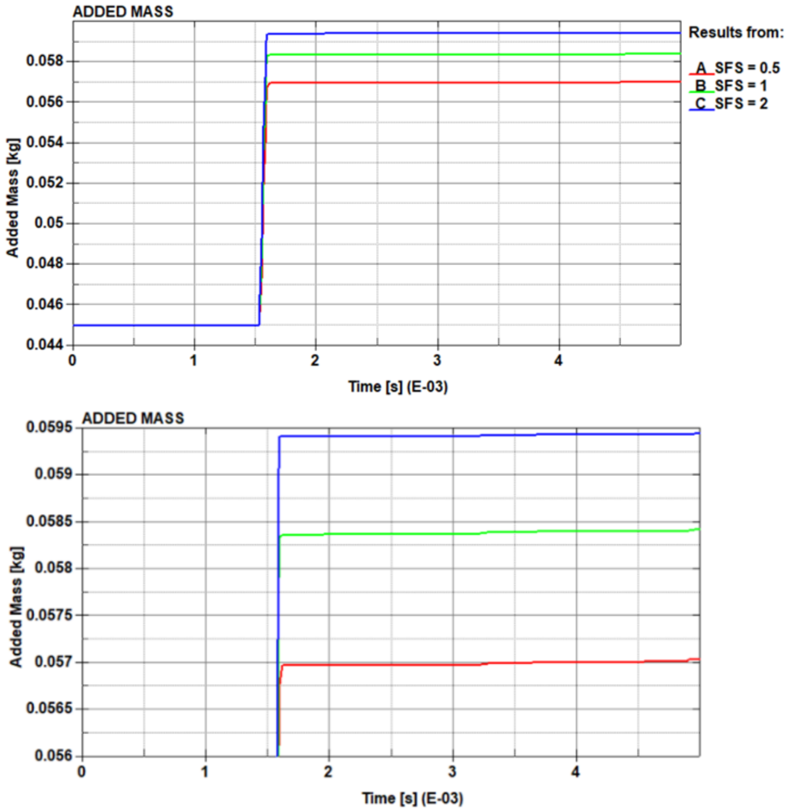

*Figure 21 - Added mass comparison - SOFT = 0*

The graph in Figure 21 shows the trend of the added mass and its magnification in the SOFT = 0 case. It is observed how imposing this value of fixed time step, the mass scaling process starts even before the impact. In fact, it can be seen that before the collision the value of the added mass is not zero. This is due to the fact that the value of the imposed time step is greater than the minimum time step calculated by LS-Dyna. Indeed, looking at Figure 18 the value of the time step before impact is just below the value of 1.699 e-06 s which is slightly less than the value of imposed one (1.71 e-06 s). As a consequence of this, a value of 0.045 kg of artificial mass will be added to the elements of the tube before the impact. At the time of the contact between tube and barrier it is observed that the added mass increases dramatically. This growth is easily explained by the fact that, as seen in section 2.3.1 in Figure 18 and 19 at the instant of impact the time step undergoes a drastic reduction. Consequently, the gap with the fixed time step will increase and LS-Dyna will proportionally increase the amount of added mass to compensate it, as explained in the previous section. After this increase of mass, the time step calculated by the software tends to grow in magnitude again, and the added mass remains constant at the value of 0.0594 kg. This is due to the fact that in the mass scaling process mass can only be added and not removed.

Regarding the relationship between added mass and SFS, it is observed that the increment in the value of SFS leads to an increase in added mass. This trend can be related to what has been said so far: with the growth of SFSs values the deformation of the elements increases and this causes a decrease in the time step as well. With the reduction of the time step the gap with the fixed one increases. As a consequence of that the added mass increases accordingly.

As anticipated earlier, it is necessary to have a closed look at the mass scaling process since the added mass can greatly influence the results. In fact, it is recommended that the added mass should not exceed 5% of the total mass. The Table 5 shows the percentages of added mass calculated for the SOFT = 0 configuration.

*Table 5 – Percetual value of added mass recorded – SOFT = 0*

| SFS value | Added Mass % |
|---|---|
| 0.5 | 3.43 % |
| 1 | 3.5 % |
| 2 | 3.52 % |

It can be seen that for all 3 cases analyzed, the added mass percentage is less than 5% and therefore acceptable.

### Added Mass– SOFT = 2

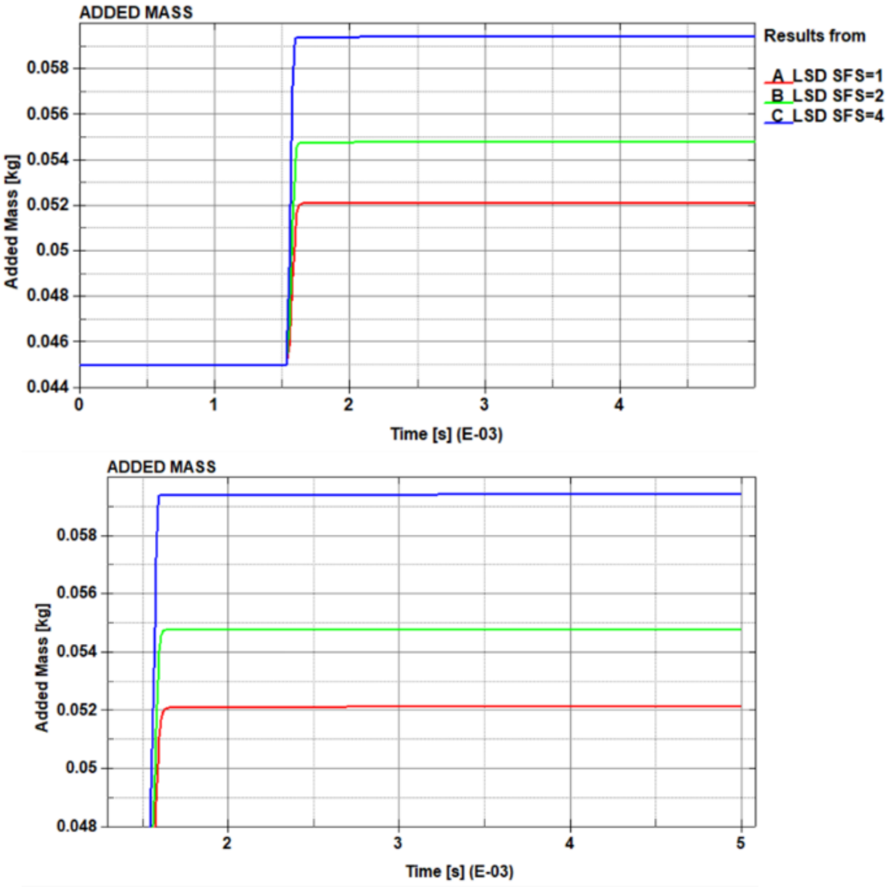

*Figure 22 – Added mass comparison - SOFT = 2*

The graph in Figure 22 shows the trend of the added mass for the SOFT = 2 configuration and its magnification. The trend is similar and analogous to that observed in Figure 21. Again, the added mass is 0.045 kg before the impact and then increases after it. Regarding the relationship with the SFS values it can be noted the same trend as described in the previous paragraph. Table 6 shows the percentages of the added mass in relation to the SFS.

*Table 6 - Percetual value of added mass recorded – SOFT = 2*

| SFS value | Added Mass % |
|---|---|
| 1 | 3 % |
| 2 | 3.3 % |
| 4 | 3.5 % |

From Table 6 a difference from the SOFT = 0 case is observed in the amount of added mass recorded after impact. In fact, the added mass percentages are lower, for the same SFS values of SOFT = 0 case. The explanation for this difference lies in the fact that generally lower deformations were observed with the SOFT = 2 configuration rather than with the SOFT = 0. Indeed, in Table 5 it is observed that the internal energy values at the same SFS are slightly lower than the values calculated with SOFT = 0. Consequently, the time step values also turn out to be higher than those calculated with SOFT = 0. This causes lower values in added mass.

### 2.3.3 Influence constant Time Step and Added Mass on the results

An increase in mass on the tube affects the results extracted from the simulations especially the kinetic energy and the momentum. Indeed, these two components are calculated starting from the mass of the tube. In the discussion that follows, the results obtained with the time step calculated by LS-Dyna (variable time step) are compared with those obtained with the imposed time step (fixed time step), described in Section 2.3.2.

**Kinetic Energy– SOFT = 0**

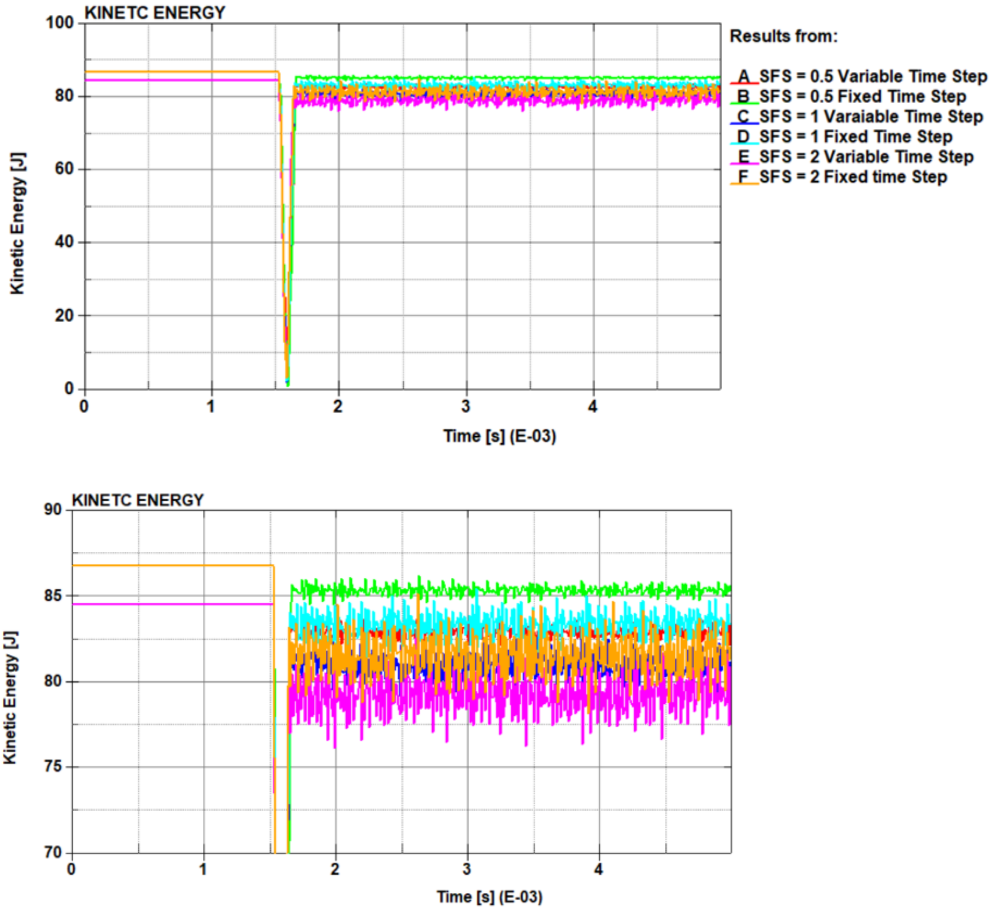

*Figure 23 - Kinetic energy comparison between fixed and variable time step - SOFT = 0*

Figure 23 shows the comparison between the kinetic energies calculated with the variable time step and the fixed time step and their relative magnification. By analyzing the trend of the curves, it can be appreciated how the added mass resulted in significant changes in the kinetic energy. Especially it can be seen that for each value of SFS the kinetic energy calculated with the fixed time step is higher than the one calculated with the variable time step; this is an effect of the artificial added mass. The increase in kinetic energy is observable both before and after the impact since, as seen in the previous paragraph, with the imposed time step value the software adds the artificial mass to the tube even before the contact.

## Internal Energy– SOFT = 0

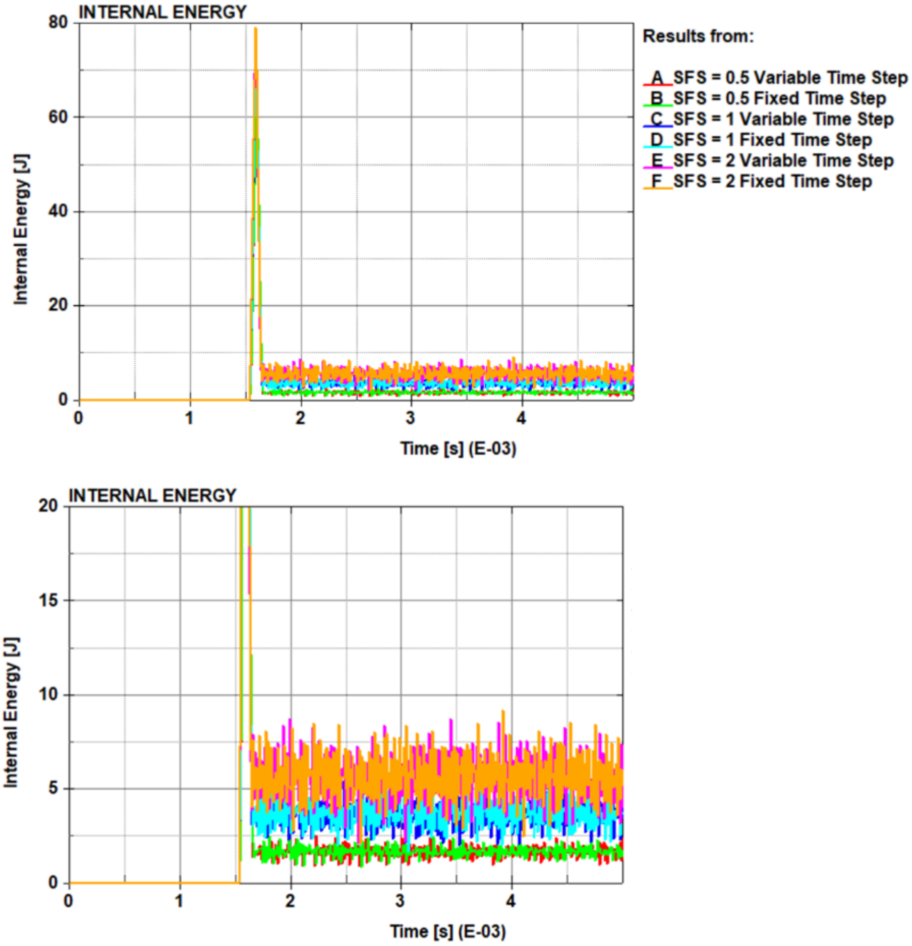

*Figure 24 - Internal energy comparison between variable and fixed time step - SOFT = 0*

The curves shown in Figure 24 correspond to the comparison of internal energy calculated with fixed time step and variable time step. Since internal energy and mass are not dependent, it is not observed an influence of the added mass on the results. In fact, unlike the kinetic energy in this case, it can be seen that the curve pairs (same SFS value) turn out to be superimposed on each other. This is an indication that the value of internal energy remains the same when calculated with time step variable than with fixed one.

### Kinetic Energy– SOFT = 2

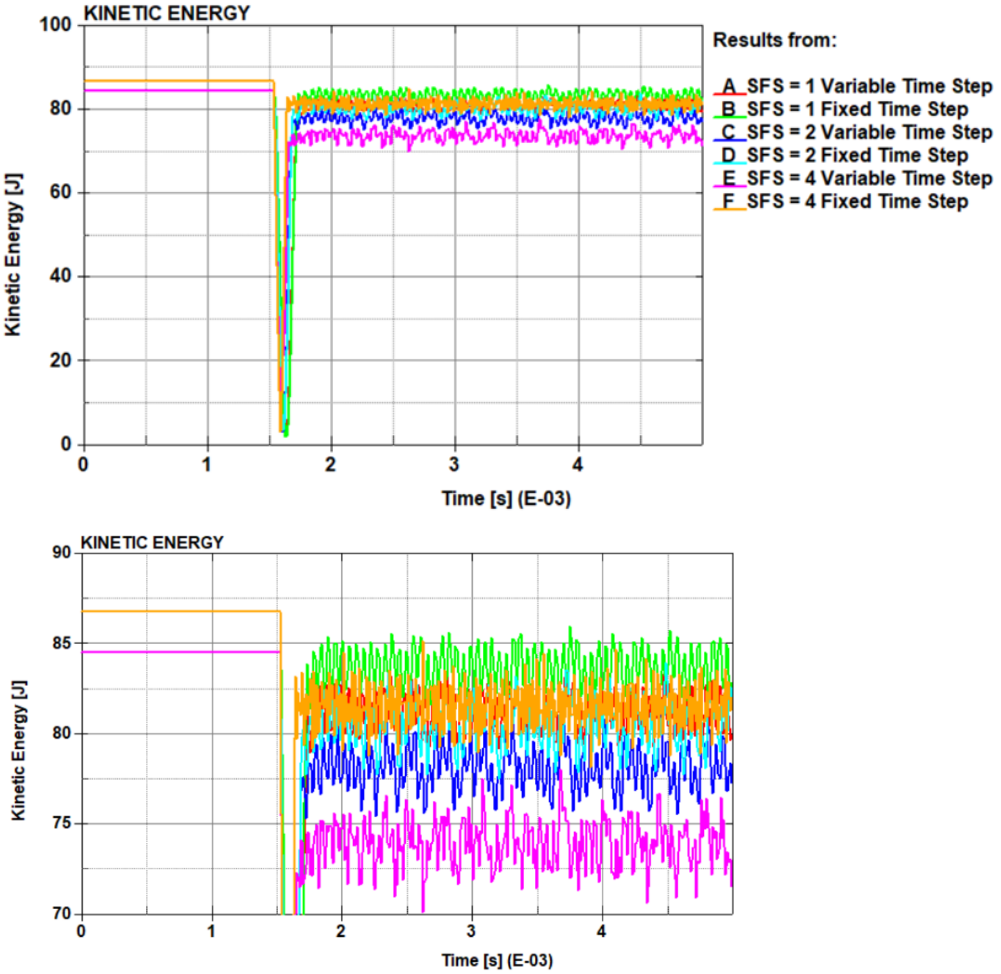

*Figure 25 - Kinetic energy comparison between variable and fixed time step - SOFT =2*

A comparison of the kinetic energies calculated in the SOFT = 2 configuration and their magnification can be seen in Figure 25. A trend similar to that described in "Kinetic Energy- SOFT = 0" can also be observed here. A difference is noted regarding the SFS = 4 case. In this case the pair of curves present a significantly larger gap than that seen for the other pairs. This is due to the fact that the value of 4 assigned to the SFS parameter resulted in a considerable increase in contact stiffness, which causes a considerable increase in added mass in the fixed time step case.

### Internal Energy– SOFT = 2

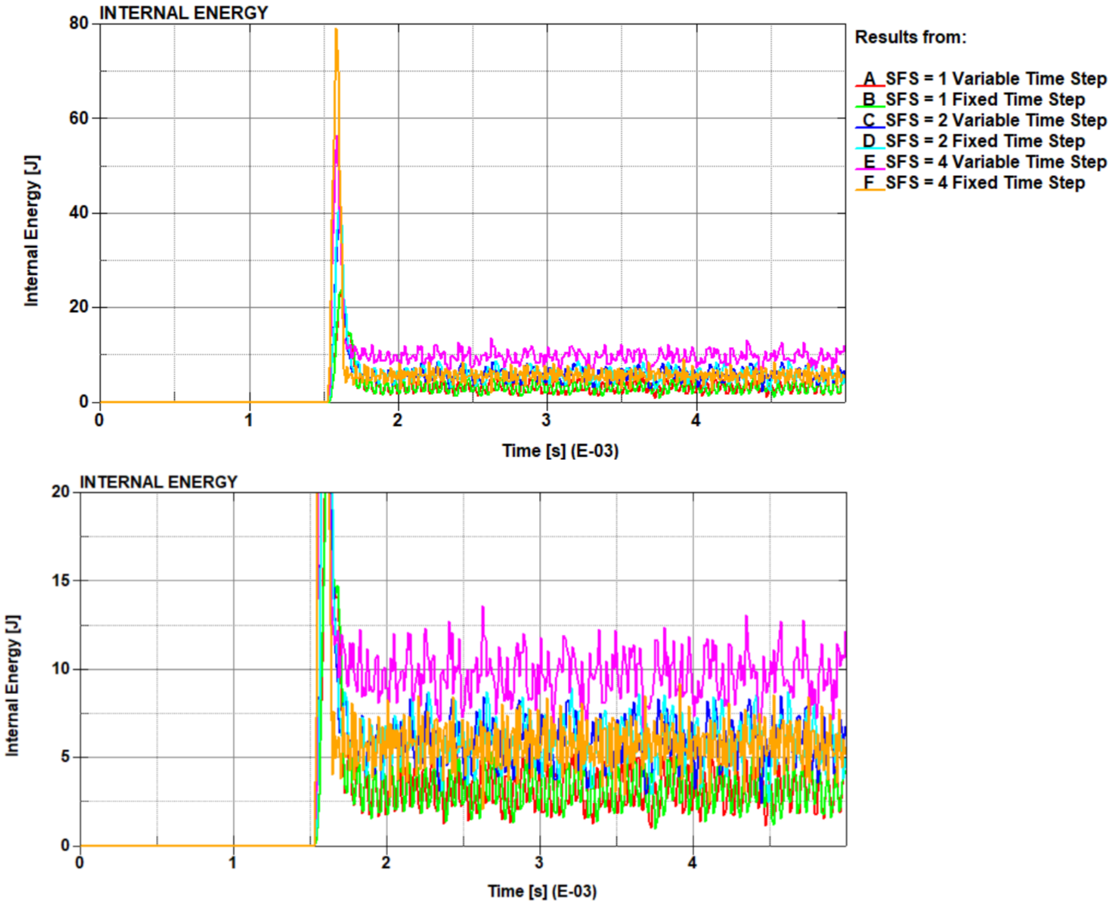

*Figure 26 - Internal energy comparison between variable and fixed time step - SOFT = 2*

The graph in Figure 26 shows the comparison of the internal energies calculated with SOFT = 2. In this case it can be seen that the two curves with value of SFS = 1 present the same trend and are overlapping. A similar situation occurs for the curves with SFS = 2. Consequently, no effect due to mass scaling is detected in these two cases. As for the curves with SFS = 4, they are not overlapping. The curve calculated with the fixed time step differs from the one calculated with the variable; in fact, the latter presents lower values. This is related to what was said in the previous paragraph about the kinetic energy: it was observed that for the SFS = 4 case, the kinetic energy calculated with the fixed time step deviated significantly from the one calculated with the variable time step. Consequently, this greater variation affects also the internal energy since there is a close correlation between these two energies. In this case it can be concluded that, for values of SFS higher than 2, the mass scaling presents an effect also on the calculation of the internal energy.

## 2.4 Contact energy analysis

The analysis performed on contact energy aims to monitor the presence of any undetected initial penetrations between the tube and the barrier during impact. In fact, undetected penetrations correspond to abrupt increases in negative contact energy. In LS-Dyna contact energy is defined as the stored energy in the compressed contact virtual springs, so as long as there are contact forces being applied, there will be nonzero contact energy. As explained in section 1.2, the contact penalty method bases its operation in the application of elastic contact forces to the penetrating nodes. The contact energy is then defined as the product of the contact force and the displacement of the nodes, i.e., the penetration depth. The contact energy is defined in the Equation 8.

$$E_{contact}^{n+1} = E_{contact}^{n} + \left[ \sum_{i=1}^{nsn} \Delta F_i^{slave} \times \Delta dist_i^{slave} + \sum_{i=1}^{nmn} \Delta F_i^{master} \times \Delta dist_i^{master} \right]^{n+\frac{1}{2}}$$

*Equation 8*

Where *nsn* is the number of slaves nodes, *nmn* is the number of master nodes, $\Delta F_i^{slave}$ is the interface contact force between the $i$th slave node and the contact segment; $\Delta F_i^{master}$ is the interface contact force between the $i$th master node and the contact segment. $\Delta dist_i^{slave}$ is the incremental distance the $i$th slave node has moved during the current time step and $\Delta dist_i^{master}$ is the incremental distance the $i$th master node has moved during the current time step [6].

When the friction is included in a contact definition, a positive contact is to be expected. Friction should result in positive contact energy. In the analyzed case the friction is absent so it is desirable to observe a small positive contact energy. Since small is a matter of judgement usually 10% of peak internal energy might be considered acceptable for contact energy in the absence of contact friction.

## 2.4.1 Influence of Standard Penalty Formulation and Contact Stiffness Scale Factors (SFS) on Contact Energy

**Net Contact Energy– SOFT = 0**

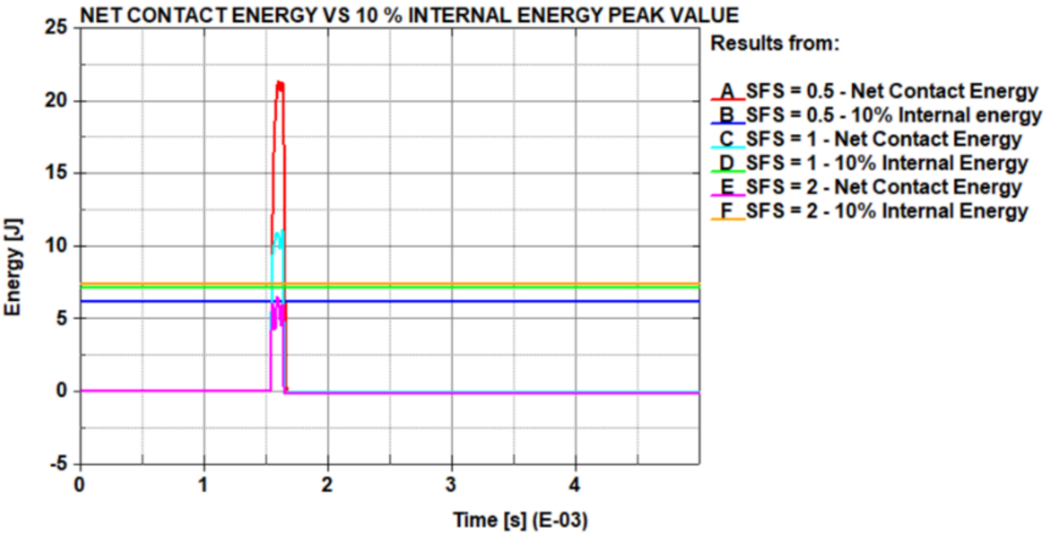

*Figure 27 - Net contact energy and 10 % internal energy comparison - SOFT = 0*

Figure 27 shows the trend of contact energy for the SOFT = 0 case. In the figure the curves corresponding to 10% of the internal energy value calculated for each case are also shown. It is observed how the trend of internal energy presents a peak at the instant of impact and then drops when the impact is over. It is noted that as the SFS value increases, the peak of contact energy tends to decrease in magnitude. This trend can be explained by the fact that, as described in section 2.2.1, by increasing the contact stiffness the penetration of the elements tends to decrease. Consequently, since contact energy is the product of contact force and node displacement it will tend to decrease as contact stiffness and SFS value increase. The table below shows the percentual peak values of the Net Contact Energy with respect.to. the Internal Energy.

*Table 7 – Percentual peak of net contact energy with respect to the internal energy - SOFT = 0*

| SFS | % peak value Net Contact Energy w.r.t. Internal Energy |
|---|---|
| 0.5 | 33.3 % |
| 1 | 15.3 % |
| 2 | 8.6 % |

It is observed from Table 7 that for the cases SFS = 0.5 and the case SFS = 1, the percentage value of the contact energy is greater than 10 % of the internal energy. For the case with the value of SFS = 2, the peak of the contact energy shows below 10 % of the internal energy.

**Net Contact Energy– SOFT = 2**

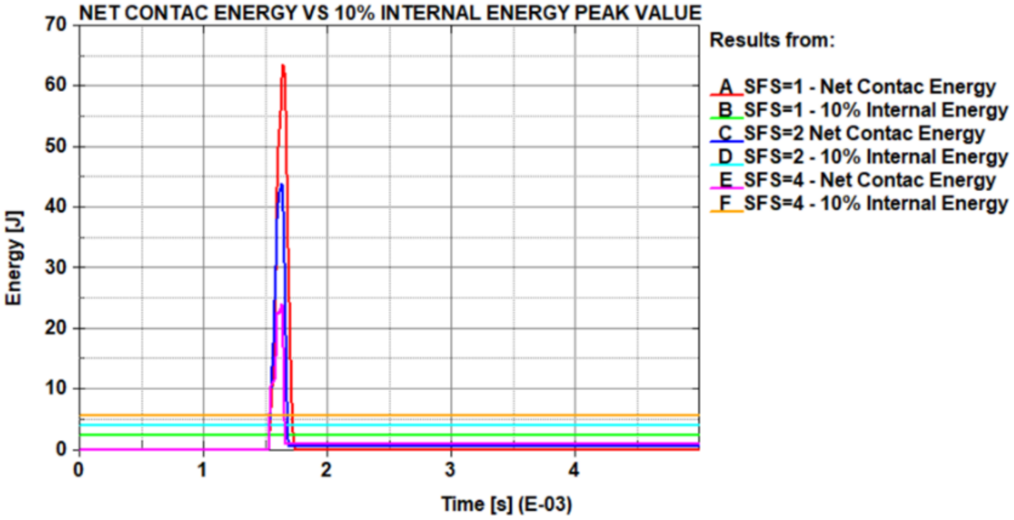

*Figure 28 - Net contact energy and 10 % internal energy comparison - SOFT = 2*

Figure 28 shows the contact energy curves for the SOFT = 2 case. The trend is the same as that described in the previous section. It is also observed in this case how the contact energy peaks tend to decrease as the value of SFS increases. The main difference noted for the SOFT = 2 case is the presence of values of the contact energy higher than the cases analyzed in the SOFT = 0 case.

*Table 8 - Percentual peak of net contact energy with respect to the internal energy - SOFT = 2*

| SFS | % peak value Net Contact Energy w.r.t. Internal Energy |
|---|---|
| 1 | 262.5 % |
| 2 | 112 % |
| 4 | 42 % |

Table 8 shows how in all 3 cases the peak contact energy exceeds 10 % of the internal energy. The peak contact energy decreases as the SFS values increases. For the case SFS = 1 and SFS = 2 contact energy values higher that 100 % are recorded.

# 3. Tube shock - crush case

The objective of this second analyzed case is to compare LS-Dyna and Europlexus (EPX) software on a more articulated case than the tube shock case. In this case shock and crush of a tube of plastic material are combined. The tube is crushed by a mass, which is applied to the top end nodes, against a rigid barrier. The barrier moves in the opposite direction of the tube, causing the combination of shocking and crushing of the tube. In fact, a velocity with a direction opposite the one of the rigid barrier is imposed on the added mass; consequently, the tube will move jointly with the added mass and impacts against the barrier. The combined action of the added mass and the movement of the rigid barrier cause the impact and the consequent crush of the tube. The set up of the simulation is described in the following paragraph and shown in Figure 29. The comparison of the results is done in terms of the internal, the kinetic, the total energy and the velocity of the added mass along the z-axis. Also in this second case, the analysis is focused on the effect of contact scale factors (SFS) on the results and their comparison with the results obtained in EPX. Regarding the contact penalty configuration in this discussion, only the Pinball Contact Penalty Formulation (SOFT = 2) is considered since it has been observed that the results obtained with this configuration of contact result extremely similar to those obtained with the Standard Contact Penalty Configuration (SOFT = 0). The same analysis with SOFT = 0 can be found in A. Spizzirri's thesis "Development of simplified vehicle models for barrier impact" in Chapter 3.

## 3.1 Model set up

The model consists of a rectangular shaped tube with three narrowing sections that act as folding triggers which are collocated on the shorter side of the tube. In addition, the rectangular plane barrier is present; the two elements are shown in Figure 29.

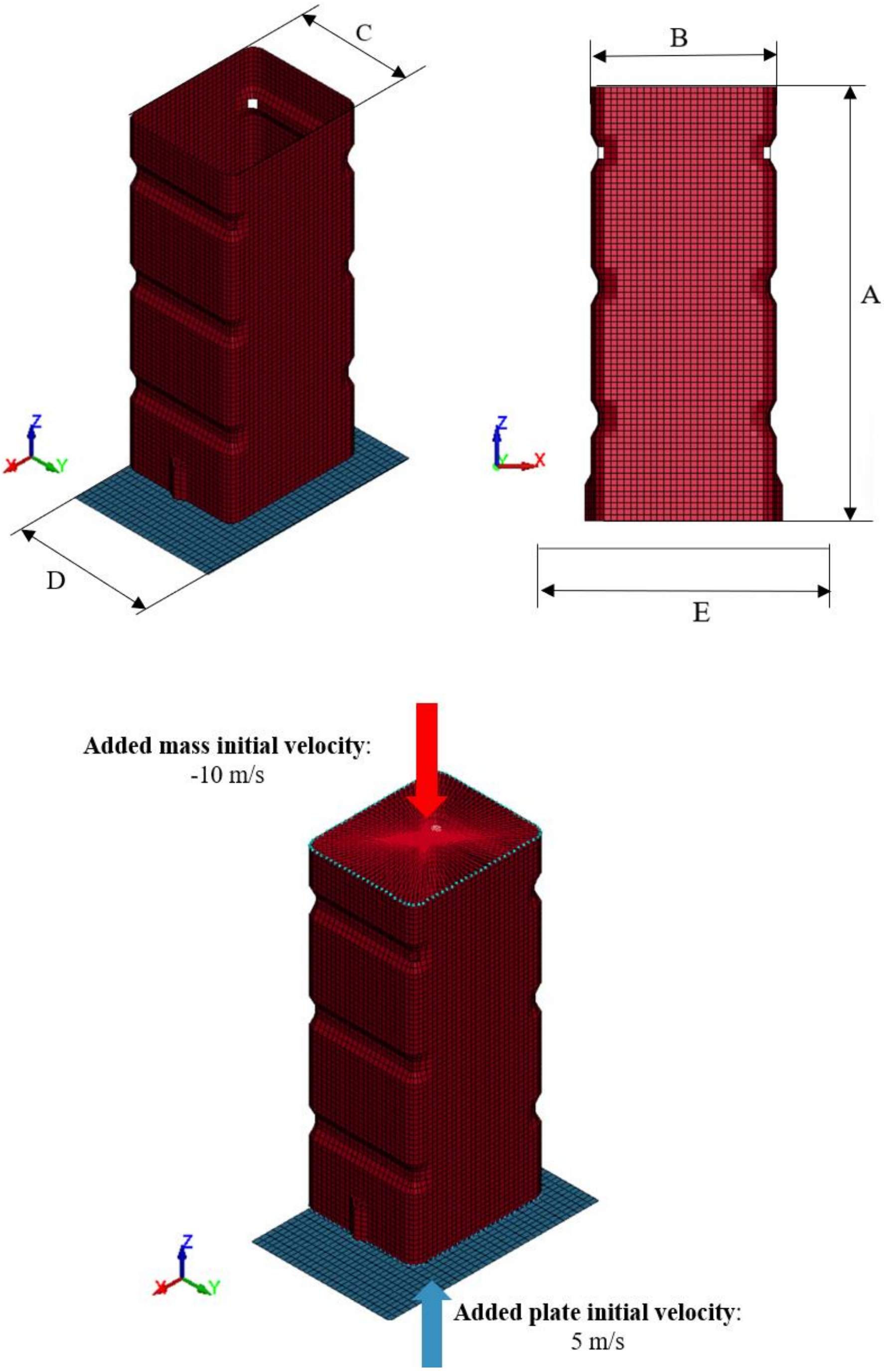

*Figure 29 - Model configuration*

The dimensions of the two components are summarized the in Table 9:

*Table 9 - Tube and barrier dimensions*

| Dimensions (mm) | TUBE | BARRIER |
|---|---|---|
| Height | 272 (A) | - |
| Length | 116 (B) | 182 (E) |
| Width | 96 (C) | 120 (D) |
| Thickness | 2 | 2 |

With reference to the mesh, the two components were modelled with shell elements and, regarding the mesh size, it was decided to use two different mesh sizes in particular:

- Tube: 4 mm
- Barrier: 4×6 mm

The reason of this choice was already explained in the Chapter 2, paragraph 2.1. The F16 (Fully integrated shell element) element formulation for the shell section is chosen for both parts (tube and barrier). This formulation is a fast element formulation used for very deformed shell elements [6].

As regards the materials, the tube is made of steel and the material law assigned is the elasto-plastic. The characteristic values of the material used for the tube in the model are listed in the Table 10.

*Table 10 – Tube material properties - steel*

| | |
|---|---|
| Density (kg/m$^3$) | 7830 |
| Young's modulus (GPa) | 200 |
| Poisson's ratio (-) | 0.3 |
| Yield stress (Mpa) | 207 |
| Effective plastic failure limit (-) | 0.75 |

The stress – plastic strain curve of the material, shown in the Figure 30, has been used in the model setup of the simulation.

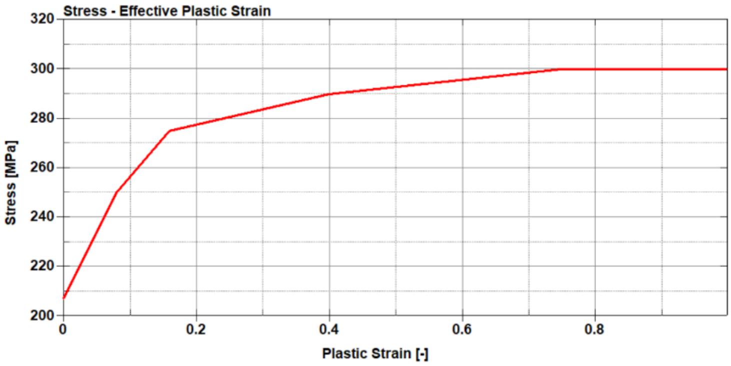

*Figure 30 – Material stress – plastic strain curve*

For what concern the barrier material, it is also steel and the material law assigned is rigid and consequently is not subject to deformations.

Regarding the added mass on the upper end of the tube that allows its crushing, an "Element Mass Node Set" was used. In this way a mass equal to 80 kg is applied to the 104 nodes on the upper end of the tube and as a consequence a mass of 0.76925 kg is applied to each node. A velocity one equal to -10 m/s in the z-axis direction was imposed on this mass. The nodes to which the added mass is applied are highlighted in light blue in Figure 31 while those highlighted in orange correspond to the nodes used for tube crush velocity tracking and analysis.

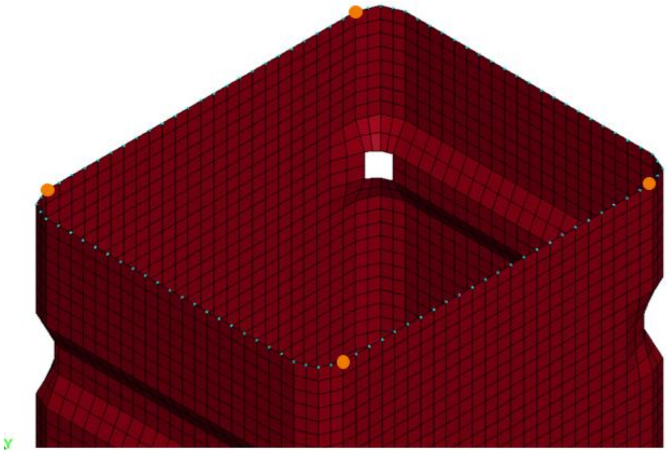

*Figure 31 - Element Mass Node Set*

The set of nodes present on both the upper and lower ends of the tube were constrained so that they could move only along the Z axis. This was made applying two constrained nodal rigid bodies on the extremities of the tube as shown in Figure 32.

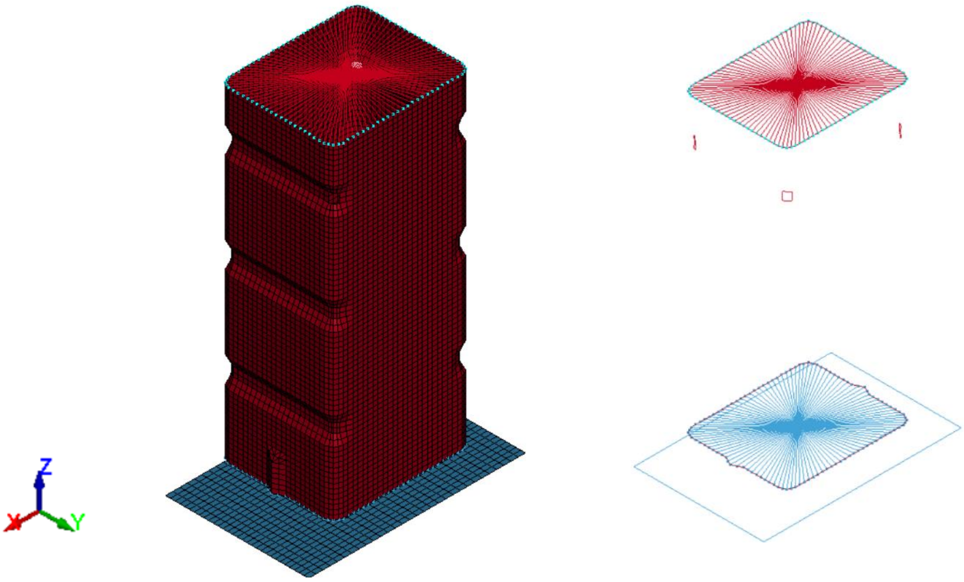

*Figure 32 - Constrained nodal rigid body*

As for the rigid flat barrier, on the other hand, a velocity of 5 m/s is imposed on it with direction toward the Z axis; the velocity in this case is applied to all nodes of the barrier.

## 3.1.1 Contacts set up

Once the model set up was completed the contact between the tube and the rigid barrier was defined. In particular, the parameters that has been set in software contact card are those related to the Contact Penalty Formulation (SOFT) and the Contact Stiffness Scale Factors (SFS). In this case only the Pinball contact penalty formulation (SOFT 2) is analysed. Different values of contact stiffness scale factors are analyzed in order to act directly on the stiffness of the contact. It was also possible to observe which configurations were more consistent with the results coming from EPX and which were less. The values assigned to the SFS parameters were chosen in a range between 1 and 4 so that different contact stiffness values can be compared with the default case (SFS =1). Between these values, were chosen only the ones that brought greater changes in the results and which allowed to obtain values more consistent with the EPX results; in particular were studied the values equal to 1, 2 and 4. The Table 11 lists the configurations investigated.

*Table 11 – SOFT and SFS configuartion*

| Case studied | SFS values | | |
|---|---|---|---|
| SOFT 2 | 1 | 2 | 4 |

## 3.2 Results comparison

As the previous case, the objective of this study is the comparison between the results coming from simulations obtained with LS-Dyna with those coming from EPX. Also in this analysis, the results obtained with the EPX software were provided with two different contact configurations: liaj 0 and liaj 1. They correspond to two different contact stiffness configurations in particular liaj 1 corresponds to the default configuration while liaj 0 corresponds to the configuration of maximum stiffness. The results were extracted from the tube and were compared in terms of:

- Internal energy
- Kinetic energy
- Z momentum
- Added mass velocity in Z direction

### 3.2.1 Influence of Pinball Penalty Formulation (SOFT 0) and Contact Stiffness Scale Factors (SFS)

In order to facilitate the explanation of the results in terms of energies, Z momentum and velocity it is necessary to show how the tube behaves during the simulation and how it deforms accordingly. In fact, how it deforms is closely related to the trends of the energies and other results. In Figure 33 four main time instants in which it can be observed how the tube deforms by folding back on itself under the combined action of the mass and the rigid barrier are shown.

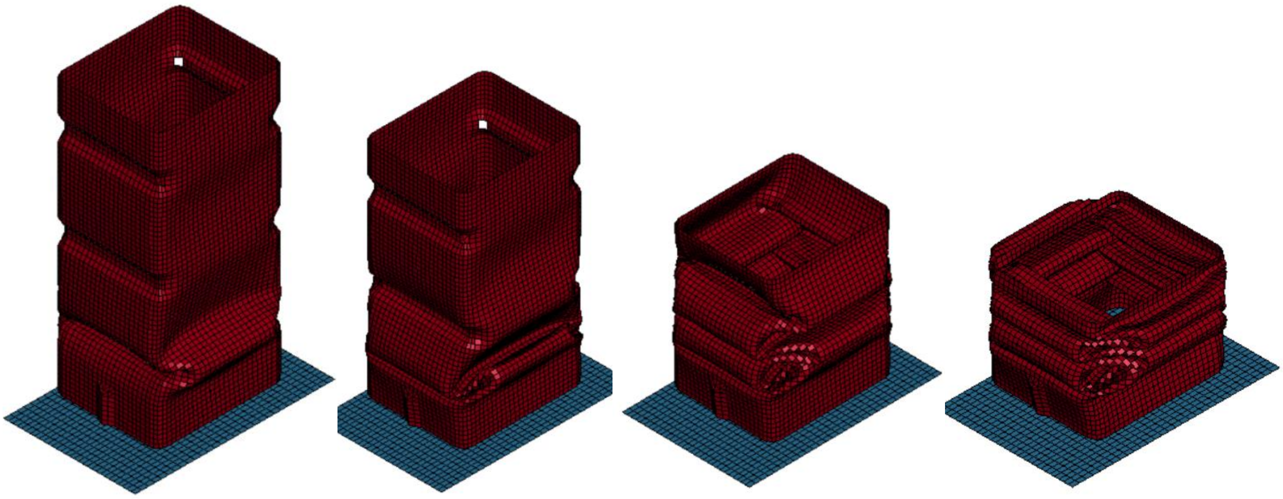

*Figure 33 - Simulation time instants: 0.002 s, 0.005 s, 0.013 s, 0.02 s*

In the Figure 33, starting from the right are shown the frames recorded at 0.002 s, 0.005 s, 0.013 s and at 0.02 s. It can be seen at the final instant (0.02 s) how the tube was crushed forming 4 folds on itself.

**Internal energy**

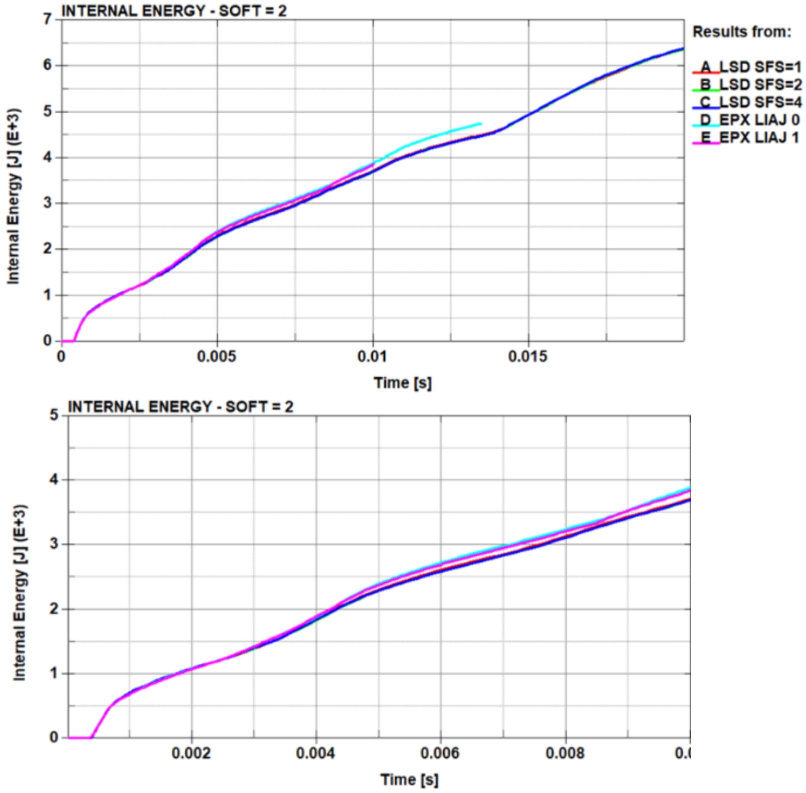

*Figure 34 - Internal energy comparison*

Figure 34 shows the internal energy trends recorded during the simulations. On the right there is a magnification of the curves. The curves obtained through EPX were not provided complete; in fact, liaj 1 stops after 0.01 s and liaj 0 at 0.016 s due to software convergence issue. Regarding the trend, it can be seen that the internal energy in the stretch between 0 and 0.001 s is zero. This part corresponds to the time between the approach of the tube and the rigid barrier, before the contact with the barrier. In this case, unlike the tube shock, the internal energy does not peak at the instant of impact but tends to increase gradually. This is due to the fact that when the tube comes into contact with the rigid barrier it does not bounce back but it is progressively crushed against the barrier by the added mass. It can be seen that the internal energy tends to increase almost linearly during the simulation. This almost linear trend is given by the fact that the tube is deformed almost constantly by the mass. This particular deformation trend is due to the geometry of the tube. In fact, as it can be seen in Figure 29 it presents equally spaced narrowing along the vertical face of the tube that facilitate the formation of the folds during the compression. Looking at the curves of the internal energy, 4 slight fluctuations are observed. In fact, the internal energy, despite its ever-increasing trend, has local increases and decreases that alternate 4 times. A first slight peak is observed at the time instant of 0.002 s, a second around 0.005 s, the third at 0.011 and the fourth 0.0175 s. These undulations are due to the folds on itself that the tube makes as it is progressively compressed. At each folding there is a greater increase in internal energy and consequently greater deformation. In the time between two folds, the internal energy tends to move to constant values because the deformation is reduced in magnitude compared to the instants that concern the creation of the folds.

As for the analysis on SFSs, great differences with respect to the tube shock are observed. Indeed, it can be seen that the curves calculated with the three different SFS values turn out to be overlapping. This overlap of the curves indicates that in this case the change in contact stiffness is irrelevant to the results. This is explained by the fact that, as already analyzed in Chapter 2, the contact stiffness affects the force applied to the nodes impacting against the barrier. In this case, the tube first impacts against the rigid barrier and then gets crushed by the added mass on its upper end; the initial deformation due to the impact between the tube and the barrier is 2 orders of magnitude less than the maximum deformation caused by the added mass in the following instants.

Consequently, variation in the tube deformation due to the different contact stiffnesses is not appreciable in the internal energy graphs.

As for the comparison of the curves obtained with LS-Dyna and EPX, the results are very consistent with each other. Between 0 and 0.01 s an almost perfect overlap of the curves is observed for both liaj 1 and liaj 0. After 0.01 s liaj 1 stops while liaj 0 tends to remain slightly above the curves obtained with LS-Dyna thus indicating higher deformation calculated by EPX.

### Kinetic energy

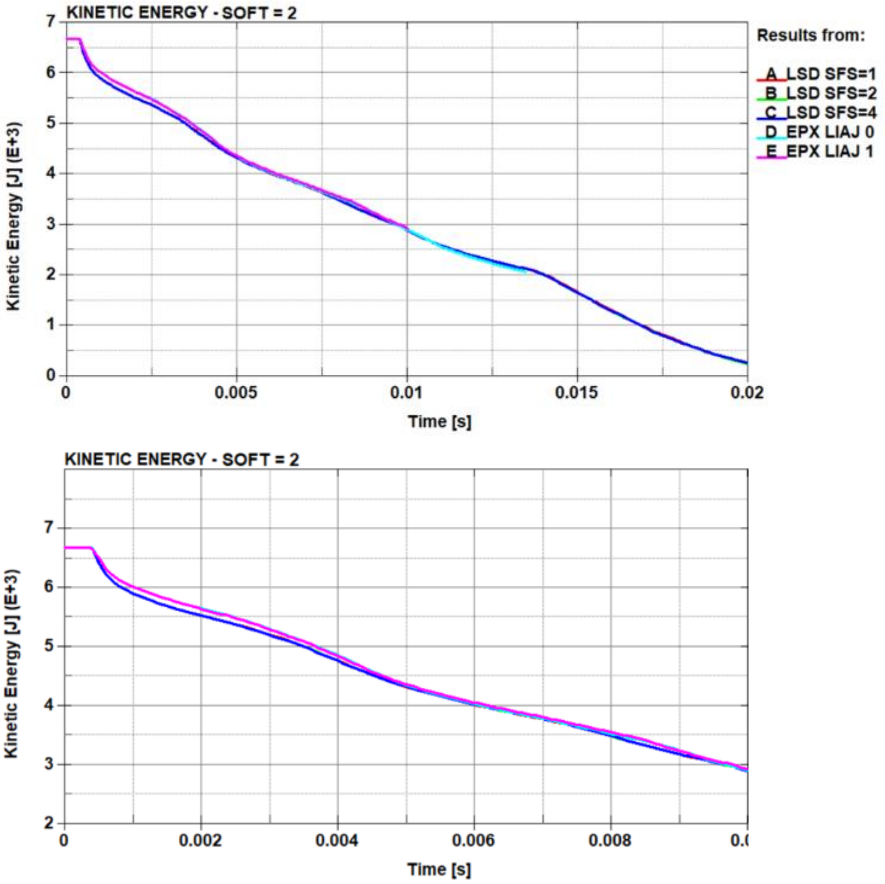

*Figure 35 - Kinetic energy comparison*

Figure 35 shows the trend of kinetic energy and its relative magnification. The graph are specular to the internal energy one due to the energy balance principle. The explanation for this trend was previously discussed in section 2.2.1. The trend of the curve has an initial constant section where the tube moves through space and impacts against the rigid barrier (0 - 0.001 s). After the impact, the kinetic energy begins to decrease with an almost linear trend and reaches the value close to 0 J at the end of the simulation. Four fluctuations are also observed in this case. They are caused by the formation of the tube folds back on itself. In fact, the speed of deformation of the tube slows down at the time it deforms by creating a fold while it increases between the formation of one fold and another. The trend turns out to mirror that of the internal energy.

Regarding the relationship with different values of SFS, similar considerations can be made as for the internal energy. It can be seen that the curves calculated with LS-Dyna are overlapping and the different values of contact stiffness do not affect the calculation of kinetic energy. The curves calculated with EPX s are extremally similar and over imposed with those calculated with LS-Dyna. Furthermore, with respect to internal energy, the liaj 0 configuration does not tend to diverge from the other curves after 0.01 s but remains consistent with the trend of the others.

### Z Momentum

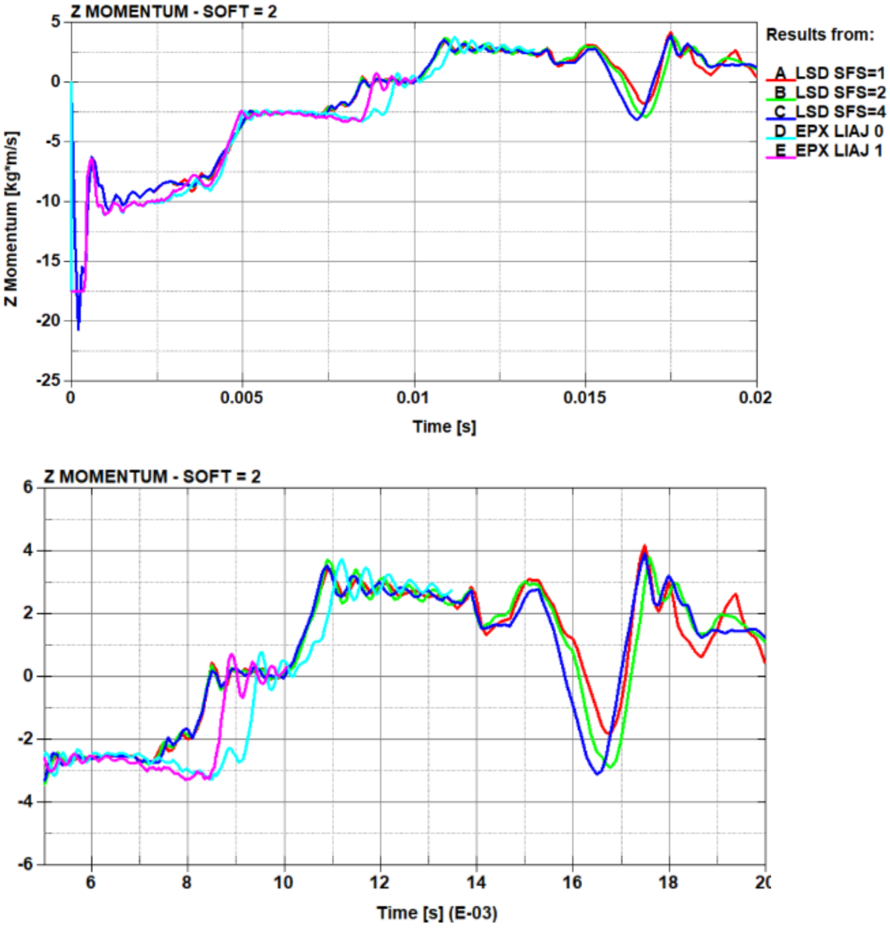

*Figure 36 - Z momentum comparison*

Figure 36 plots the trend of Z momentum. It shows a less linear trend than that observed for both kinetic energy and internal energy. Four stretches are distinguishable in which the Z momentum is at near-constant values. These segments correspond to the instants when the tube folds on itself and the tube deformation slows down. Between these instants the Z momentum increases linearly. This is due to the fact that they correspond to the instants between the formation of one fold and the next. In this portion the speed of the tube increases. After the 0.015 s all the tube folds have been formed and the deformed tube is further crushed against the rigid barrier. This causes a peak where the Z momentum decreases since the formation of the folds is complete and the tube slows down. After this instant the speed of the tube reaches 0 m/s and consequently also the Z momentum is null.

With regard to the variation of the SFS parameters, it is observed that they turn out to be irrelevant up to 0.015 s. Till this instant of time, in fact, the curves are perfectly overlapped. After the 0.015 s instant, it can be observed how the curves related to the different SFSs tend to be slightly detached from each other. In fact, in the section between 0.015 s and 0.2 s the folds of the tube are completed and it is further crushed against the rigid barrier; the latter acquires more importance in the crushing action during the last instants of the simulation. As for the comparison with EPX results they turn out to be consistent with those calculated in LS-Dyna. They are in fact superimposed for most of the time instants. A difference can be seen at instant 0.0075 s where the EPX curves tend to grow a few instants after the curves calculated in LS-Dyna. This is caused by a different formation of the tube folds in the simulations obtained in EPX.

### Added mass Z velocity

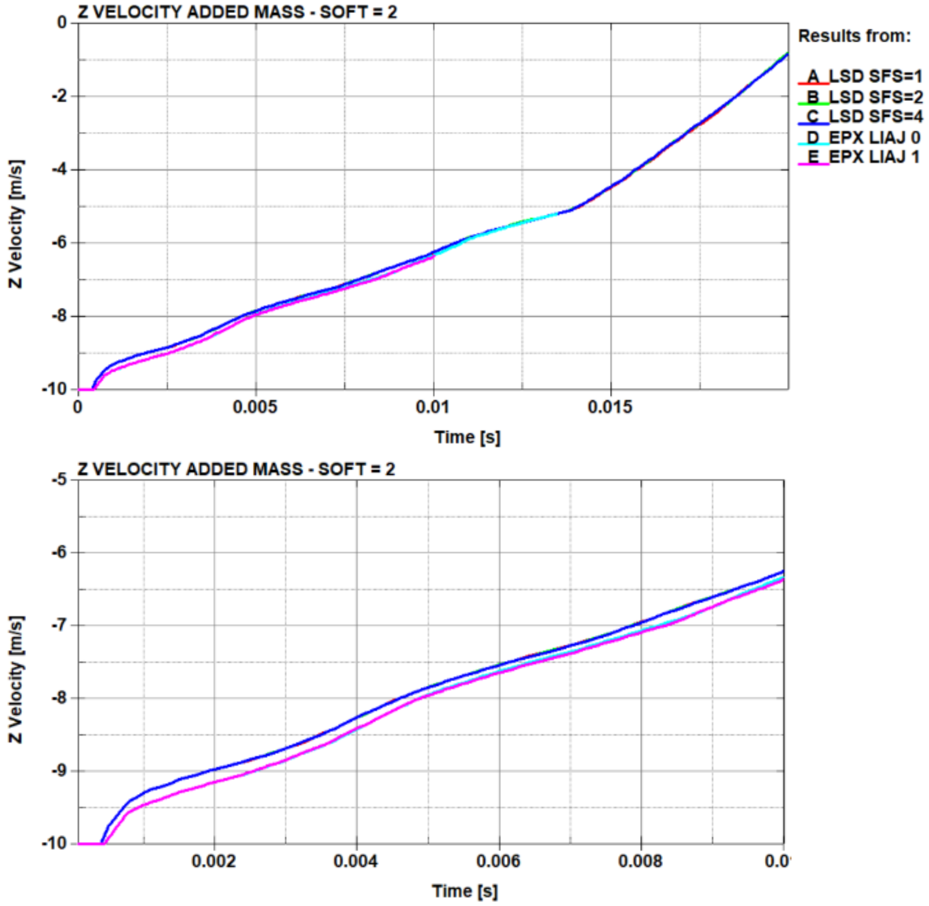

*Figure 37 - Added mass Z velocity comparison*

Figure 37 shows the velocity of the mass added to the nodes of the upper edge of the tube (Figure 31) that correspond to the speed at which the upper end of the tube moves in the direction of the rigid barrier. The curve starts from the value of the velocity imposed on the mass (-10 m/s) and then reaches a value close to 0 at the end of the simulation. In this case there is a progressive decrease in the velocity and the presence of the same fluctuations also observed in the other results as well. After instant 0.015, as noted for the Z momentum, the formation of the tube folds is completed and tube velocity slows down to the value of 0 m/s.

It is observed that the different values of SFS turn out to be irrelevant during the simulation. The curves calculated in EPX are similar and analogous to those calculated in LS-Dyna. The only difference is that the EPX curves show a slightly higher velocity in modulus between 0 and 0.01 s.

## 3.2.2 Plastic Strain comparison

As a result of what has been analyzed so far, it could be inferred how the different values assigned to the SFS parameters are negligible for the purpose of comparison between LS-Dyna and EPX. Consequently, only the case calculated with SOFT = 2 and the SFS parameter = 1 (the default value) will be considered in the analysis that follows.

**Time instant: 2 ms**

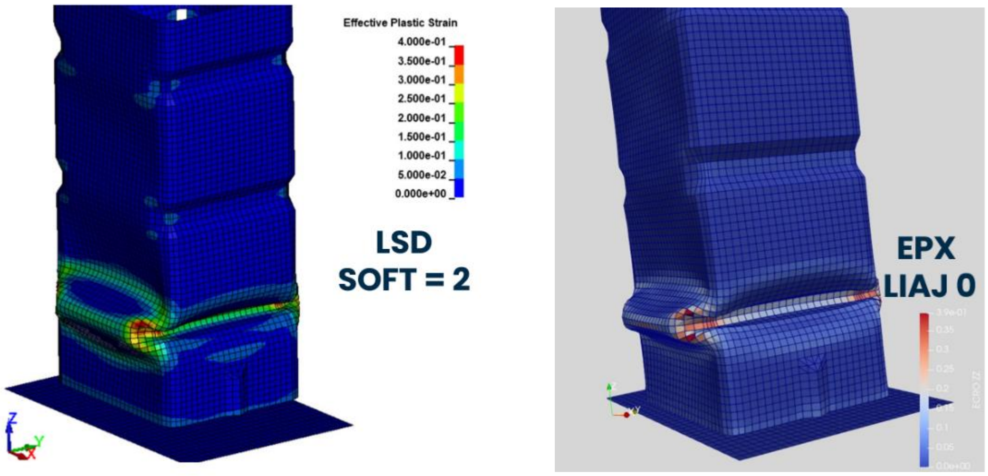

*Figure 38 - Plastic strain at 2 ms*

From Figure 38 it can be noted the comparison between the plastic strain calculated with LS-Dyna, on the left, and the one calculated with EPX on the right. As far as the strain is concerned, it can be seen that the two tubes deform in an extremely similarly way, and there are no major differences in the shape of the fold that is created. As for the distribution of plastic strain it also appears to be consistent between the two software. The only difference concerns the elements that are interested in the maximum plastic strain value; which appears, in the LS-Dyna case, on the elements of the upper edge of the fold while, in the EPX case, on both the lower and the upper edges.

**Time instant: 5 ms**

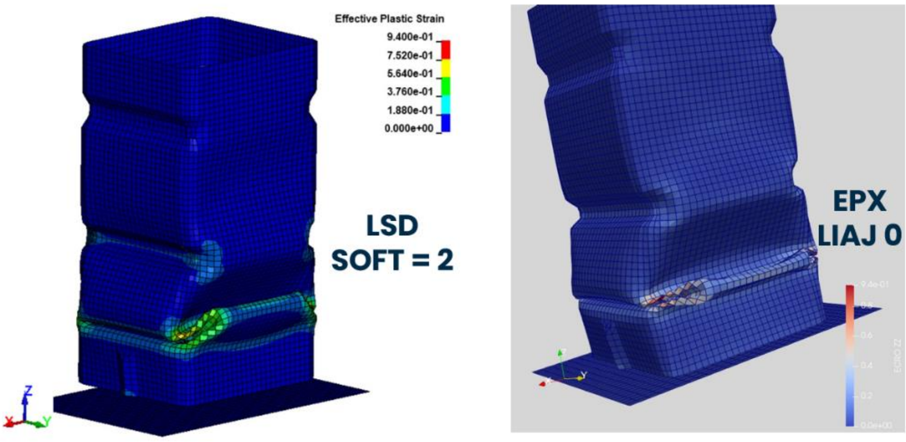

*Figure 39 - Plastic strain at 5 ms*

Figure 39 shows the comparison at 5 ms. It can be seen here how the first fold is completed and the deformation phase leading to the creation of the second one is beginning. At this instant, a more pronounced difference is observed in terms of the deformation shape obtained in LS-Dyna and that in EPX. The discrepancy concerns the fact that the fold created in LS-Dyna turns out to be more inclined upward than that observed in EPX, which remains more parallel to the XY plane. Regarding the distribution of plastic strain, it is similar for both software. The greatest plastic strain is recorded in the elements present in the inner part of the fold for both cases.

**Time instant: 10 ms**

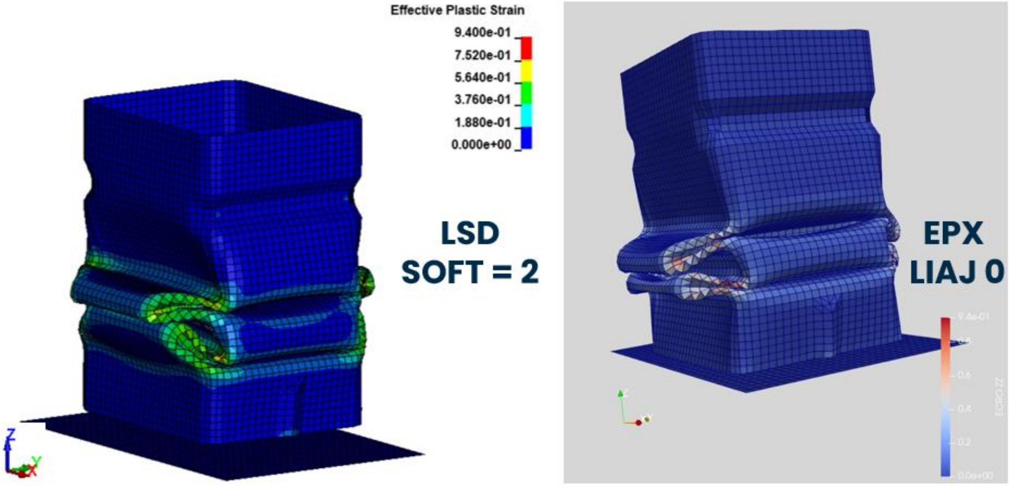

*Figure 40 - Plastic strain at 10 ms*

In Figure 40 is recorded the strain at 10 ms. At this instant the formation of the second fold is completed. Differences in terms of shape are also observed regarding this second fold. In fact, it remains more parallel to the XY plane with regard to the LS-Dyna case, while in EPX it is more inclined downward. Moreover, in LS-Dyna the deformation that will cause the formation of the third fold appears to be more pronounced than the one seen in EPX. In terms of plastic strain, it appears to be similar and analogous for both cases.

**Time instant: 13 ms**

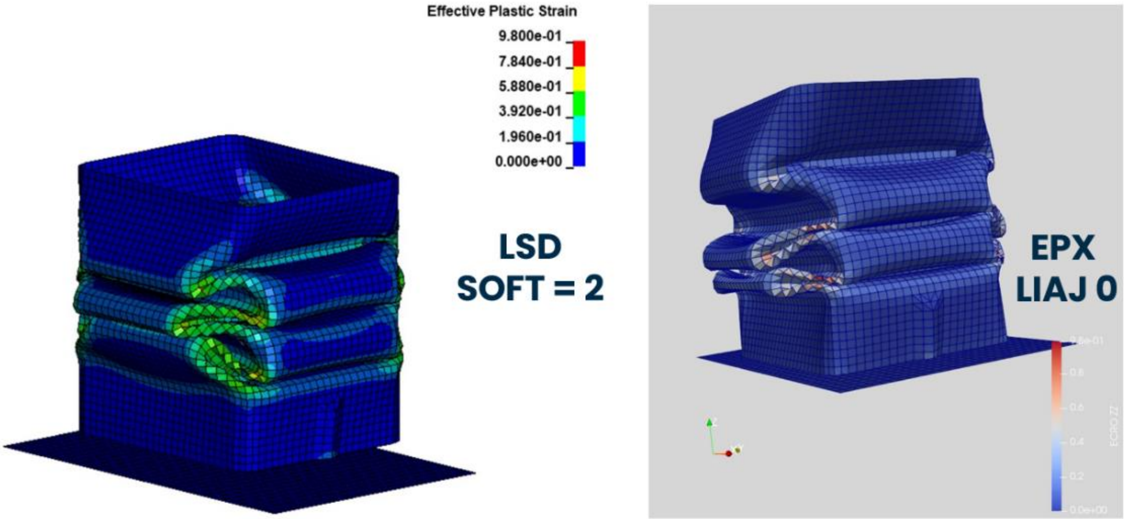

*Figure 41 - Plastic strain at 13 ms*

Figure 41 shows the deformation at instant 13 ms. At this instant it can be noted that all 3 folds have been created. The main differences that can be observed are at the formation of the third fold, which is finished in LS-Dyna, and it is not yet completed in EPX. This is observable by the fact that the edge of the fold in LS-Dyna appears much closer to the underlying fold than those in EPX. As for the plastic strain it looks similar for both cases. A difference is observed in the elements of the central fold that present the maximum value of plastic strain. Indeed, it can be seen that in the case calculated in EPX there is a higher number of elements presenting the maximum value (elements colored in dark red). A similar distribution cannot be observed in LS-Dyna on the same elements, which show values just below the maximum value; they are in fact colored in yellow. This consideration is also confirmed in the internal energy curves where it is noted that for instants between 10 and 13 ms the curves calculated in EPX present slightly higher values than those calculated in LS-Dyna.

# 4. N3C vehicle impact to safety bollard

The objective of this second part of the thesis is to simulate, through the LS-Dyna software, an impact of a vehicle belonging to category N2 or N3 against a safety bollard. The vehicle FEM model was developed by SVS FEM Services [9] and provided by the JRC. This model consists of a generic vehicle belonging to category N2/N3 on which it is possible to act through appropriate parameters to adapt the vehicle in terms of size and mass to the specific categories. The model is validated by basic tests (vehicle in idle, linear track curb test and rigid wall test) according to CEN/TR 16303; validation has been also carried out on this model by reproducing a real experiment of impact between a vehicle of category N2A against a bollard at 48 km/h [10]. It was decided to carry out a second validation by reproducing a real experiment but, in this case, increasing vehicle size and impact velocity. Through the analysis of the validation results, further suggestions for improving the vehicle modeling can be provided.

Following this second validation, the influence of the impact position between the vehicle model and a rigid bollard is analyzed. The analysis will consist of simulating an impact between the vehicle and the bollard where the latter will be positioned at different offsets from the plane of symmetry of the vehicle. From these simulations, the work consists in the comparison between the different vehicle’s deformations based on the positions of the bollard. Further attention will be paid to the internal, the kinetic, the total energy recorded and the contact force between the vehicle and the bollard. The deformations of some vehicle components that play a significant role in terms of internal energy absorption will be also analyzed in details.

The vehicle model used consists of a generic vehicle model that can be modified in terms of dimension and mass, acting on appropriate parameters. The generic vehicle model represents both required categories (N2 or N3) commercially used within the EU and does not reflect any specific brand or model-depending features [10]. The generic model and a relative detail on the structural components is shown the Figure 42.

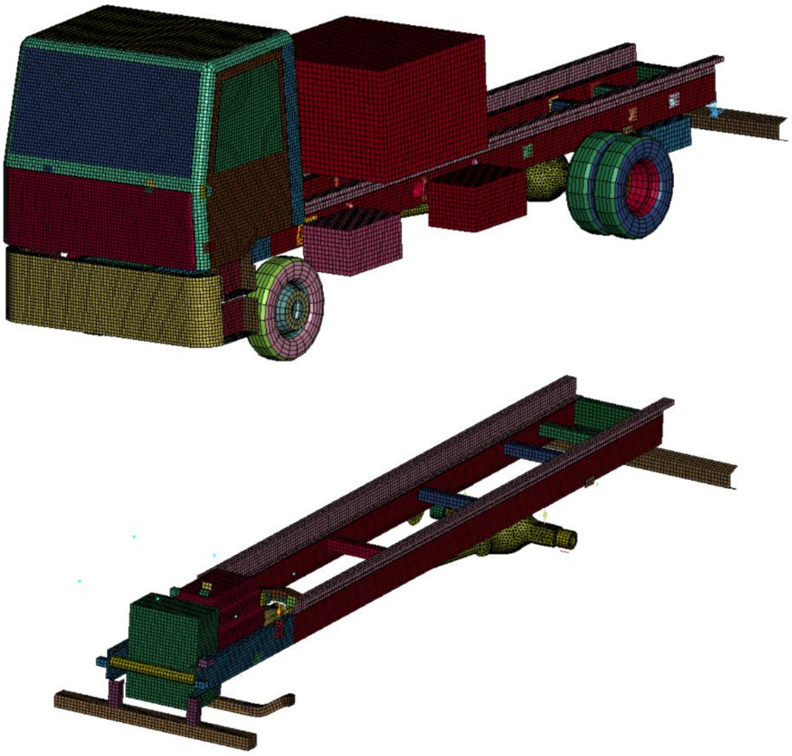

*Figure 42 - Generic vehicle model*

As shown in Figure 42 the vehicle model has only the necessary structural and exterior components. It presents a front cab enclosed in the main components of the exteriors such as the doors, the front bumper, the roof, a windscreen, etc.; inside there are the main components such as the engine, the frame, the front axle and the suspension. As for the flatbed it is composed of the longitudinal and cross beams that create the frame. There are boxes rigidly attached to the frame, that are generic representations of items which are commonly attached to the frame. Above the flatbed is placed a cargo mass that can be modified in terms of positions and weight. In fact, the model is parameterized to easily modify key attributes of the vehicle (velocity, mass distribution, dimensions, crash related stiffness, suspension properties). In the Figure 43 there are some examples of different vehicles that can be obtained by acting on vehicle dimensions, and cargo mass.

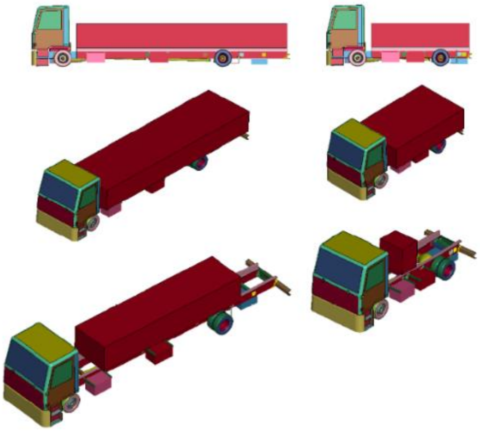

*Figure 43 - Examples of different vehicles configurations*

The model is organized in several "Includes" which are recalled by a main file (Main.k). To modify the parameters of the vehicle it is necessary to act on the parameter.k file. Figure 44 shows the schematic of how the various files and "Includes" that constitutes the model is organized.

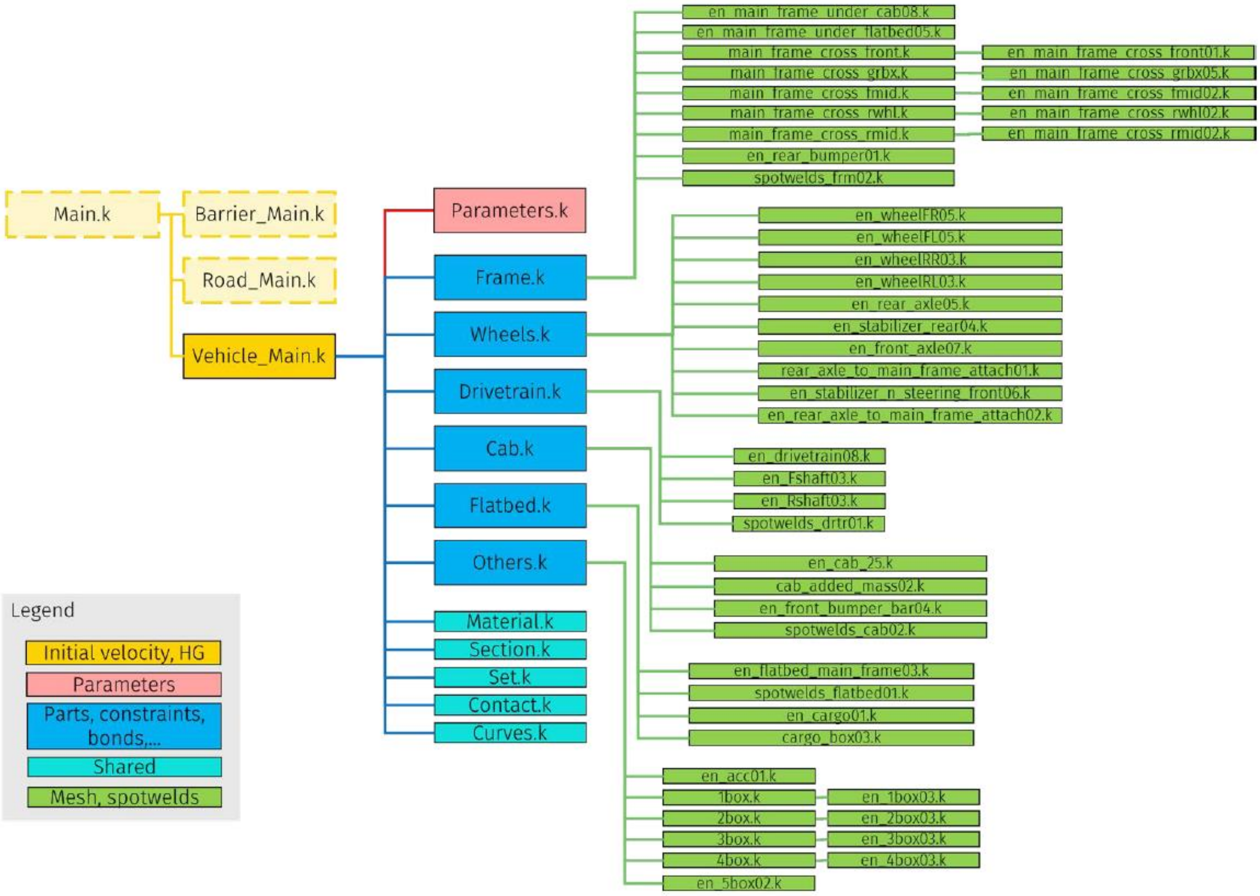

*Figure 44 - Model include organization*

## 4.1 N3C bollard impact validation

In this validation, the real experiment referring to this standard: "Moveable Bollard PAS-68 V/7500[N3C]/80/90:7.7." [11] was reproduced virtually through a simulation on LS-Dyna. In this standard, a vehicle belonging to the N3C category with a total mass of 7500 kg impacts on a bollard at a speed of 80 km/h. The impact angle between the vehicle and the bollard is 90° and the impact penetration is 7.7 m. Only the video of the experiment is available. Images of the experimental test are processed on the Tracker software by OSP [12] to extrapolate the kinematic properties of the vehicle through the tracking of three marker points on the vehicle: two are placed on the cabin (M1 and M2) and one on the flatbed (M6). Once the displacements and velocities of these markers, along X axis and Z axis, are extrapolated, they will be compared with the results obtained from the simulations carried out in LS-Dyna.

### 4.1.1 Validation set up

It was necessary to adapt to adapt the generic vehicle model, in terms of dimensions and mass, to the existing commercial vehicle used in the experimental test taken as reference for the validation. The considered vehicle category is the N3C with a mass of 7500 kg and the commercial vehicle used in the experimental test is the Renault Midlum 7.5 tons. From this vehicle the main characteristics in terms of dimensions and mass were extracted. Once obtained, acting on the parametrers.k file, they were implemented on the FEM generic model. An image of the Renault Midlum vehicle can be seen in Figure 45 showing the dimensions that were implemented in the FEM model.

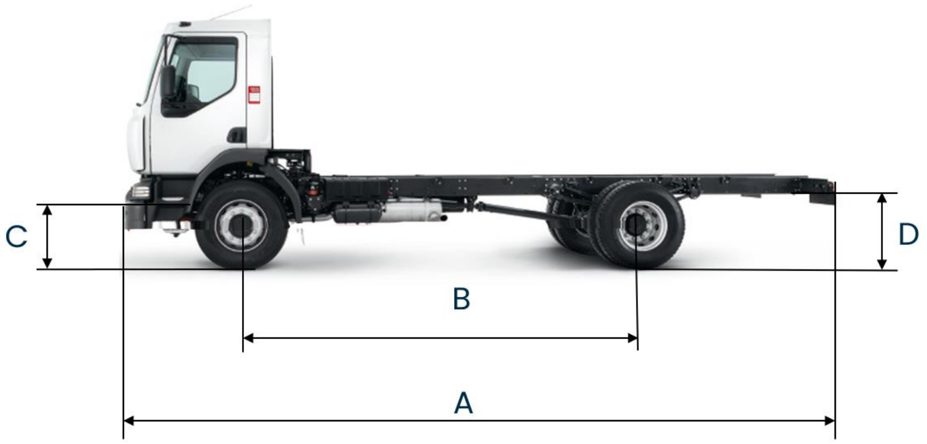

Figure 45 - Renault Midlum side view

In the following Table (Table 12) the dimensions referred to the letters shown in the Figure 39 are listed.

*Table 12 – N3C vehicle dimesions*

| Parameter | Value |
|---|---|
| Vehicle length – A (m) | 8.4 |
| Wheel base – B (m) | 5 |
| Ground clearance – C (m) | 0.84 |
| Wheel outer dimeter – D (m) | 0.922 |
| Total vehicle mass (kg) | 7500 |

The parameters shown in Table 13 were later set into the parameters.k file thus acting directly on the dimensions of the FEM vehicle model. The weight calibration was done by acting on the mass and dimensions of the cargo. A specific value of mass was set to obtain a total mass of the vehicle of 7.5 t; the geometry of the cargo was also modified so that this mass was equally distributed on the flatbed avoiding load imbalances. Figure 46 shows the modified FEM model according to the parameters of the Renault Midlum vehicle belonging to the N3C category.

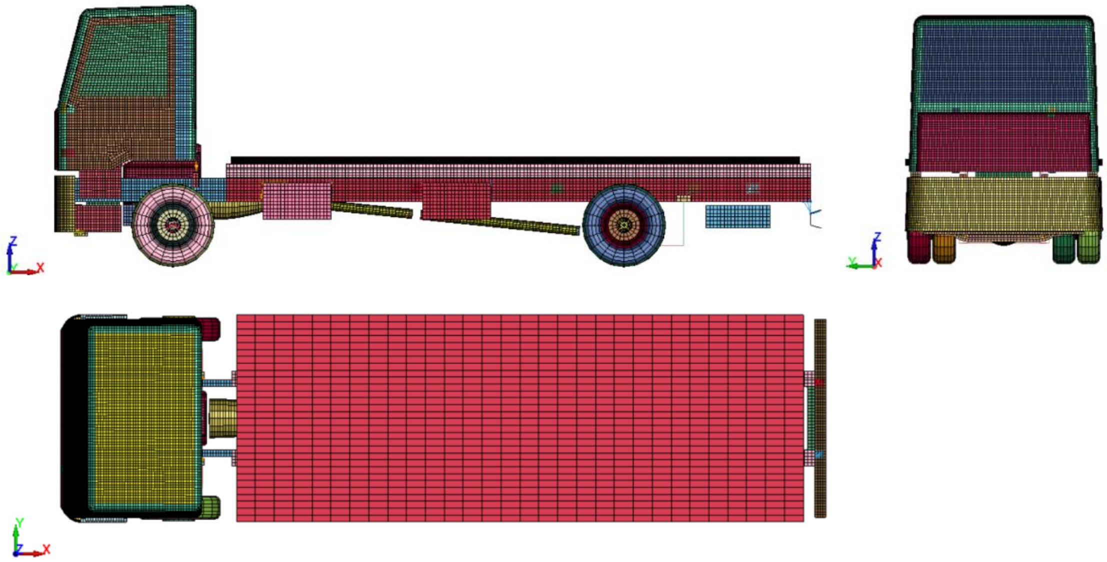

*Figure 46 - N3C FEM vehicle model*

For what concern the vehicle barrier, the bollard model used in the experiment corresponds to the FAAC J355 M50 [13]. A FEM bollard was modeled in LS-PrePost [14] with the same dimensions (height and diameter) of the experimental one. The FEM model of the bollard was modeled with shell elements and the material is steel and the material law is rigid. In the Figure 47 a picture of the experimental Bollard and the corresponding FEM model are shown.

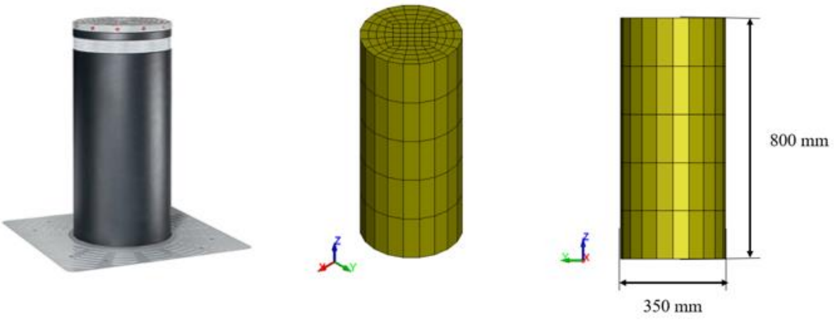

*Figure 47 - Experimental bollard and FEM bollard model*

Once the model of the bollard is completed it is placed in correspondence to the symmetry plane of the vehicle reproducing the conditions of the experiment. The set up of the bollard and vehicle can be seen in Figure 48.

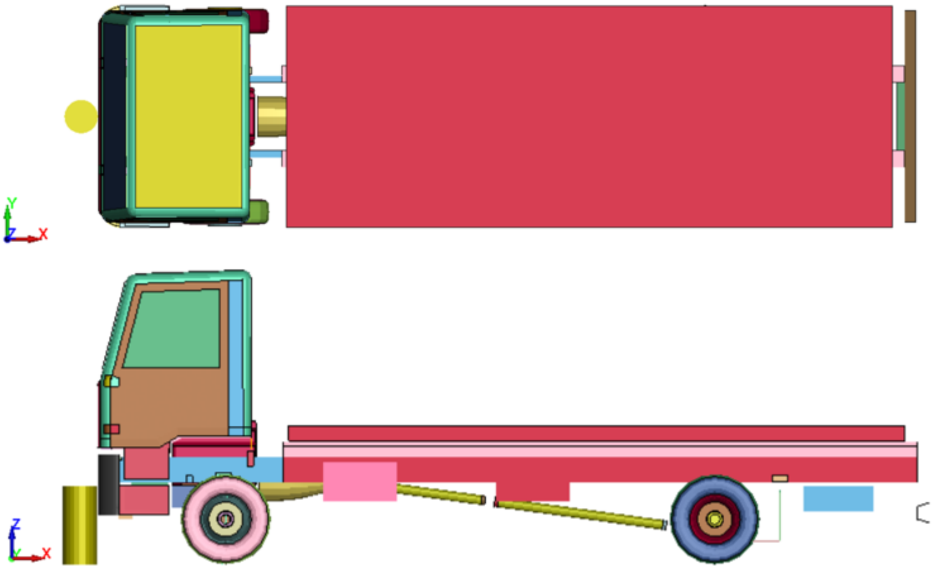

*Figure 48 - N3C validation set up*

Regarding the contact between the bollard and the vehicle, the Contact Penalty Formulation chosen is the Pinball one (SOFT = 2). The values of the contact stiffness scale factor were left at the default value (SFS = 1), while the values of the static and dynamic friction coefficients (FS and FD) are both set to the value of 0.3. The vehicles speed is imposed with the same value of the experimental one: 80 km/h; and the simulation is run with a duration of 1000 ms.

## 4.1.2 Results comparison - animations

### Lateral view comparison

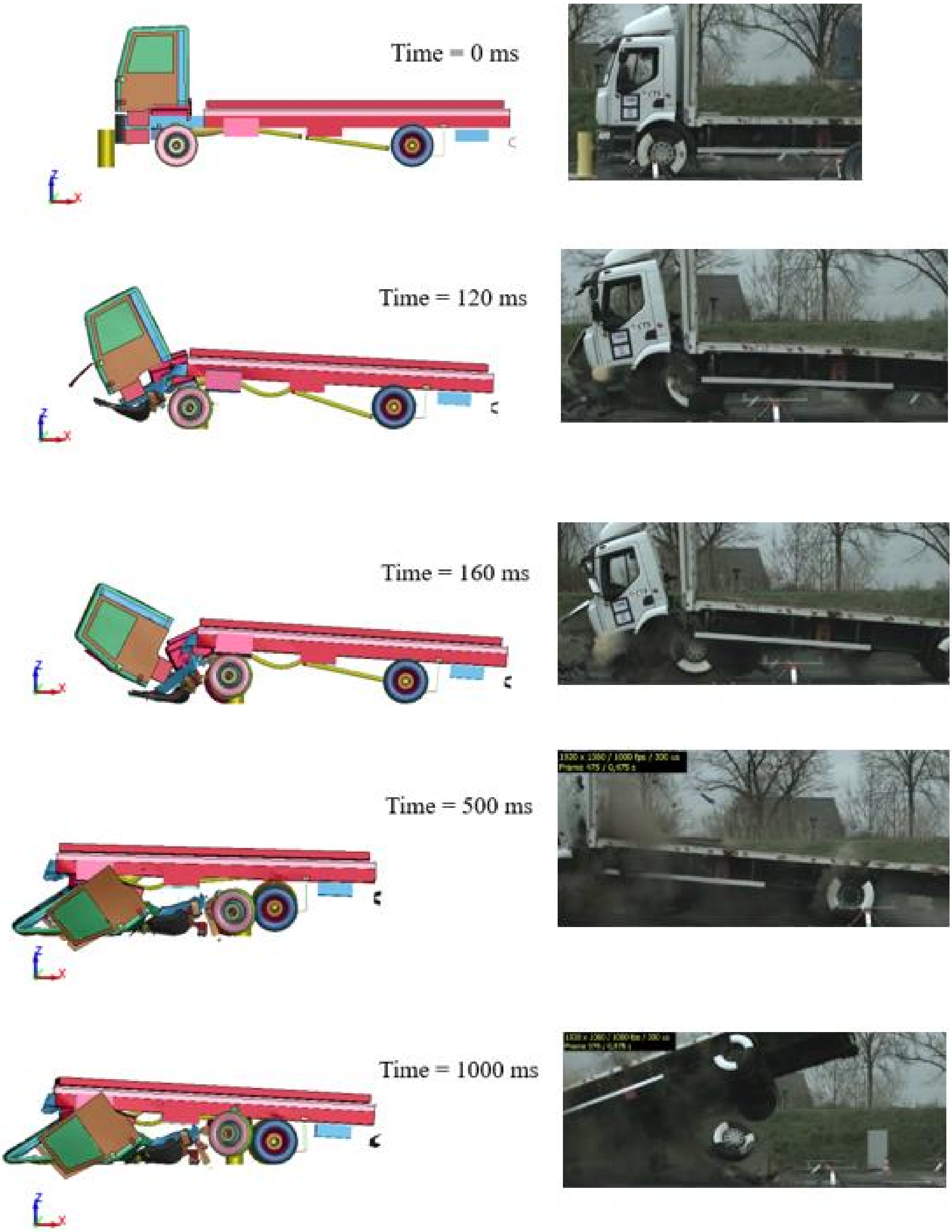

*Figure 49 - Lateral view comparison between simulation and experiment*

### 45° view comparison

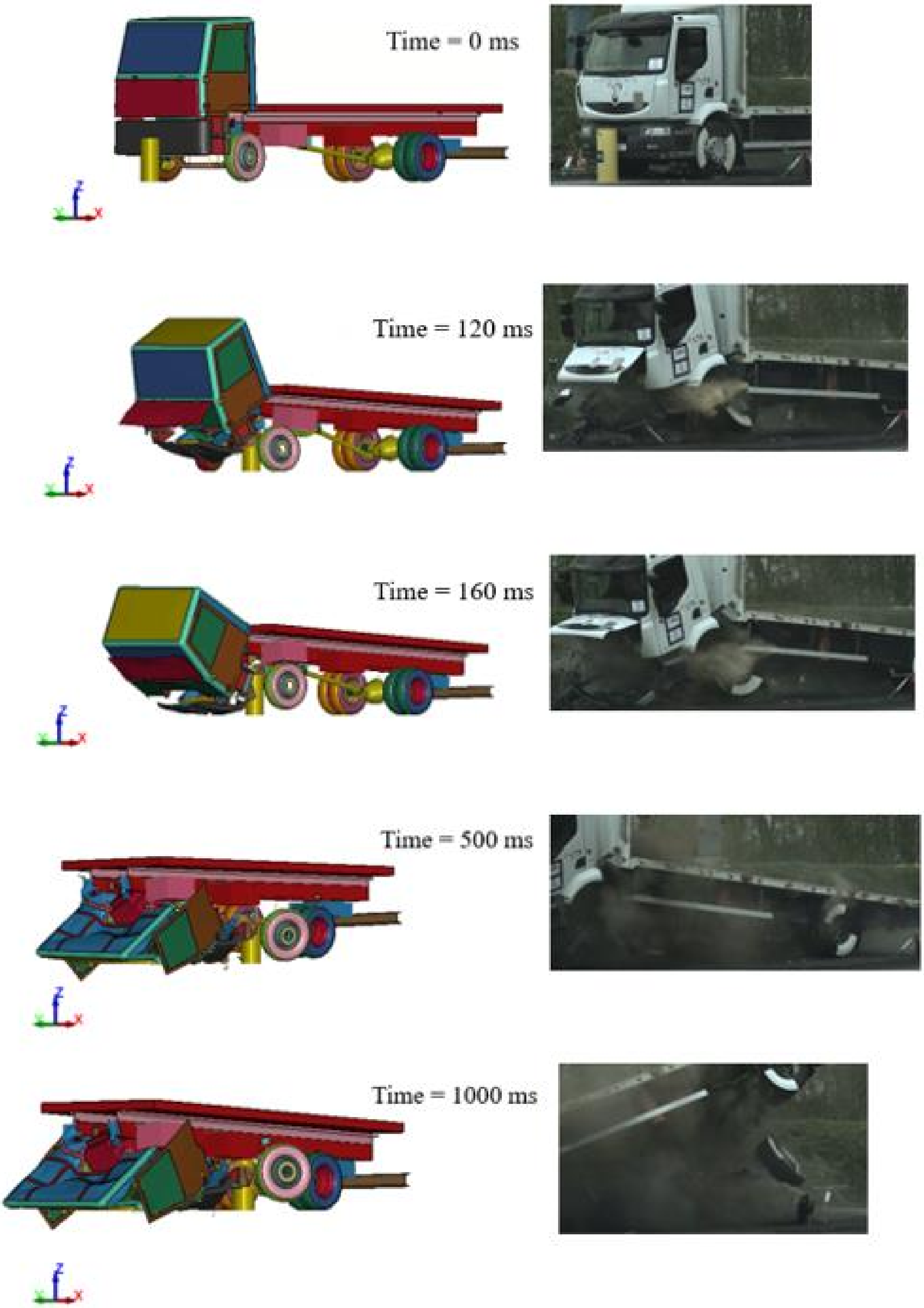

*Figure 50 - 45° view comparison between simulation and experiment*

From Figures 49 and 50, a comparison between time instants of the simulation obtained in LS-Dyna and the real experiment can be observed. Overall, the results of the simulation appear to be consistent with the real experiment. In fact, the vehicle impacts against the bollard and then overcomes it and stops when the rear axle collides. This behavior is, indeed, observed in both the simulation and the experiment. It is also noted how, for both the real case and the virtual one, the front axle is torn from its connections with the frame and gets stuck against the bollard.

The main difference is observed in the behavior and deformation of the cabin. From the instant t = 160 ms onward, it is noted that the cab of the FEM model tilts forward by rotating around the Y-axis much more than its real counterpart. At t = 500 ms it is observed how the FEM model's cabin is completely crushed against the ground and is detached from the frame, while, in the real experiment, it is tilted forward but still attached to the vehicle frame. This difference is related to the fact that the connections between the rear of the cabin and the frame in the FEM vehicle model fail earlier than those in the experimental vehicle.

Another difference is observed in the final instants of the simulation and regards the movement of the rear of the flatbed. From the 500 ms instant it can be seen that for the FEM model, the flatbed remains in an almost horizontal position and stops against the bollard due to the impact with the rear axle. On the other hand, in the real case, when the rear axle and the bollard come into contact, the impact causes the rotation of the flatbed around the Y axis causing its rear end to rise along the Z axis. This upward movement, which can be observed only for the experimental case, is due to the fact that the impact velocity between the rear axle and bollard is greater than the one recorded in the FEM simulation. This difference can also be related to the different behavior of the cabin: in the simulation, in fact, the overturning of the cabin and its relative crush against the ground suddenly slows down the speed of the whole vehicle and consequently also that of the flatbed. In the simulation, when the rear axle comes into contact with the bollard, the speed of the flatbed is close to 0 m/s and is not sufficient to trigger the rotation and the consequent elevation of the rear of the flatbed.

### 4.1.3 Results comparison – marker M1

The vehicle of the real experiment has some markers for studying the displacements and the velocities of the cabin and the flatbed. In order to compare the kinematic properties of the experimental vehicle through the markers tracking, with the results of the FEM simulation, some measurement points were set on the FEM vehicle cabin and flatbed at the same position of the experimental ones. In the Figure 51 the M1 marker position of the experimental and FEM vehicle is shown.

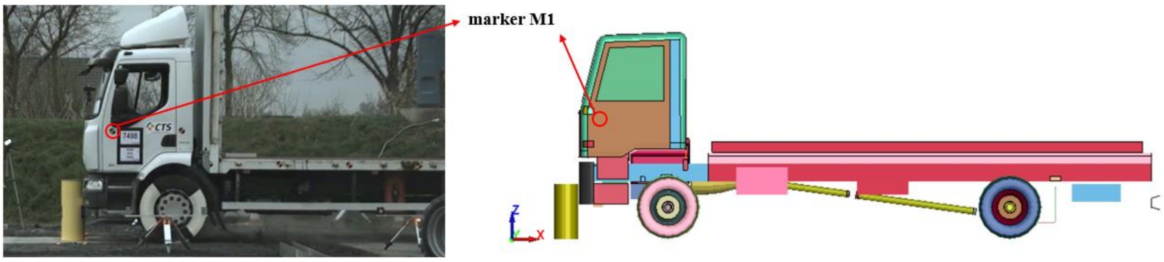

*Figure 51 - Marker M1 on the experimental and FEM vehicle*

Through the use of Tracker software, the displacements and the velocities along the X axis and Z axis of the M1 marker were extracted from the video of the real experiment. After that they are compared with those obtained with the corresponding measurement point placed on the cabin of the FEM vehicle model.

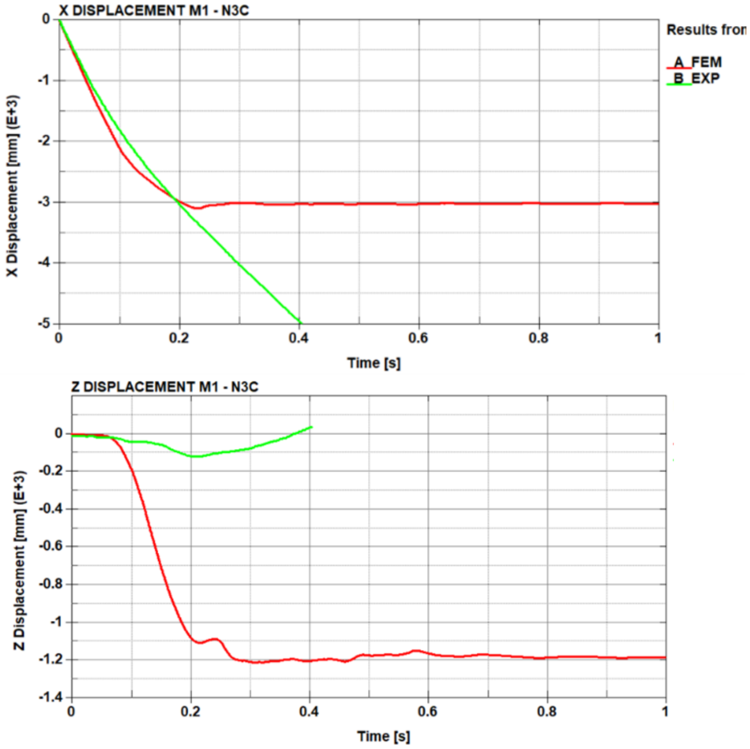

*Figure 52 - Displacement comparison of M1 marker*

From Figure 52, the comparison between the displacements along the X axis and the Z axis of the M1 marker for the experimental case (EXP) and the FEM simulation (FEM) is observed. The origin of the axis reference system is positioned at the center of the marker for both the FEM and EXP cases. The curves of the experimental case stop at 0.4 s because the marker exits from the video frame and cannot be longer tracked by the Tracker software. For the displacement along X a good correlation of the two curves can be observed between 0 s and 0.2 s but, after 0.2 s the curves are not anymore overlapped. This difference lies in the fact that, as observed in Figures 49 and 50 the cabin of the FEM vehicle tilts and hits the ground at t = 0.2 s while that of the experimental vehicle continues its travel along the X axis. As for the displacement along the Z axis the FEM curve tends to decrease rapidly between 0.1 s and 0.2 s since the cabin tilts forward moving toward the ground. The EXP curve does not show the same trend for the reason just described.

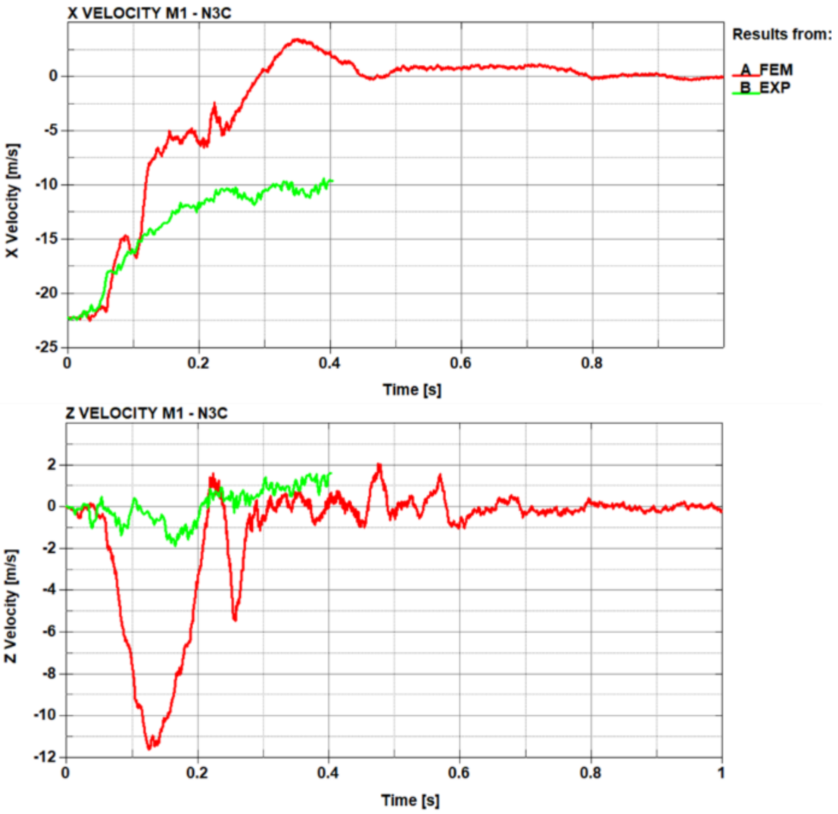

*Figure 53 - Velocity comparison of M1 marker*

Figure 53 shows the comparison between the velocities along the X axis and the Z axis of the M1 marker for the experimental case (EXP) and the FEM simulation (FEM). The comparison of the velocities along the X axis shows that the velocity of the M1 marker of the FEM model reaches the value of 0 m/s faster than the experimental case since at 0.2 s the cabin stops against the ground. The positive values recorded between 0.3 s and 0.4 s are caused by the rebound of some cabin components on the ground. Regarding the velocity along Z the EXP curve tends to oscillate less than FEM curve because the motion of the cabin remains more parallel to the X axis. For what concern the FEM curve, the negative peak recorded at t = 0.16 s is related to the tilting behavior of the cabin and its consequent impact with the ground. The following spikes recorded at t = 0.21 s and 0.25 s are caused by the rebound of doors panels on the ground and the peaks recorded at 0.46 s and 0.57 s are caused by the collision between the flatbed and the tilted cabin. The same analysis was also performed for marker M2, which is also located on the cabin at the same height as marker M1 but shifted in the direction of the flatbed; it can be seen in Figure 51. However, the results were not shown since they led to same conclusions as those described for marker M1.

### 4.1.3 Results comparison – marker M6

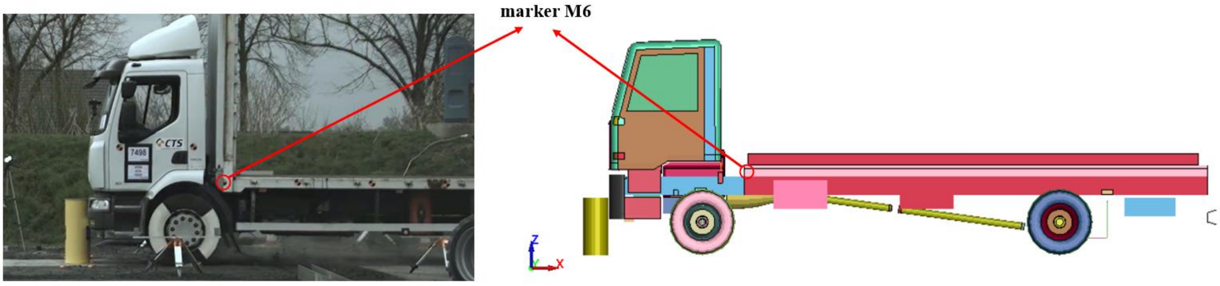

*Figure 54 - Marker M6 on the experimental and FEM vehicle*

Figure 54 shows the M6 marker analyzed that is positioned on the frontside of the flatbed. The origin of the axis reference system is positioned at the center of the marker for both the FEM and EXP cases. The procedure performed to obtain the comparison of the results is the same as shown for the M1 marker.

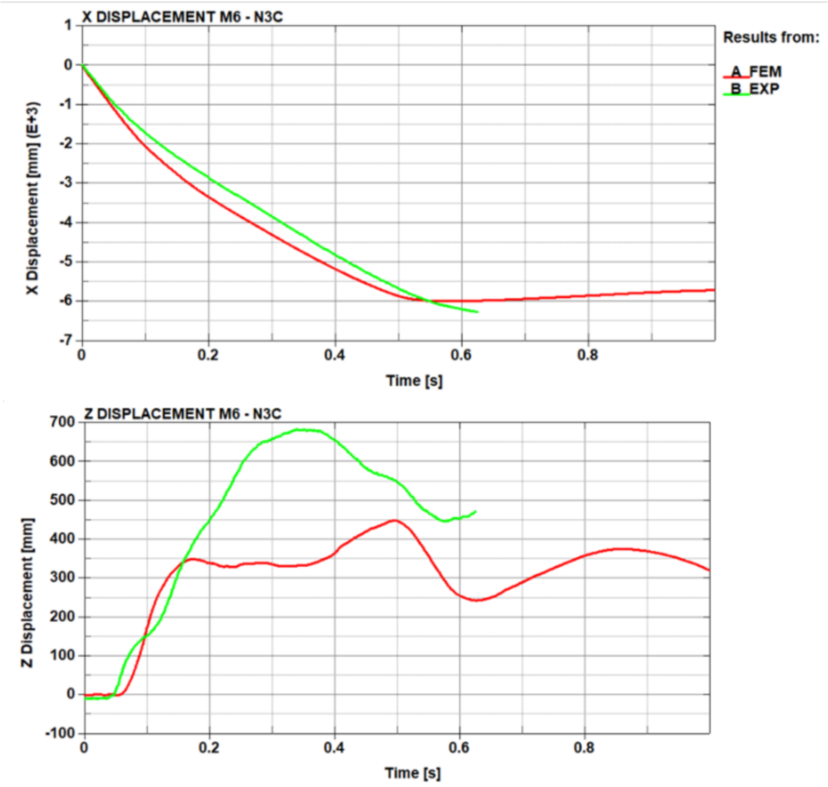

*Figure 55 - Displacement comparison of M6 marker*

In the comparison of the displacement along the X axis, is observed a good correlation between the two curves showing a consistent movement between flatbed for the FEM case with the experimental one. Some differences are observed for the displacement along the Z axis, particularly, after the instant t = 0.2 s, the flatbed the of the experimental vehicle, overcoming the bollard, reaches higher heights along the Z axis than the FEM case. This difference is again attributed to the different behavior of the cabin in the FEM model; after t = 0.2 s it is stopped against the ground and interferes with the forward motion of the flatbed and does not allow it to reach the same value in height that reaches that of the experimental one.

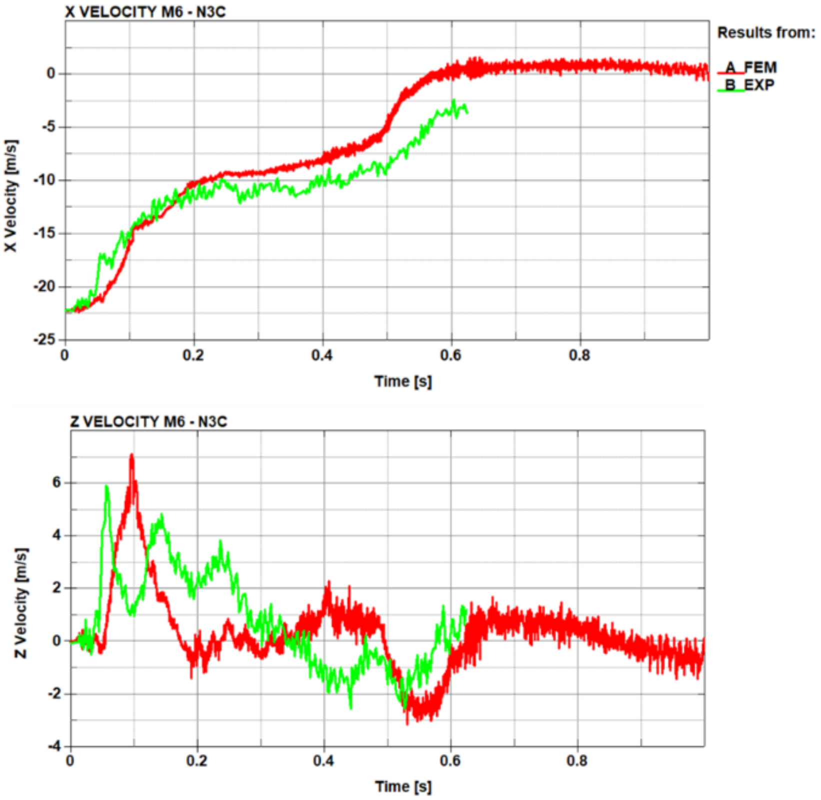

*Figure 56 - Velocity comparison of M6 marker*

The velocities recorded for marker M6 and shown in Figure 56 show a good correlation between the FEM simulation and the experimental case, especially the curves related to the velocity along the X axis. These are similar in terms of trend and, the only difference, is observed for the FEM curve values, which are slightly higher than the EXP ones between 0.4 s and 0.6 s. Regarding the velocity along Z, differences are observed in the distribution of the velocity peaks during the simulation. The first peak is caused by the overcoming of the bollard for both the EXP and FEM cases. In the EXP curve it occurs 0.02 s earlier, than in the FEM curve; after this spike the EXP curve tends to decrease until 0.4 s where it shows a negative peak. The FEM curve, on the other hand, after the first spike remains at values around 0 m/s until 0.4 s where it shows a negative peak similar to the one of the EXP curve. This negative velocity peak corresponds to the instant of the impact between the bollard and the rear axle; this impact causes the flatbed front to lower and consequently the velocity of M6 along Z changes direction.

This analysis was performed in order to test the FEM vehicle model also in case of impact at high speeds against security barrier, since validations had already been performed on experiments of impacts at 48 km/h. The results obtained in this validation involving an impact of the vehicle with a speed at 80 km/h showed differences in the behavior of the FEM model compared to the real one especially regarding the behavior of the cabin. This different behavior can be attributed to the failure, shortly after impact, of the connections between the cabin and the forward tilting of the cabin. In general, for the little information available on the real experiment the validation is acceptable, however, an improvement in terms of stiffness of the connections between cabin and frame is needed if the model is to be used for high-speed impacts; this improvement will be suggested to the model developers.

## 4.2 Bollard position sensitivity analysis

The same N3C category vehicle model (Figures 46) used for the validation shown in Section 4.1 was used for this analysis, which aims to observe the influence that different bollard positions with respect to the symmetry plane (XZ) of the vehicle, have on the impact and on the vehicle deformation. The model set up also includes the creation of a second bollard model; it has a higher height and smaller diameter than the one used in the validation to allow a greater precision in its positioning in the different cases. The bollard will be placed with four different offsets from the plane of symmetry of the vehicle thus proposing four cases of study.

### 4.2.1 Simulation set up

It was decided to model the bollard based on the dimensions of an existing one; the bollard model considered is the following: ALE F16-100-C50 [15]. The FEM model was made with shell elements and the assigned material law was rigid and the material used is steel. The FEM model of bollard used in the simulation is shown in the Figure 57.

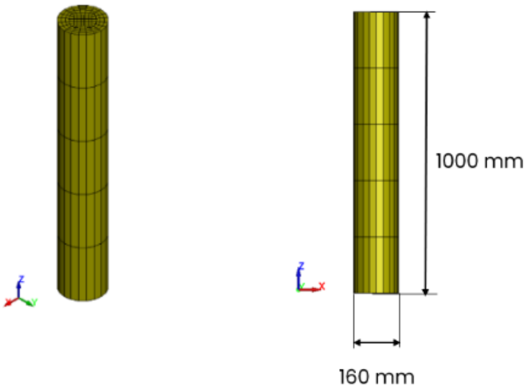

*Figure 57 - Bollard FEM model*

The bollard is placed in four different positions with respect to the symmetry plane (XZ) of the vehicle; the reference case corresponds to the centered bollard where the offset with respect to the XZ plane is 0 mm. The bollard position is gradually moved toward the Y axis by 150 mm, 400 mm and 750 mm. The four cases with the different positions between the bollard and the vehicle are shown in Figure 58.

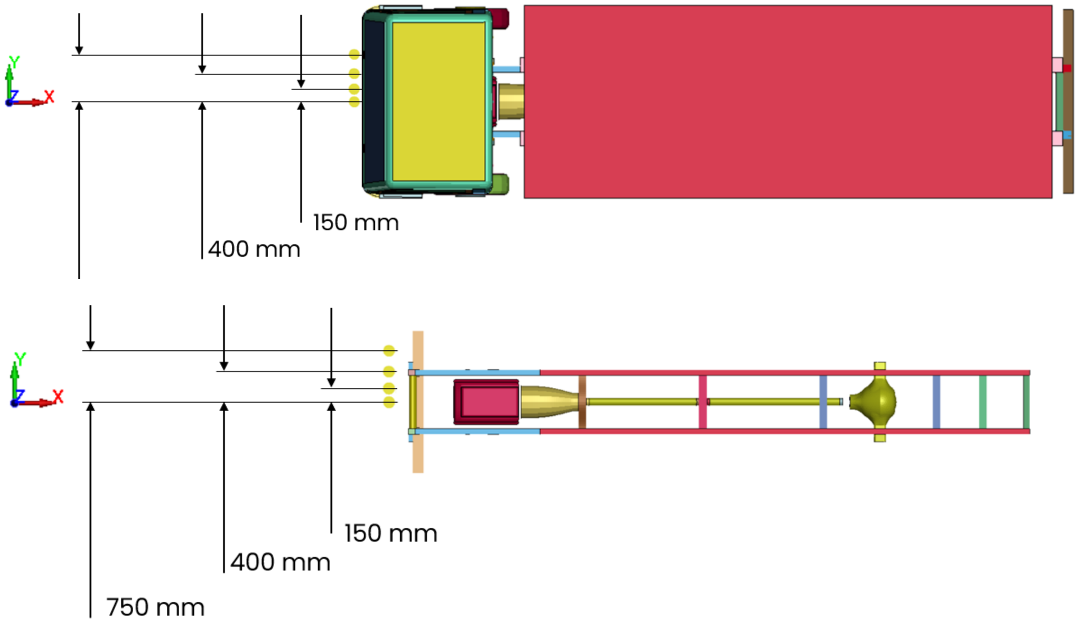

*Figure 58 - Model set up: relative position of the bollard*

The different positions of the bollard were chosen so that the influence of the main components of the vehicle, which are involved in the impact and experience the greatest deformations, could be analyzed. The case with the bollard centered (offset = 0 mm) is considered as the reference case. The bollard shifted by 150 mm was studied with the aim of mainly analyzing the behavior of the engine in an off-center impact case. For the case with offset = 400 mm, the bollard was placed exactly in front of the longitudinal beam to measure the influence the latter has on energy absorption during impact. In the last configuration (offset= 750 mm) the bollard was placed in correspondence to the area of the vehicle between the longitudinal beam and the wheel with the objective of analyzing the contributions, in terms of energy absorption, of the front axle and the front bumper bar.

Regarding the contact between the barrier and the vehicle, the contact penalty formulation chosen is the Pinball one (SOFT = 2). The values of the contact stiffness scale factor were left at the default value (SFS = 1), while the values of the static and dynamic friction coefficients (FS and FD) are both set to the value of 0.3. Finally, the simulation was set in terms of speed and duration. The impact speed is 48 km/h, and it is the same for all the four bollard offset cases. The simulations are run for a duration of 1000 ms.

### 4.2.1 Results comparison

An evaluation of the results was performed by analyzing the animations obtained for each case in order to understand how the vehicle deforms and the differences produced by the various bollard offsets. To simplify the explanation of the results, this analysis shows the time frame in which the front structure is fully crushed against the bollard (t=200 ms) and the last instant of the simulation (t = 1000 ms), where the impact between the vehicle and the bollard is fully completed. For each case, the entire impacted vehicle and a detail on some major internal components are shown. For an easy explanation in the following analyses, the four cases studied will be cited only with the bollard offset values: "0 mm", "150 mm," "400 mm," and "750 mm."

### Bollard offset: 0 mm

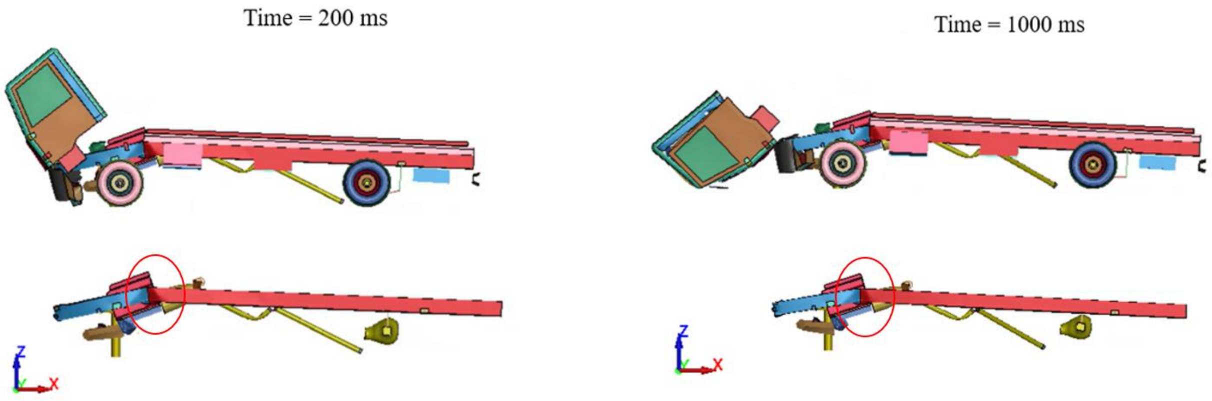

*Figure 59 - 0 mm offset – side view at t = 200 ms and t = 1000 ms*

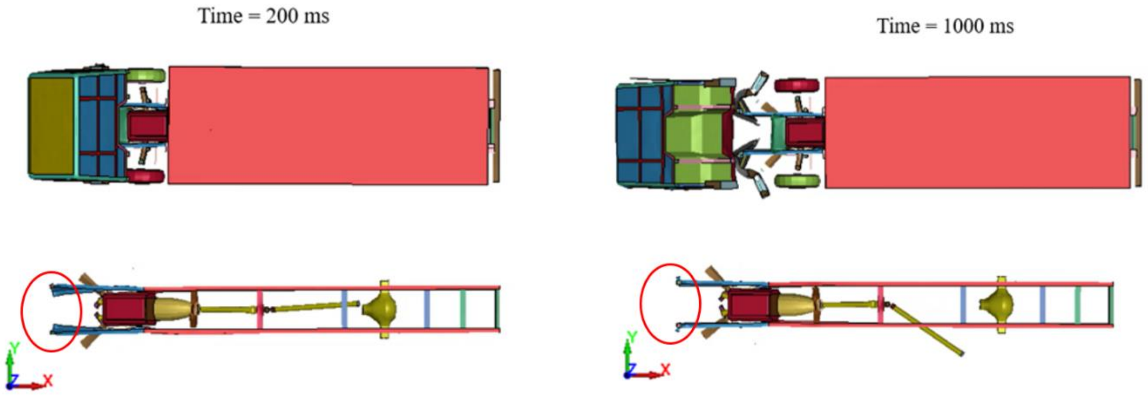

*Figure 60 - 0 mm offset – top view at t = 200 ms and t = 1000 ms*

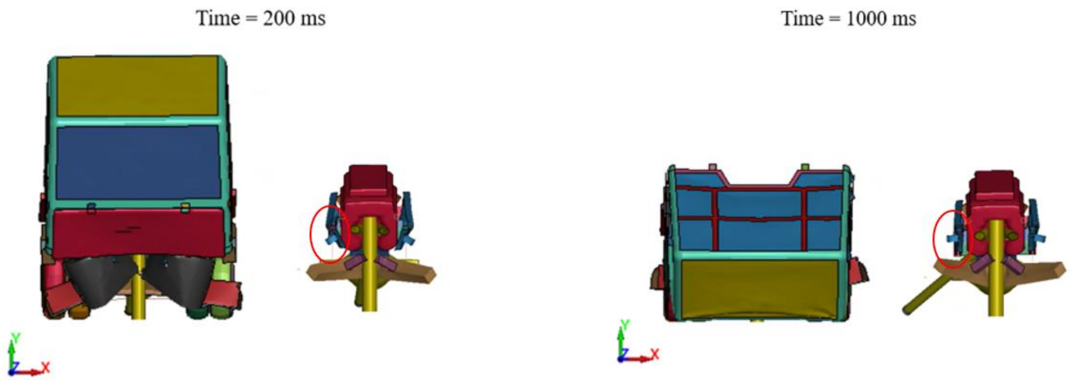

*Figure 61 - 0 mm offset – front view at t = 200 ms and t = 1000 mm*

From Figures 59, 60, 61 can observed the deformation of the vehicle in the impact with the centered bollard and the details related to the frame and powertrain.

Analyzing the side view shown in Figure 59, the following can be noted: at instant 200 ms the rear connections between the cab and the frame have failed and the cab is tilting forward; at instant 1000 ms it is completely crushed on the ground. As for the longitudinal beams, they undergo a bending deformation at the connection between the front longitudinal beams (blue part) and the longitudinal beams (red part). This bending deformation is due to the action of the engine and gearbox, which, impacting against the bollard, tend to rotate forward. This movement is amplified by the fact that the cargo - the rectangular structure in red placed on the flatbed - impacts on the back side of the engine, pushing it forward and accentuating its rotation. In fact, the engine tends to rotate around the Y axis and the rear part of it tends to lift up along the Z axis. Since the engine and the frame are rigidly connected, this motion tends to bend upward the longitudinal beams in the XZ plane.

The behavior of the vehicle from the top view can be observed in Figure 60. From this sight another aspect on the deformation of the front longitudinal beams is recorded. Indeed, at 200 ms after the impact, the front ends of the longitudinal beams tend to move closer to each other while, at the end of the simulation, they return close to a parallel configuration. This movement is due to the deformation of the front bumper bar. This bar is connected to the front ends of the front longitudinal beams and tends to pull them along the X-axis during its deformation. When the simulation is completed, the connections between the front bumper bar and the front longitudinal beams failed and the latter tend to resume a parallel configuration. The longitudinal beams undergo plastic deformation in the XZ plane while elastic deformation prevails in the XY plane.

As regards the front view, it can be observed in Figure 61. From these images it is noted how the longitudinal beams undergo a twist along the X-axis at 200 ms instant; this deformation is not any more visible at the end of the simulation (1000 ms). The reason of this behavior is the same explained in the description of Figure 59.

## Bollard offset: 150 mm

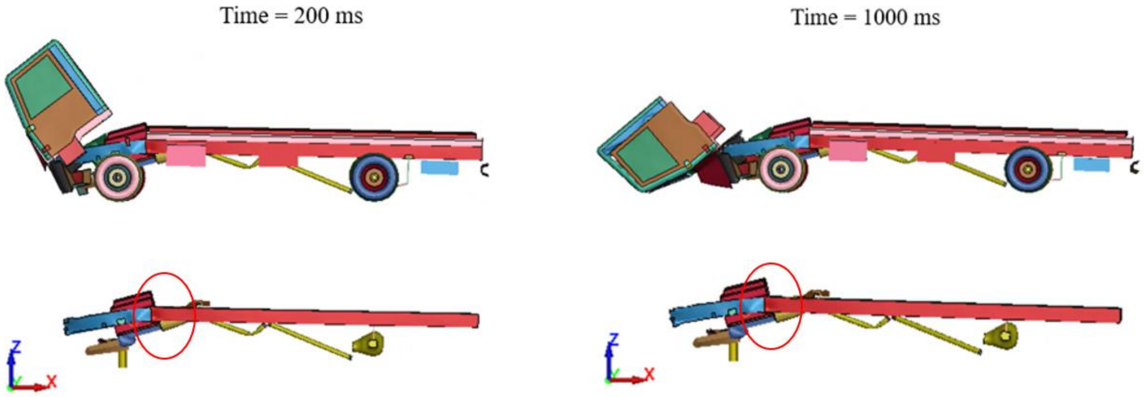

*Figure 62 - 150 mm offset – side view at t = 200 ms and t = 1000 ms*

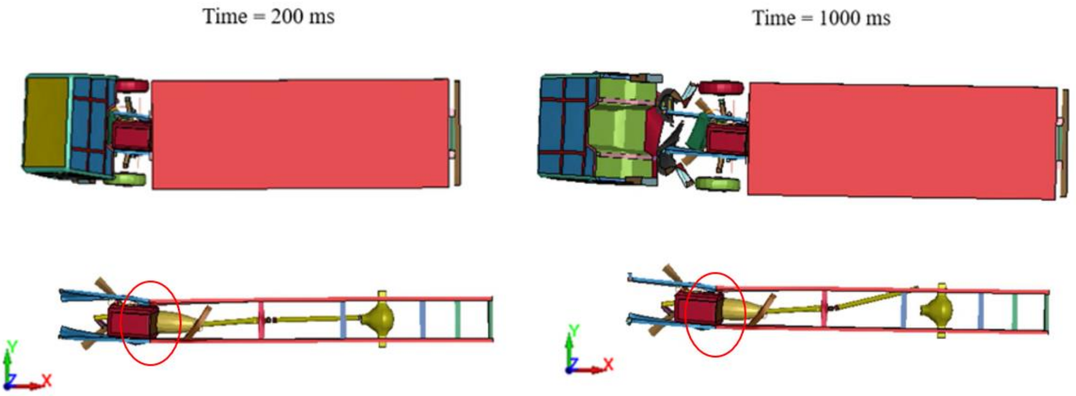

*Figure 63 - 150 mm offset – top view at t = 200 ms and t = 1000 ms*

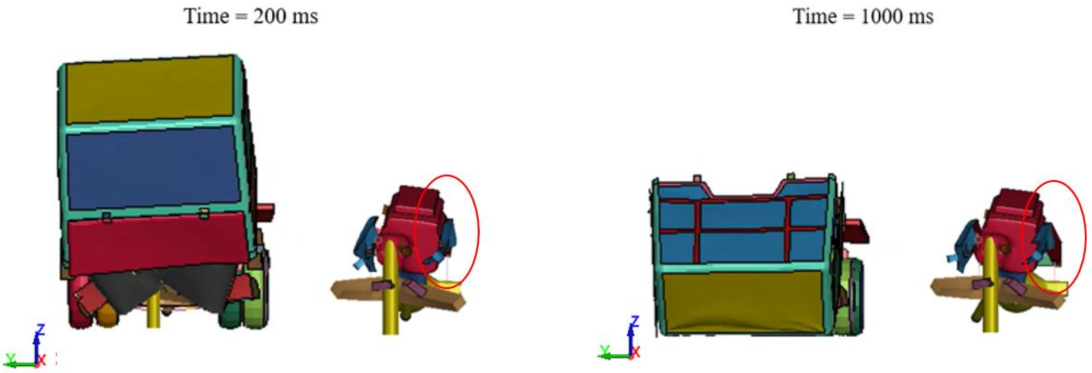

*Figure 64 - 150 mm offset – front view at t = 200 ms and t = 1000 ms*

Figures 62, 63 and 64 show the deformations recorded for the case where the bollard is displaced 150 mm along the X axis from the centered position (Figure 58).

From Figure 62, the deformation can be observed from a side view. In this view, the behavior of the cabin appears to be similar to that seen for the "0 mm" case. One difference is noted in the deformation of the longitudinal beams. The deformation, in terms of bending, turns out to be less pronounced than in the previous case. This variation is due to the different behavior of the engine and the gearbox during the deformation. In fact, they tend to rotate around the Y axis but the rear part of both reaches a lower height along the Z axis than in the "0 mm" case.

The top view of the vehicle deformation is shown in Figure 63. Since the bollard is positioned with an offset of 150 mm, it impacts the right side of the engine. The off-centered collision causes the engine to rotate not only around the Y axis but also around the Z axis. The engine and the gearbox are then pushed against the left longitudinal beam of the frame. This displacement causes the bending deformation of the longitudinal beams in the XY plane as well. A similar behavior to the one observed for the "0 mm" case is noted for the front ends of the front longitudinal beams.

Figure 64 shows the impact from a front view. It can be evaluated how the engine is displaced against the left longitudinal beam causing its deformation, which reflects also on the right one. Moreover, it can be seen how the impact of the bollard occurs in the lower right area of the front side of the engine. This also causes the engine to rotate about the X axis. The deformation of the cabin differs from the "0 mm" case: in fact, it undergoes not only a rotation around the Y axis, but also a rotation around the X axis given by the different deformation of the longitudinal beams.

### Bollard offset: 400 mm

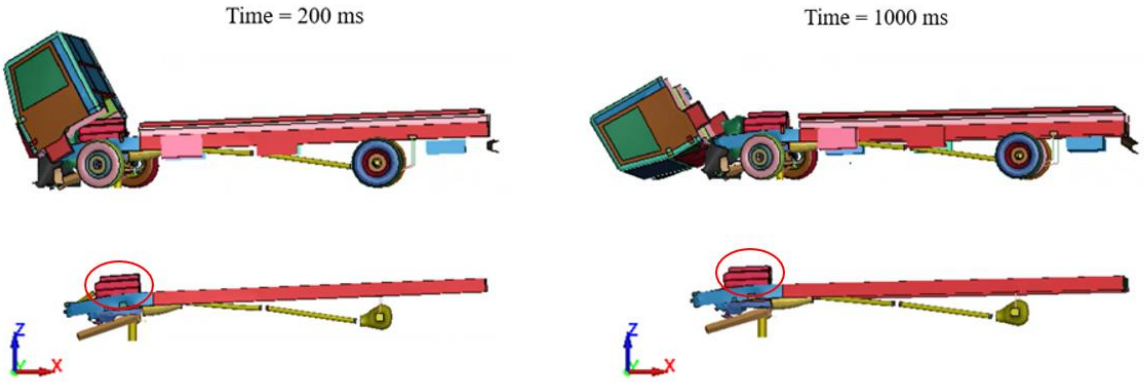

*Figure 65 - 400 mm offset – side view at t = 200 ms and t = 1000 ms*

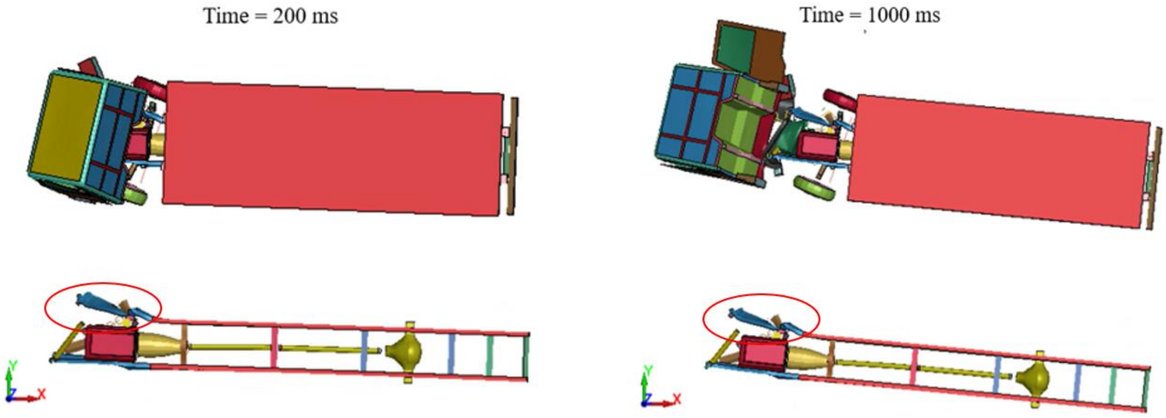

*Figure 66 - 400 mm offset – top view at t = 200 ms and t = 1000 ms*

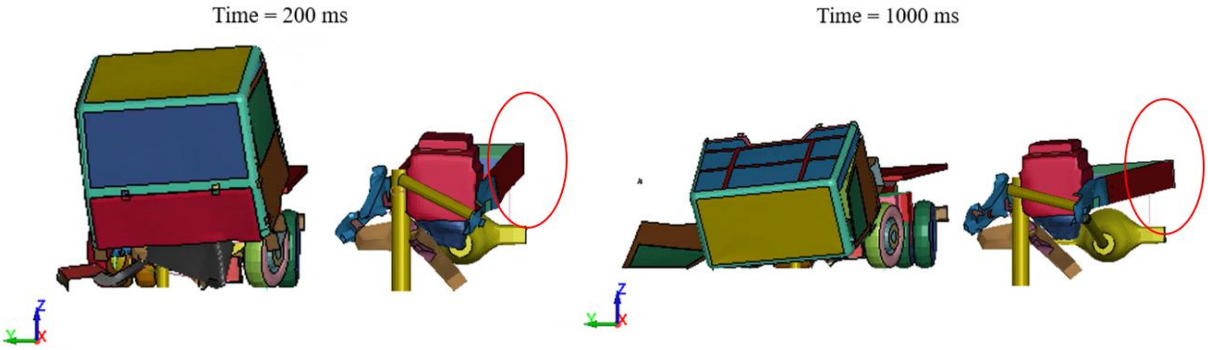

*Figure 67 - 400 mm offset – front view at t = 200 ms and t = 1000 ms*

Figures 65, 66 and 67 show deformations of the vehicle when it impacts against the off-centered bollard by an offset of 400 mm. In this case the bollard is positioned exactly in front of the right longitudinal beam (Figure 58).

From Figure 66, two instants of the simulation can be observed from a side view; the first differences from the "0 mm" and "150 mm" cases can be seen in the movement of the cabin, in the deformation of the longitudinal beams and in the deformation of the engine. The latter does not impact directly against the bollard, as for the two cases previously analyzed, but hits the bollard only with its right side. This lateral impact with the bollard reduces drastically the engine and gearbox rotation around the Y axis; in fact, the engine maintains a position almost parallel to the XY plane. The non-rotation of the engine results in a lower bending deformation of the longitudinal beams in the XZ plane than in the "150 mm" case. As for the cabin, not only a rotation around the Y axis but also around the Z axis is observed.

The deformation of the right longitudinal beam can be clearly visible from the top view in Figure 67. Indeed, the front longitudinal beam is crushed on itself by the impact with the bollard; it crushes the front end of the beam and pushes it outward and then penetrates between the beam and the side of the engine. Between the time instant t = 200 ms and the final instant, it is observed that the whole vehicle has made a rotation around the Z axis. This rotation is due to the fact that the bollard positioned itself between the longitudinal beam and the engine stopping on the front axle. In this way it acts as a fulcrum triggering the rotation of the frame and thus the whole vehicle.

Figure 68 shows the frontal view of the impact. The yaw rotation of the vehicle can be seen from the difference in position of the rear part of the frame between the instant t=200 ms and the final instant. The crushing of the front longitudinal beam and its deformation in the y-direction can be better appreciated.

## Bollard offset: 750 mm

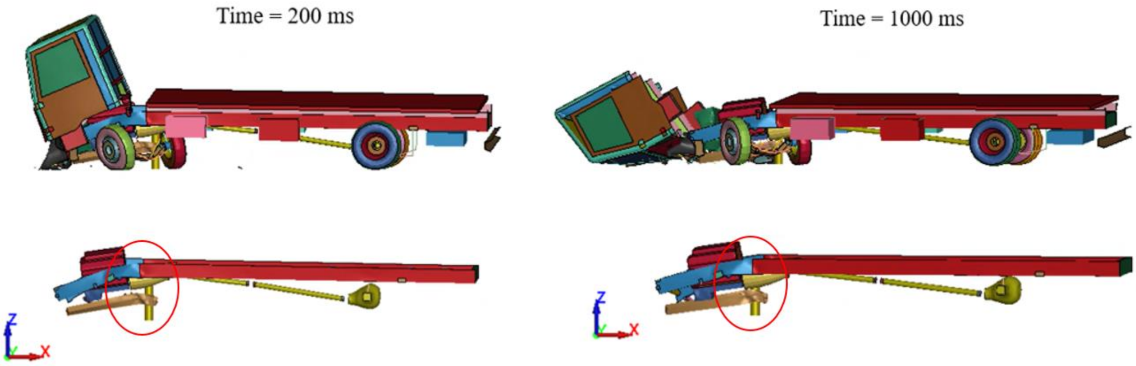

*Figure 68 - 750 mm offset – side view at t = 200 ms and t = 1000 ms*

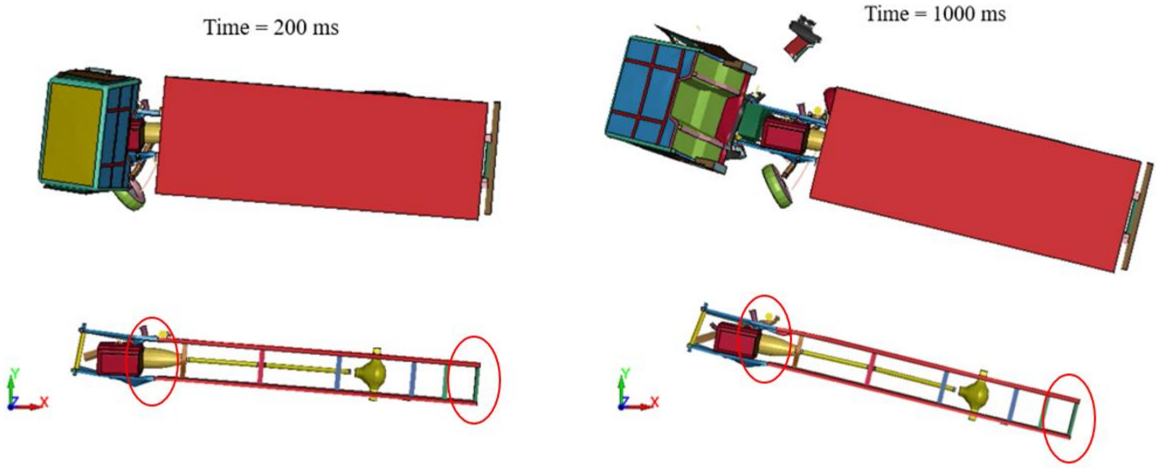

*Figure 69 - 750 mm offset – top view at t = 200 ms and t = 1000 ms*

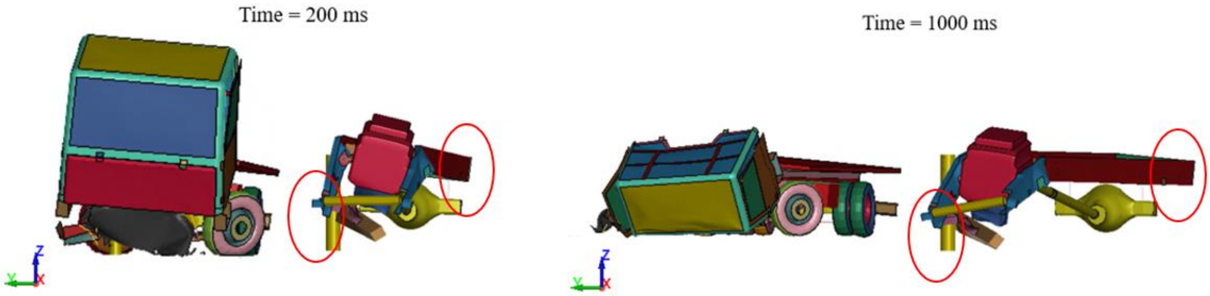

*Figure 70 - 750 mm offset - front view at t = 200 ms and t = 1000 ms*

The study with the bollard off-center and displaced from the central position by 750 mm is shown in Figures 68, 69 and 70. This is the case where the vehicle hits the bollard at the area between the longitudinal beam and the right wheel (Figures 58).

Figure 68 shows the side view of the impact. It can be seen that the engine has a similar behavior to that described for the "400 mm" case. Again, the reason for the engine movement is due to the fact that the engine and bollard do not come into direct contact. However, it is observed that the bending deformation of the longitudinal beam appears to be more pronounced than in the "400 mm" case. It bends upward just before the junction zone between front longitudinal beam (blue part) and the longitudinal beam (red part)

From Figure 69, where the top view is shown, the bollard impacts against the right longitudinal beam on the outer side. This impact crushes and deforms both the front axle and the right longitudinal beam against the engine. The engine pushes against the left longitudinal beam causing it to deform in the XY plane. The main difference with the other cases is the rotation that the vehicle performs around the Z axis. The front bumper bar and the front axle act as arm and the inertia of the vehicle causes a torque that induces a yaw rotation of the vehicle. In this case the rotation is more pronounced than in the "400 mm" case.

From Figure 70, the impact is observed from a frontal view. Also from this sight, the rotation of the vehicle around the Z axis can be observed form the different position of the rear of the vehicle between instants t = 200 ms and the final instant. It is also noticeable how the frame in this case is subjected to a torsional moment around the X axis. Indeed, it can be seen how, at the final instant, the front right longitudinal beam is at a lower height than the left one. This is due to the deformation of the front bumper bar and the connecting element between it and the longitudinal beam. The front bumper bar undergoes significant deformation along X axis and pulls the front end of the longitudinal beam downward, triggering a torsion moment of the frame.

## 4.2.2 Energy components

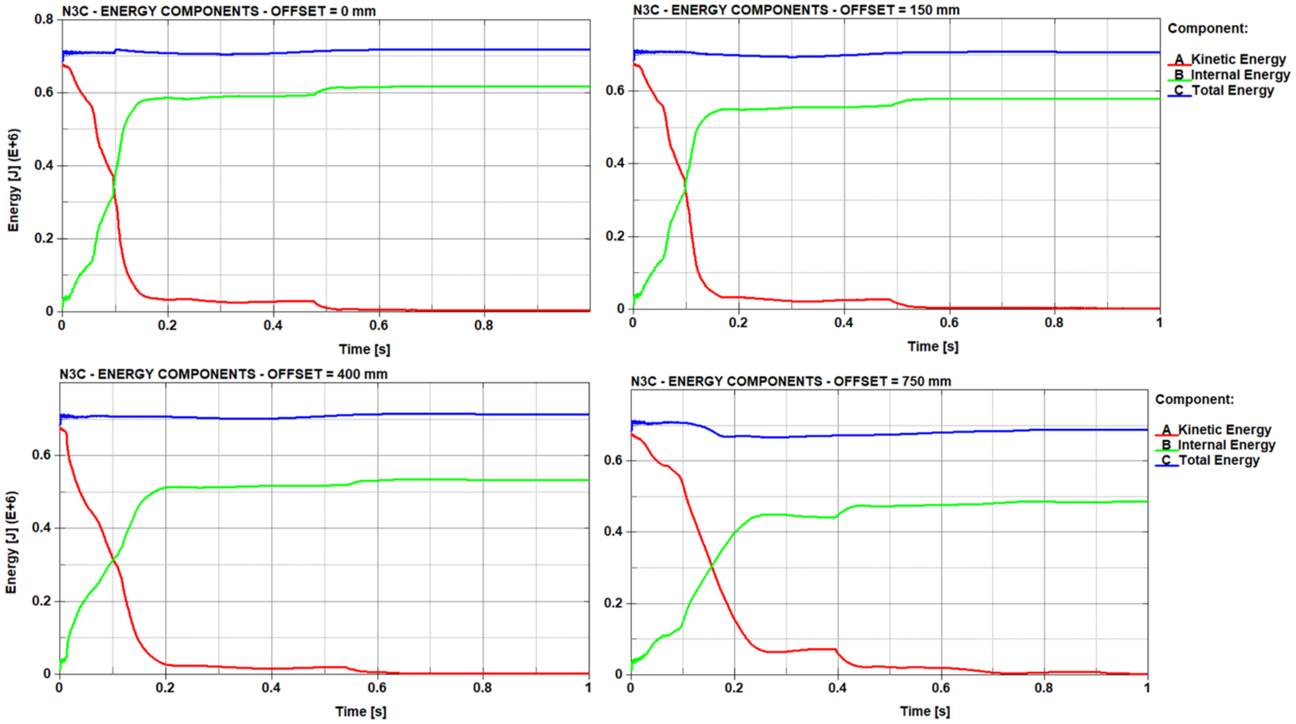

*Figure 71 - Energy components*

Figure 71 shows the energy components recorded for each case. The internal energy trend shows a sharp increase between 0 and 0.2 s, which corresponds to the instant when the frontal structure of the vehicle has completed its impact against the bollard. After 0.2 s the internal energy tends to almost constant values. As far as kinetic energy is concerned, it mirrors the internal energy due to the energy balance principle. It decreases almost linearly between 0 and 0.2 s; at this instant the velocity of the vehicle is very close to 0 m/s. As for the total energy, it tends to stand at a constant value throughout the duration of the simulation. It means that other energy components, like the hourglass energy, are low enough not to impact on results. The overall trends of the internal, the kinetic and the total energy are similar among the "0 mm", "150 mm" and "400 mm" cases. Some differences are observed in the "750 mm" case where lower internal energy values and higher kinetic energy values are reordered. The total energy also undergoes a decrease at the instant t = 0.2 s. On the following pages there is a specific comparison analysis of the different cases in terms of internal energy, kinetic energy, total energy, X momentum and X force.

### Internal energy

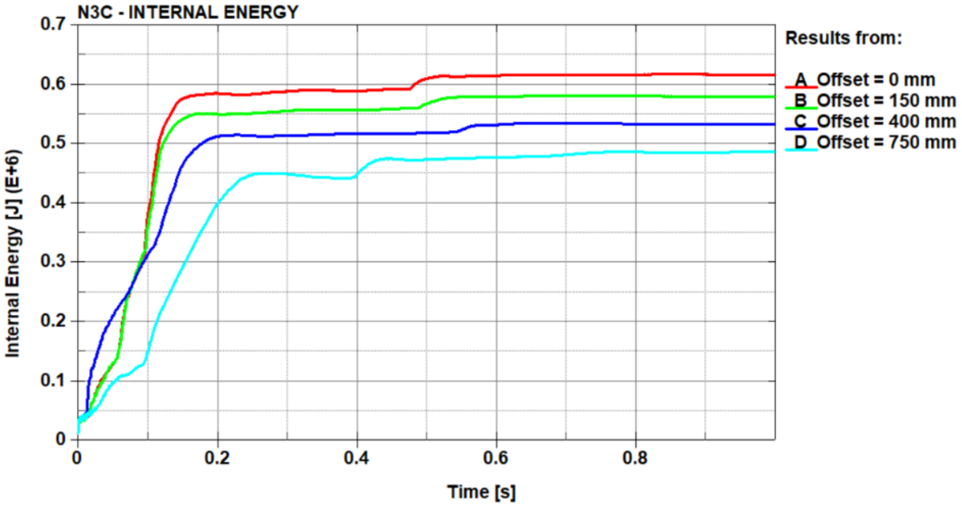

*Figure 72 - Internal energy comparison*

Figure 72 shows the internal energy curves recorded for each case. For the "0 mm" and "150 mm" cases, the energy curves grow rapidly between 0 and 0.17 s. After this last instant, the curves tend to constant values. For the "400 mm" case the internal energy grows rapidly between 0 and 0.19 s; after the 0.19 s. it also tends to constant values. A similar trend is observed for the "750 mm" case. In the latter, the curve flattens out after 0.21 s. Overall, it can be said that all four curves grow until t = 0.2 s; this instant corresponds to the time when the front structure is fully crushed against the bollard. After the growth, the curves flatten but all show a slight rapid growth that occurs around the middle of the simulation. This slight growth corresponds to the instant when the cabin, which tilts, hits the ground deforming itself. For the “0 mm” and “150 mm” cases this slight growth is recorded at t = 0.5 s while for the “400 mm” study around the instant t = 0.55 s. The greatest difference is observed for the “750 mm” event: the energy growth, due to the cabin impact, occurs earlier (at t = 0.4 s) than the other three cases. This difference is due to the fact that, as observed in Figures 62, 63 ,64 the vehicle undergoes considerable rotation about the Z axis which causes the cabin to crush earlier against the ground rather than the other cases. It is clearly visible how as the bollard offset increases, the internal energy tends to decrease and reduces to lower values. This variation is associated with the different deformation that the components undergo for each case. For the "0 mm" study, the engine is the element that most affects the absorption of internal energy. The same observation can be made for the "150 mm" event; in this case the internal energy is slightly lower than in the case with the centered bollard. For the "400 mm" study, the energy absorbed by the vehicle during deformation is lower than for the "0 mm" and "150 mm" cases. In the "400 mm" event, in fact, the engine plays a marginal role in terms of deformation since it hits the bollard glancingly and only with the right side. In such case, the component that has the greatest impact on the internal energy is the front longitudinal beam, which records the maximum deformation. In the "750 mm" study, the overall vehicle deformation, and consequently the internal energy, appears to be the lowest compared to the other 3 cases. This is due to the fact that neither the engine nor the longitudinal beams come into direct contact with the bollard; the main contributions in terms of internal energy come from the deformations of the front bumper bar and the front axle.

### Kinetic energy

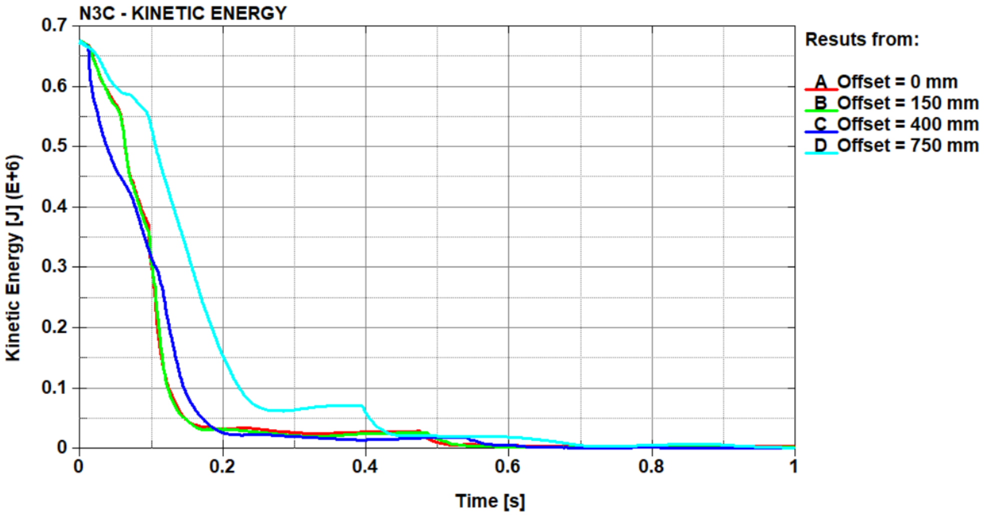

*Figure 73 - Kinetic energy comparison*

The graphs for the kinetic energies corresponding to each study are plotted in Figure 73. The curves for the cases "0 mm", "150 mm", and "400 mm" appear to be very similar to each other and in several sections appear to be superimposed. These three graphs tend to decrease very rapidly between 0 s and 0.2 s; after the instant t = 0.2 s the trends of the kinetic energies remain at almost constant values until the instant t = 0.5 s. Between 0.2 s and 0.5 s, the kinetic energy curves show values with an order of magnitude lower than the starting ones. Around the instant t = 0.5 s the curves tend to decrease again and reach values with 2 orders of magnitude lower than the starting value. This second reduction corresponds to the moment when the cabin crashes into the ground. This impact reduces the vehicle speed, which reaches values close to 0 m/s at the end of the simulation. As for the curve of the "750 mm" simulation, it shows a similar trend to those of the other cases with the difference that its averages values are higher throughout the duration of the simulation. In this study, given the high offset value, the bollard takes longer to totally stop the vehicle and induces a yaw rotation of the vehicle. The rotation around the Z axis causes the kinetic velocity value to be higher in the section between 0.2 s and 0.4 s than in the other three cases. At 0.4 s there is the impact of the cabin with the ground, which corresponds to a decrease in kinetic energy. After the collision of the cabin, the flatbed continues its rotation keeping the value of kinetic energy almost constant between 0.4 s and 0.5 s. At t = 0.6 s the kinetic energy reaches values similar to those recorded for the other cases and then assumes values close to 0 J at the end of the simulation.

### Total energy

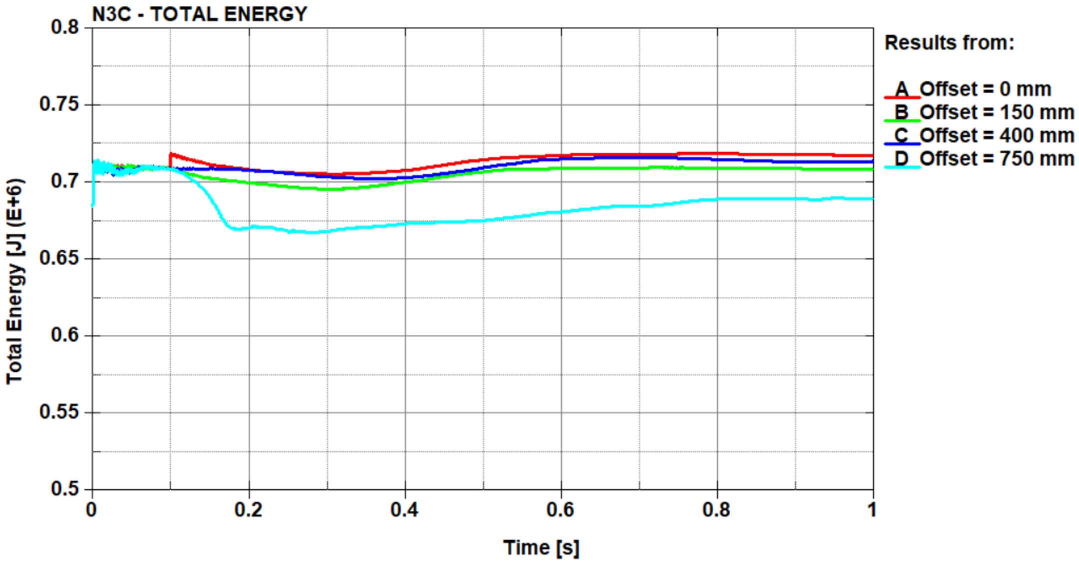

*Figure 74 - Total energy comparison*

Figure 74 shows the curves for the total energy. It is observed that the curves tend to decrease in value as the offset value increases. Similar behavior to that is observed for the internal energy. For the "0 mm", "150 mm" and "400 mm" cases, the curves are found to be similar in values during all the simulation. The main difference is observed for the “750 mm” study, which shows a decrease at the 0.16 s instant. The reason why the total energy for this case is significantly lower than for the other three cases is because the overall vehicle deformation recorded is lower than all the other three cases.

### X momentum

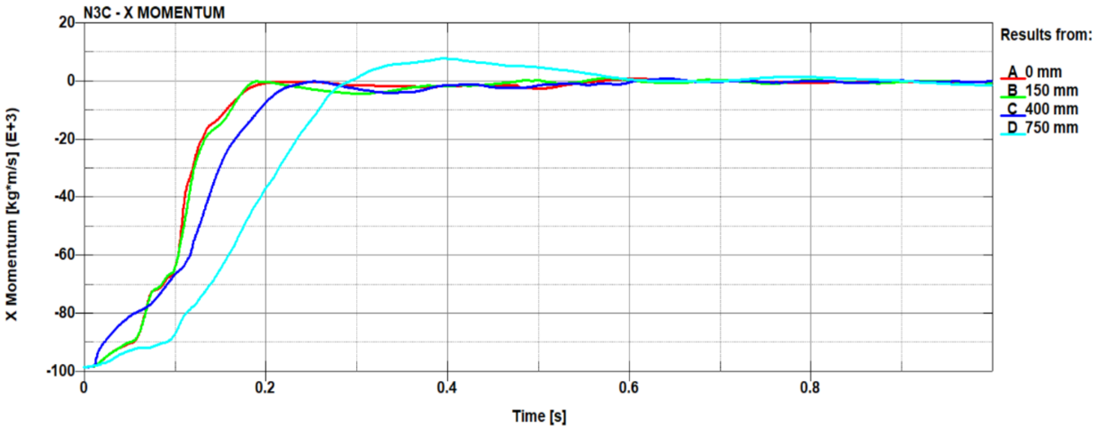

*Figure 75 - X momentum comparison*

The X momentum recorded in the four simulations is shown in Figure 75. The curves obtained from "0 mm," "150 mm," and "400 mm" simulations show similar trend between each other; they increase between 0 and 0.2 s and then reach values close to 0 for the rest of the simulation. The curves start from negative values since the direction of vehicle movement is in the opposite direction of the X axis. For the "0 mm" and "150 mm" cases, the curves are very similar to each other and are almost totally overlapping. They reach values close to 0 for the instant t = 0.19 s. As for the "400 mm" simulation, in the section between 0 s and 0.2 s the curve appears to be more shifted to the left than the previous cases. This difference shows how the vehicle takes longer to slow down and stop. In fact, the value of 0 kg·m/s is reached at the instant of 0.25 s; after this time the curve also reaches values close to 0. The "750 mm" simulation is shifted to the left more than the "400 mm" case. As mentioned earlier, this is the case in which the vehicle takes the longest time to slow down and stop. It reaches the null value at t = 0.3 s; after this instant, it is observed that the curve takes positive values in the segment from t = 0.3 s to t = 0.6 s. The positivity of the values in this section shows that the flatbed not only rotates around the Z-axis but also performs a translation in the same direction of the X-axis. In fact, after the cabin has detached and crashed on the ground, the flatbed bounces against the bollard moving in the opposite direction compared to before the impact. The motion stops at the t = 0.6 s instant, and the curve decreases to similar values of the other cases.

### X Force

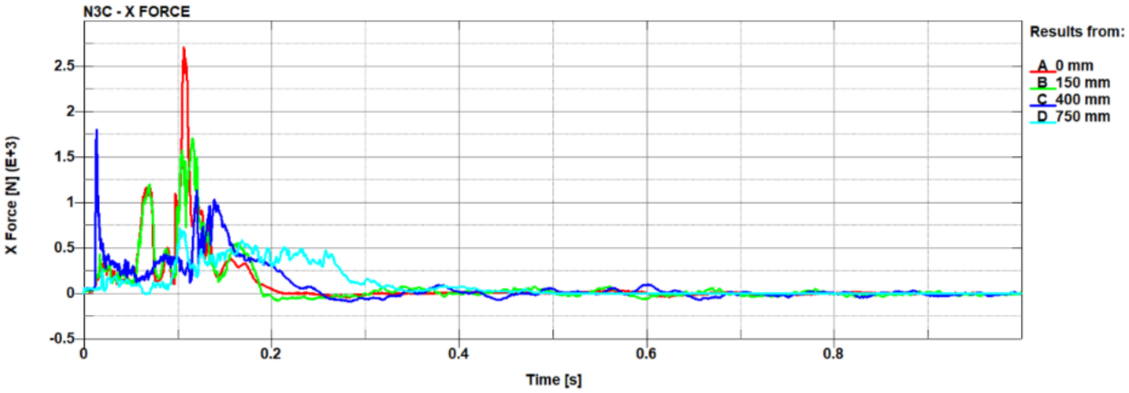

*Figure 76 - X force analysis*

Figure 76 shows the trend of the force that is exchanged, along the X axis between the vehicle and the bollard during impact. In this case, the force exchanged along the X axis was analyzed since the impact between the bollard and the vehicle occurs at an angle of 90° and along the direction of the X axis. From the evaluation of the X force, it can be inferred which of the four cases is the most penalizing for the bollard. In terms of the curve's trends, all four cases show several force peaks distributed over the range from 0 s to 0.2 s. This means that, most of the force is discharged on the bollard during the crushing phase of the vehicle's front. Once this phase is completed, the force tends to decrease and tends to values close to 0 N. Only for the "750 mm" case the X force take longer to decrease to negligible values, which are reached around 0.3 s.

Figure 77 shows the X force trend with a magnification between 0 s and 0.4 s; in this way the force peaks recorded for each case can be analyzed and compared in greater detail. In order to better understand the nature of the force peaks, some pictures of the frame and engine deformation, which correspond to the time instants at which the main force peaks are recorded, have been shown for each case.

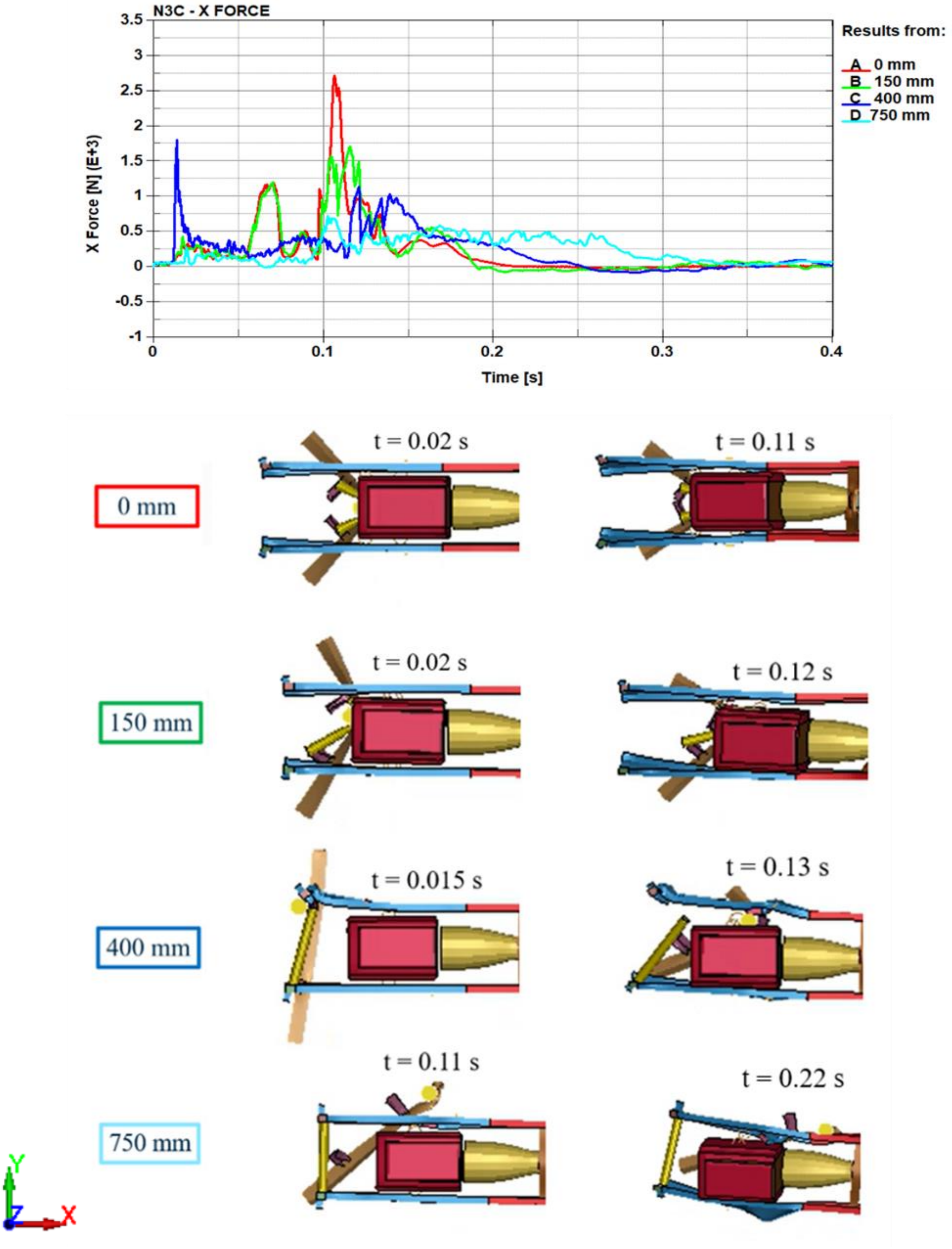

*Figure 77 - X force peaks analysis*

Analyzing the "0 mm" case, it can be seen that the curve has two distinct force peaks. The first is recorded at 0.07 s while the second is at 0.11 s. The first force peak (t= 0.7 s) is caused by the impact between the bollard and the front side of the engine. This peak reaches 1200 N. The second peak occurs at 0.11 s, and the reason for this second peak is less trivial; in fact, it is caused by the impact between the cargo, positioned on the flatbed, and the rear side of the engine. In the description of Figure 62, it was analyzed how, due to the deformation of the frame, the cargo impacts on the engine and crushes it further against the bollard. Indeed, it is observed from Figure 77 how, at t=0.11 s, the engine is rotated more forward than at the instant t = 0.02 s. Since the cargo has a mass of 2610 kg, the inertia force transmitted to the engine, causes a sudden increase in the X force. This peak reaches the highest value of all four cases, which is 2750 N. However, it is necessary to point out that if the cargo changes in terms of position, shape or mass, this behavior would no longer be evident and the force peak would not be present or would be present with a different value.

As for the "150 mm" case, it shows a peak at the 0.07 s instant that is extremely similar to that observed for the "0 mm" simulation; it is, in fact, caused by the impact between the bollard and the front side of the engine. Similar behavior to that described for the "0 mm" case is also seen for the peak recorded at t = 0.11 s. In this case, however, the peak force appears to be lower and less defined. The cause of this difference can be related to the fact that the bollard hits the engine on the right side causing it to move against the left longitudinal beam. The cargo no longer impacts perpendicularly against the rear face of the engine, which is found to be slightly rotated, and the peak force transferred to the bollard is therefore lower in magnitude (1700 N).

For the "400 mm" case, the peak force occurring at 0.015 s is caused by the impact between the bollard and the front longitudinal beam. It crushes itself by impacting against the bollard and, since the front longitudinal beam is a structural element with a high stiffness, it transfers a force of 1800 N to the bollard. After this instant the front long beam is deformed outward and the bollard slides between the longitudinal beam and the engine. When the bollard comes in contact with the front axle there is the second force peak (t = 0.13 s) which has a value of 1150 N. If the cargo had a different shape or mass and the peak recorded for the "0 mm" case at t = 0.11 s was not present, the peak of force shown by the "400 mm" case at t = 0.015 would have been the highest value among all cases.

In the "750 mm" case, the X force presents significantly lower values since the bollard does not come into direct contact with either the engine or the longitudinal beam. The first peak is recorded at the instant t = 0.11s. The bollard, in fact, after deforming the front bumper bar, impacts against the front axle. After this peak (from instant t = 0.15 s to instant 0.25 s) the force oscillates between the value of 400 N and 500 N. This time segment corresponds to the phase in which the right longitudinal beam impacts and deforms itself against the bollard. During this deformation, the front axle continues to be deformed through a rotation around the Z axis.

## 4.2.3 Results comparison - vehicle components

In the following section, some structural components of the vehicle will be analyzed in detail. In particular, their contribution in terms of internal energy and plastic strain for each bollard offset case will be studied. The components chosen are those that have an internal energy value greater than the 5 % of the total internal energy, in one or more of the cases of study. The elements considered are the engine, the front longitudinal beams, the fan and filter, the front bumper bar and the front axle. These components are shown in Figure 78; where, for each component analyzed, the material law and the material physical properties have been indicated in order to better understand the plastic strain analysis that will follow.

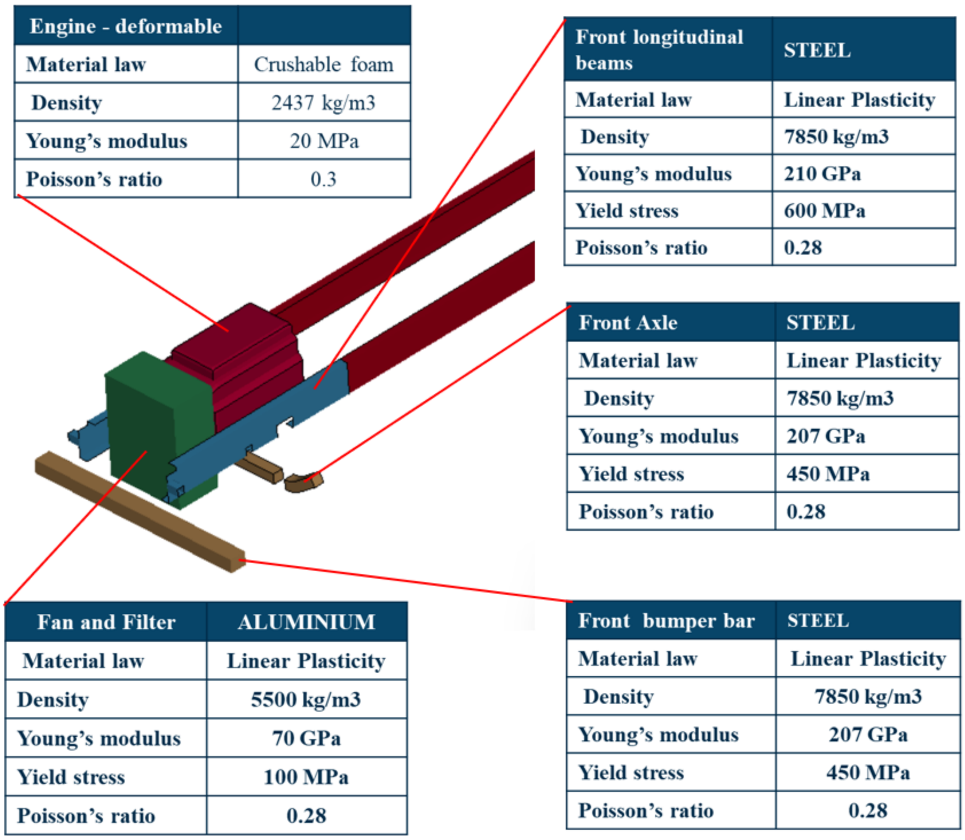

| **Engine - deformable** | |
|---|---|
| **Material law** | Crushable foam |
| **Density** | 2437 kg/m3 |
| **Young's modulus** | 20 MPa |
| **Poisson's ratio** | 0.3 |

| **Front longitudinal beams** | **STEEL** |
|---|---|
| **Material law** | **Linear Plasticity** |
| **Density** | **7850 kg/m3** |
| **Young's modulus** | **210 GPa** |
| **Yield stress** | **600 MPa** |
| **Poisson's ratio** | **0.28** |

| **Front Axle** | **STEEL** |
|---|---|
| **Material law** | **Linear Plasticity** |
| **Density** | **7850 kg/m3** |
| **Young's modulus** | **207 GPa** |
| **Yield stress** | **450 MPa** |
| **Poisson's ratio** | **0.28** |

| **Fan and Filter** | **ALUMINIUM** |
|---|---|
| **Material law** | **Linear Plasticity** |
| **Density** | **5500 kg/m3** |
| **Young's modulus** | **70 GPa** |
| **Yield stress** | **100 MPa** |
| **Poisson's ratio** | **0.28** |

| **Front bumper bar** | **STEEL** |
|---|---|
| **Material law** | **Linear Plasticity** |
| **Density** | **7850 kg/m3** |
| **Young's modulus** | **207 GPa** |
| **Yield stress** | **450 MPa** |
| **Poisson's ratio** | **0.28** |

*Figure 78 - Studied components and relative material properties*

### Engine deformable

The vehicle engine consists of two components: a rigid rectangular solid element (engine rigid) and an outer solid deformable part (engine deformable). The inner element is not subject to deformation while the outer element (engine deformable) is modeled as a crushable foam. The Figure 79 shows the two elements that built the FEM engine model through a section along the XZ plane: the engine deformable (part 1) e engine rigid (part 2). This particular modeling was defined during the vehicle testing where it was found that a rigid part may cause a significant contact force peak when the vehicle impacts to the barrier. To avoid this spike, the external deformable part was introduced and it covers the rigid engine block. The role of this part is to imitate the deformable behavior of the softer parts which are located in the surroundings of the engine (plastic covers, hoses, tubes, valves, hoses, clamps etc.). This part uses crushable material model with nonlinear bulk stiffness [10]; the material stress - plastic strain curve is shown in Figure 80.

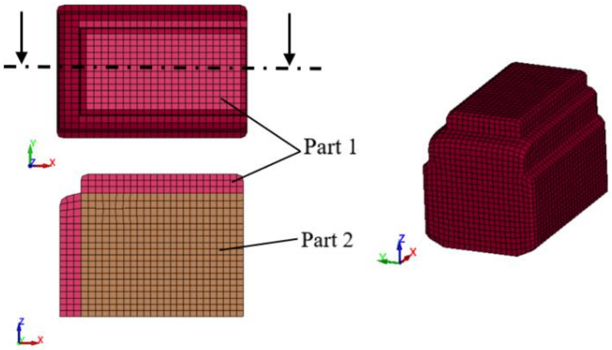

*Figure 79 - FEM engine model parts*

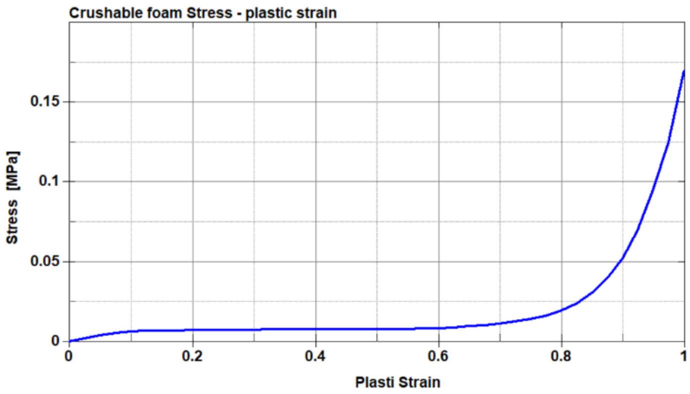

*Figure 80 - Crushable foam stress- plastic strain curve*

Considering what has just been said, it was decided to analyze the deformable engine by studying its absorbed internal energy and the reported deformations for each case.

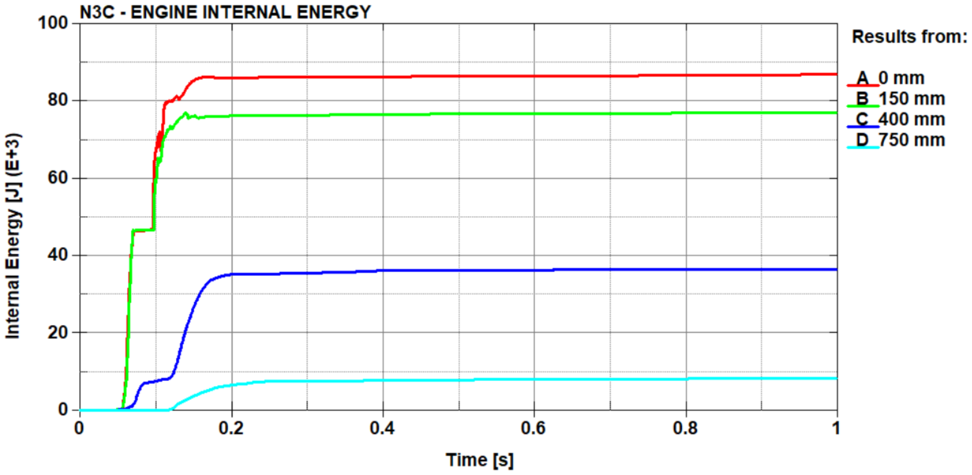

*Figure 81 - Engine deformable - internal energy comparison*

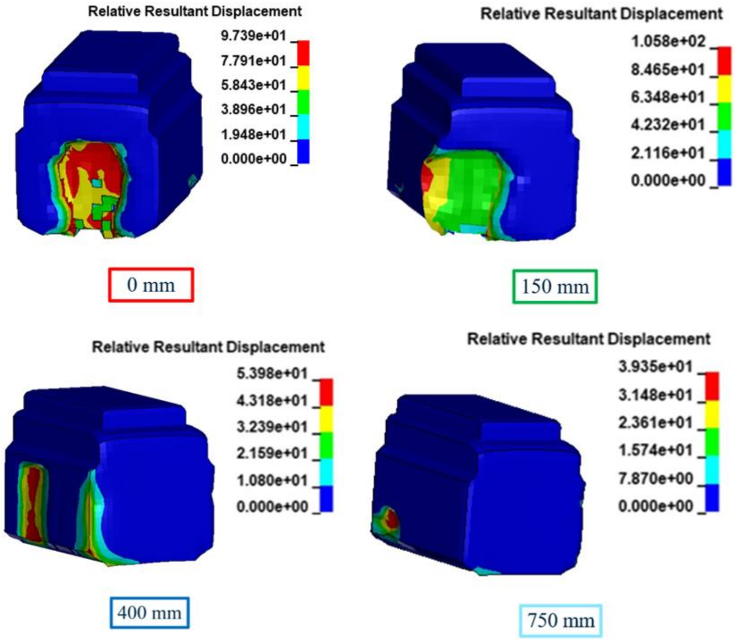

*Figure 82 - Engine elements displacement*

Figure 81 shows the trends of the internal energy recorded by the engine deformable for each bollard offset. A similar trend is observed in Figure 82 about the total energy of the vehicle: the energy values tend to decrease as the offset value increases. From this comparison it can be inferred that the engine is one of the main players, in terms of internal energy absorption, during the deformation of the whole vehicle. For the "0 mm" and "150 mm" study, the internal energy values are very similar to each other; this is due to the fact that engine and bollard make direct contact. For the "150 mm" case, the maximum internal energy value results to be 2000 J lower than for the centered bollard.

For the "400 mm" case, the internal energy has a value of 36 kJ, which is less than half of the "0 mm" case (87 kJ). This significant difference is caused by the fact that the engine impacts against the bollard only with the right side. For the last case, the internal energy shows a maximum value of an order of magnitude lower than for the other three studies. The only deformations suffered by the engine are caused by the right longitudinal beam, which, bending in the XY plane, hits the engine on the right side.

Figure 81 shows the relative displacements of the deformed elements with respect to the undeformed engine surface; these displacements correspond to the plastic deformation that the component undergoes for each case and, consequently, the relative absorption of internal energy. The maximum displacement for the "0 mm" is 97 mm and affects the central elements of the front side. In the study with the bollard positioned at "150 mm" the maximum displacement (106 mm) among the four cases is recorded. The elements affected by the maximum deformation are the ones of the right edge of the front side. In fact, the bollard collides with the right area of the engine, which is also pushed forward by the cargo and further crushed against the bollard. This additional push accentuates the deformation of the elements in particular those of the right edge. Since the edge belongs to the deformable part (part 1 - Figures 79) it is subjected to considerable deformations. In the "400 mm" simulation, there is a maximum deformation of 54 mm on the right flank of the engine. In this event, the bollard, after hitting the longitudinal beam, slides between it and the right side of the engine deforming it and stops on the front axle. The deformation in this case affects a smaller area, and the maximum value is about half that of the two previous cases. This difference justifies the reduction in magnitude of the internal energy. As for the last case, the deformation is observed on the right flank in a very localized area. The deformation is caused by the bending of the longitudinal beam that impacts with the right flank of the engine. The maximum relative displacement is 39 mm, and the affected area is extremely small. This justifies the low value recorded for the internal energy.

### Front longitudinal beams

Figure 83 shows the internal energy absorption from the front longitudinal beams for the four bollard offset cases; Figure 84, on the other hand, shows an image of the front longitudinal beams in the undeformed and in the deformed condition and the relative effective plastic strains recorded for each case. It was decided to study the plastic strain for this component since they are modeled as shell elements and the material assigned is steel whose properties are shown in Figure 78.

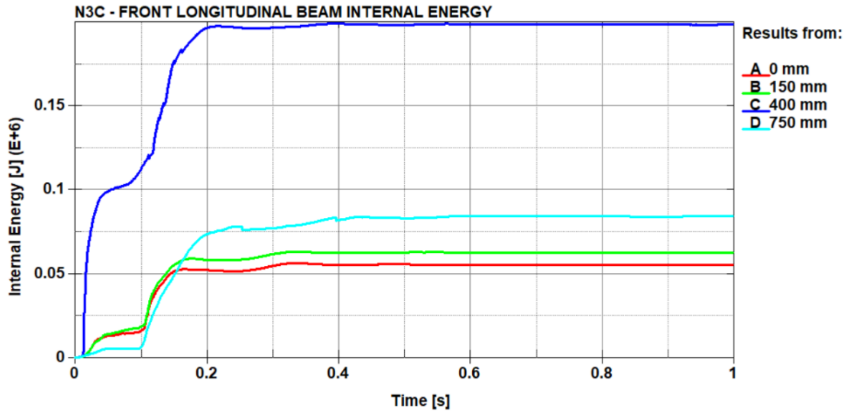

*Figure 83 - Front longitudinal beams - internal energy comparison*

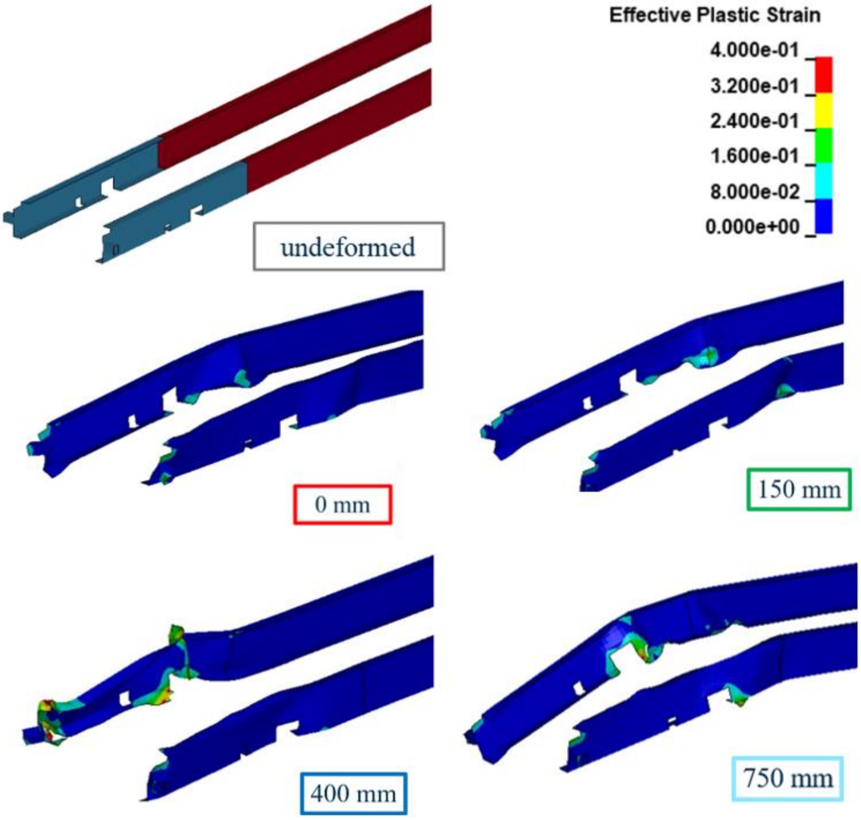

*Figure 84 – Front longitudinal beam effective plastic strain*

From Figure 83 it can be seen that for the "400 mm" case, the internal energy absorbed by the front longitudinal beam reaches a maximum value of 200 kJ. This value is the highest contribution of internal energy absorbed by a component among all four simulations. In fact, its value is more than double of the maximum value recorded for the internal energy absorbed by the engine ("0 mm" - 87 kJ). This information, correlated with the high peak of X Force observed for the impact between the front longitudinal beam and the bollard, shows that this case is extremely penalizing for the latter. It is also confirmed by Figure 84 where the maximum plastic deformation occurs in the area of the front longitudinal that is compressed by the collision.

As for the "0 mm" and "150 mm" studies they are similar to each other in terms of both internal energy and deformation; the maximum values of internal energies recorded are respectively 55 kJ and 63 kJ. The "150 mm" case shows values of internal energy slightly higher than "0 mm" simulation caused by the greater deformation of the elements; in fact, more light blue and green areas can be observed in the junction between the front longitudinal beams and the longitudinal beams. This difference is consequent of the off-centered bollard that pushes the engine against the left longitudinal beam increasing its overall deformation.

The study with the bollard displaced by 750 mm presents a maximum internal energy value of 85 kJ, which is between the "400 mm" and "150 mm" cases. It is an order of magnitude higher than the one calculated for the engine internal energy in the same simulation. The longitudinal beams are, in fact, deformed by the progressive rotation of the front axle and of the engine around the Z axis. The greatest deformations are concentrated in the area in front of the junction zone, in particular where a rectangular-shaped notch is located.

### Fan and filter

Figure 85 shows the internal energy related to the deformation of the fan and filter for the bollard offset cases; on the other hand, in Figure 86, the undeformed and deformed shape of the fan and filter FEM model can be observed with the relative effective plastic strains recorded for each case. The deformation has been measured in terms of effective plastic strain since the fan and the filter is modeled with shell elements and the aluminum is the imposed material (Figure 78).

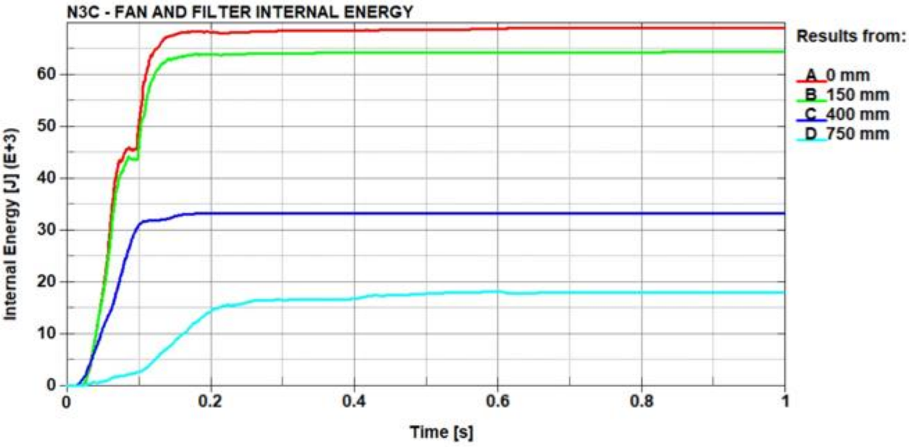

*Figure 85 - Fan and filter - internal energy comparison*

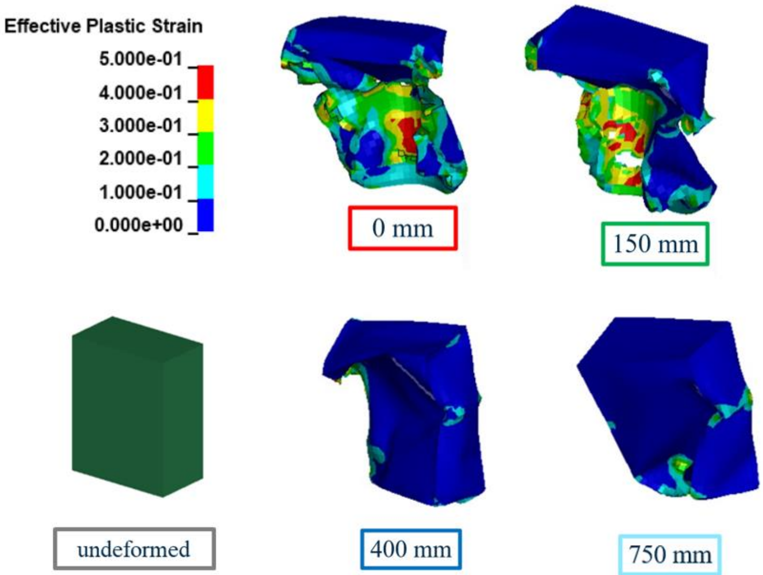

*Figure 86 – Fan and filter effective plastic strain*

Since the fan and filter is located between the front bumper bar and the engine, it comes into direct contact with the bollard during both simulations with offset equal to 0 mm and with offset equal to 150 mm. In these two cases it undergoes very similar deformations; the main difference is that in "150 mm" the elements affected by the maximum plastic strain value (red areas) are shifted to the right side and present in lower quantity than in the "0 mm" case. This difference is reflected by the internal energy value: the trend of the two curves and their corresponding maximum value are similar and equal to 56 kJ for "0 mm" and 48 kJ for "150 mm". As for the "400 mm" study, the deformation is caused by the collision with the frontal cross member, positioned perpendicular to the front longitudinal beams; it is detached from the right longitudinal beam by the impact with the bollard, and produces the deformation of the fan and filter. In this case the deformation is less pronounced than in the first two simulations and the difference is also highlighted by the maximum internal energy value which is equal to 33 kJ. In the last case, the deformation of the fan and filter is the lowest recorded among the four bollard offsets, since neither the bollard nor the front cross member comes into direct contact with it; in fact, the observed deformation is caused by the marginal impact with the deformed front bumper bar.

### Front axle

This section will analyze the internal energy absorption of the front axle and the related plastic strain for the four studied cases. The front axle is a component with high stiffness and it is modeled as a solid steel element. Figure 87 shows the curves related to the internal energy while Figure 88 shows the undeformed and deformed conditions and the relative plastic strain of the front axle.

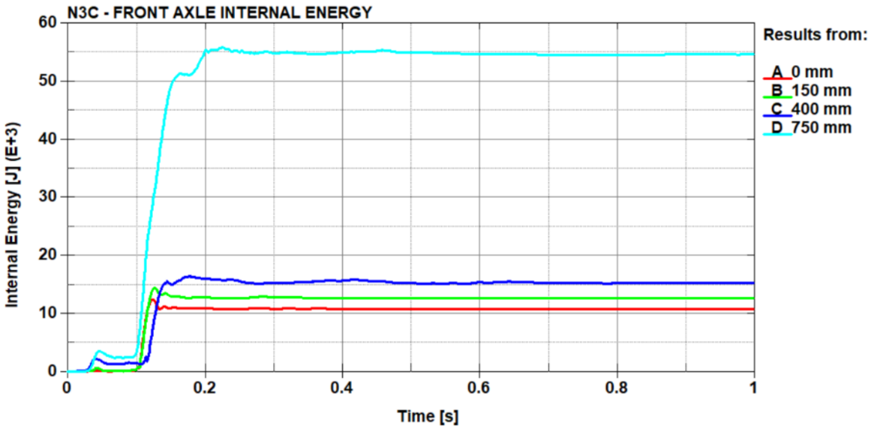

*Figure 87 - Front axle - internal energy comparison*

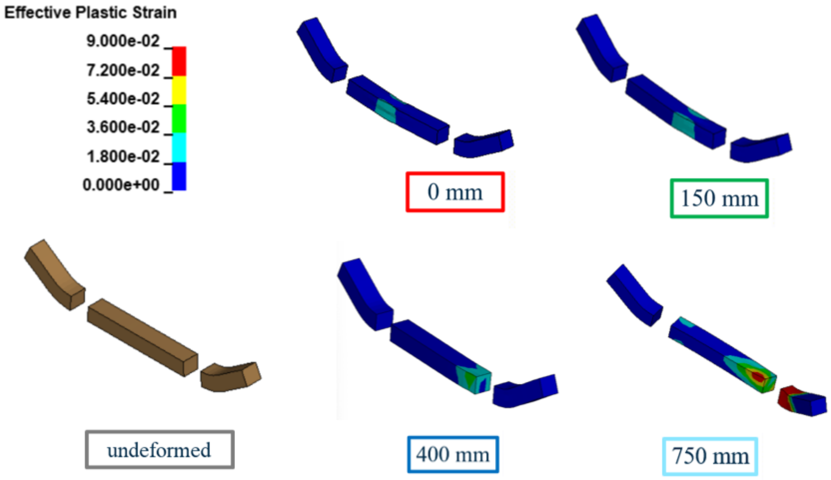

*Figure 88 - Front axle plastic strain*

It can be seen from Figure 87 that the internal energy absorbed by the front axle tends to increase in value as the bollard offset increases. For the "0 mm" and "150 mm" cases, the curves appear to be very similar to each other; the maximum values are lower than 2% of the total energy of the respective cases. In these two cases the plastic strain shows low values although the front axle and the bollard get into direct contact. This is due to the fact that the collision occurs after the entire vehicle front part (front bumper bar, front cross member, fan and filter~~,~~ and the engine) has already collided against the bollard and the deformation has almost absorbed the entire impact. For the "400 mm" case, the internal energy and plastic deformation are slightly higher since the bollard, after deforming the front longitudinal beam, slides between it and the engine and stops in contact with the front axle. Nevertheless, the internal energy value is the 3% of the total energy since the impact with the front longitudinal beam has absorbed almost the entire collision. In the simulation with the bollard displaced of 750 mm from the centered condition the highest values of internal energy are recorded with a maximum value of 55 kJ; consequently, in this case it is also present the maximum value of plastic strain. This high plastic strain is given by the fact that, with this offset, the impact with the bollard is absorbed almost completely by the deformation of the front axle and the longitudinal beams.

## Front bumper bar

Figure 89 shows the graphs of internal energy for the front bumper bar and Figure 90 shows the relative plastic strain values for each case analyzed. The front bumper bar is modeled with shell elements and the material assigned is steel (Figure 78).

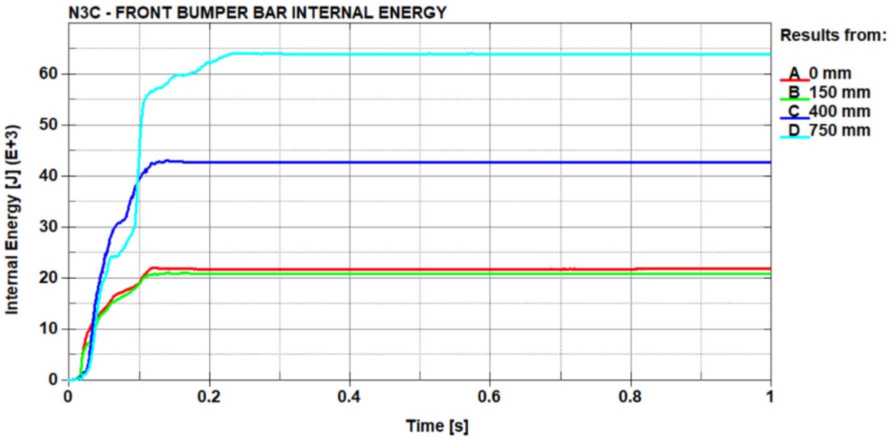

*Figure 89 - Front bumper bar - internal energy comparison*

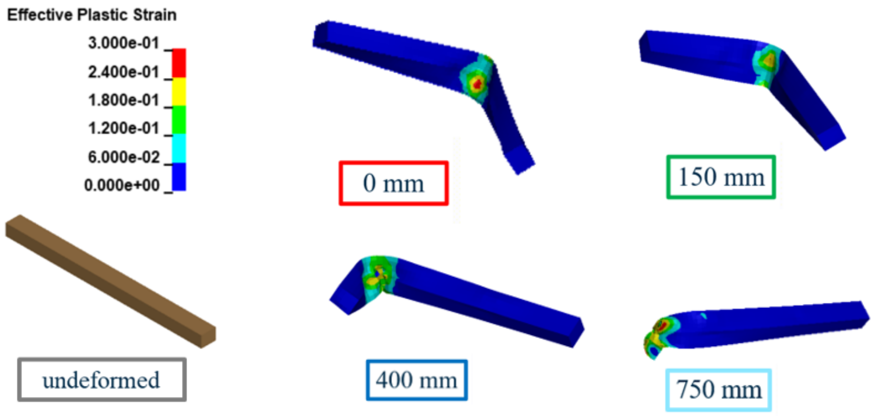

*Figure 90 - Front bumper bar plastic strain*

In Figure 89, it can be seen that for the "0 mm" and "150 mm" cases, the internal energy curves are very similar and almost overlapping; although the front bumper bar enters in to direct contact with the bollard in both of the two simulations, the maximum value is less than the 4% of the total energy in the respective cases. This indicates how the front bumper bar, despite the deformation, marginally affects the impact absorption. As for the other two studies "400 mm" and "750 mm", the internal energy is significantly higher. Especially for the "750 mm" case the internal energy reaches a maximum value of 64 kJ. The main difference between these two simulations and the first two is the fact that the high offset value of the bollard dose not causes only the crush of the front bumper in the impact area, but also the rotation around the Z axis and around its own longitudinal axis of the bar. Consequently, it can be observed how the deformation, caused by the rotation, greatly influences the absorption of the impact.

### 4.2.4 Statistical analysis of the results

The Table 13 shows the maximum values of the internal energy of the components of each case; and Table 14 the percentage of the component's internal energy in relation to the total internal energy. As mentioned in the beginning of the chapter 4.2.1, are studied only the components that have an internal energy value greater than the 5 % of the total internal energy, in one or more of the cases. In the simulations where the internal energy is less than 5 %, the value is not included for an easier understanding of the analysis.

*Table 13 – Components internal energy maximum values*

| Component | 0mm | 150mm | 400mm | 750mm |
|---|---|---|---|---|
| Total | 617 kJ | 580 kJ | 534 kJ | 488 kJ |
| Engine | 86.8 kJ | 76.9 kJ | 36.4 kJ | - |
| Front long. beam | 55.4 kJ | 62.7 kJ | 199 kJ | 84.7 kJ |
| Fan and filter | 69.1 | 62.7 | 33 | - |
| Front axle | - | - | - | 54.7 kJ |
| Front bumper bar | - | - | 42.8 kJ | 64 kJ |

*Table 14 – Percentual influence of components with respect to the total internal energy*

| Component | 0mm | 150mm | 400mm | 750mm |
|---|---|---|---|---|
| Total | - | - | - | - |
| Engine | 14% | 13.3% | 6.8% | - |
| Front long. beam | 9% | 10.8% | 37.3% | 17.4% |
| Fan and filter | 11.2% | 10.8% | 6.2% | - |
| Front axle | - | - | - | 11.2% |
| Front bumper bar | - | - | 8% | 13.1% |

Figure 91 shows the values shown in Table 14 with the use of a histogram for easier evaluation of the data; while Figure 92 the values recorded in Table 15.

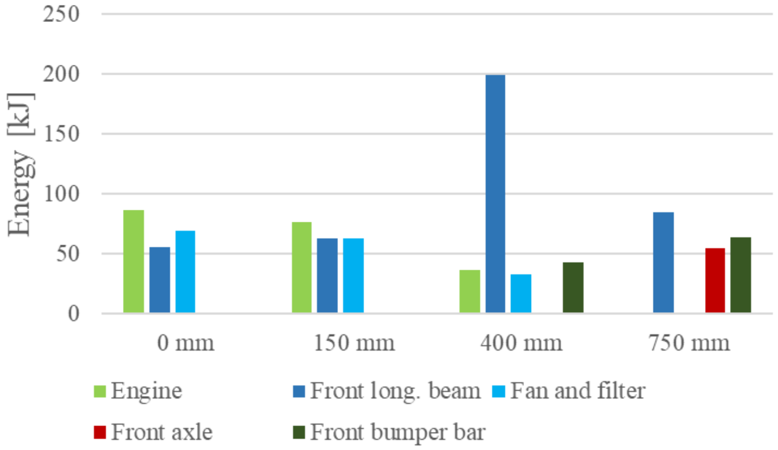

*Figure 91 – Components maximum internal energy values*

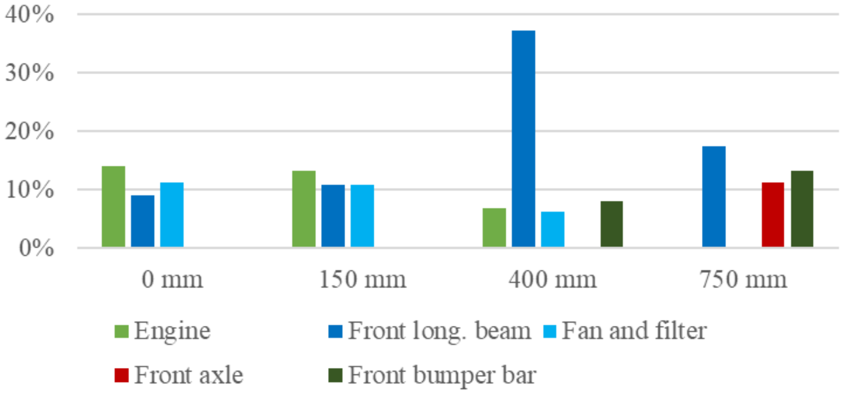

*Figure 92 – Components percentual influence on total internal energy*

Regarding the "0 mm" case, the element that mostly affects the internal energy is the engine followed respectively by the fan and filter and the front longitudinal beam. As for the simulation with 150 mm of bollard offset, the values of the components are similar to those of the "0 mm" case. The main difference is observed in the fact that longitudinal beams and the fan and filter present equal value to each other. In this case the percentage influence of the front longitudinal beams is greater than the study on "0 mm" due to the greater deformation caused by the rotation of the engine. In the "400 mm" simulation there is the highest value in terms of percentage contribution on the total internal energy calculation. In fact, the internal energy of the front longitudinal beams is greater than 35% of the total value while the engine and the fan and filter slightly exceed 5%. These results show that the front longitudinal beams are the structural elements that can absorb the bollard impact the most among all other components. In the last case the front longitudinal beams appear to be the element with the greatest influence on the total internal energy calculation; the influence of the front axle and of the front bumper is between 10% and 15%. The latter has a quite high percentage of influence similar to that shown by the engine in the "0 mm" case.

# Conclusions

As for the comparison between the LS-Dyna software and Europlexus, that is shown in the first two chapters of this thesis, it has been focused on contact formulations (SOFT) and contact stiffness scale factors (SFS) and their influence on explicit FEM simulations. This study was done to better investigate how the contact algorithms in LS-Dyna and in Europlexus works in order to understand similarities and differences. The results of this analysis showed how the contact stiffness scaling factors, when varied from their default value, can greatly affect the results especially in cases where low elements deformations are involved. In the case showed in Chapter 2, the contact stiffness scale factors had a significant influence on the internal energy, the kinetic energy, the momentum and time step of the simulation. It was also observed that by increasing the SFS values, the differences with the results obtained in Europlexus tend to decrease. Therefore, it can be concluded that, thanks to a deep understanding of the contacts methods in LS-Dyna, and consequently acting on parameters such as the SFS ones, which are often left at the default value, the simulation outputs can be greatly influenced, according to the different conditions and requirements.

On the other hand, with regard to Chapter 3, it could be inferred that the contact stiffness scale factors turn out to be irrelevant in a tube shock-crush case against a rigid wall, that involves considerable elements plastic deformations. In this case, similar and consistent results were obtained between those calculated with LS-Dyna and those with Europlexus.

Chapter 4 regards the analysis of the generic vehicle model of category N2/N3 in terms of reliability in impact simulations with safety barrier. Specifically, the model was properly modified to match with the N3C category and to undergo a second validation by reproducing an experimental test. This validation involved the vehicle model to an impact with a bollard at 80 km/h. A good correlation between the results was generally observed; the main difference is related to the behavior of the cabin of the FEM model compared to that of the experimental case. This discrepancy was attributed to the early failure of the connections between the cabin and frame. Therefore, this issue was pointed out to the model developers to further improve the FEM modeling even for high-speed impacts.

In the sensitivity analysis on the influence of the bollard position, it was possible to analyze in detail the influence of the main structural components of the vehicle in absorbing the barrier impact. Special attention was focused on the normal force transmitted to the bollard during the impact. It was observed that the most penalizing cases for the barrier are the case with the centered bollard and the case in which the off-center bollard makes direct contact with the vehicle's longitudinal beam ("400 mm" case). It is necessary to point out that the front longitudinal beams are the structural elements that can absorb the bollard impact the most among all other components and at the same time are they are cause of the highest peak force exchanged with the barrier. Finally, it was noted that the position of the cargo and its mass also greatly influence the peak forces exchanged with the bollard. This last point could be the starting topic for the continuation of this research.

# References

[1] European Commission's Joint Research Centre,
<https://joint-researchcentre.ec.europa.eu/index_en>

[2] Europlexus,
<http://www-epx.cea.fr/>

[3] V. Karlos and M. Larcher, "Guideline: Building Perimeter Protection: Design recommendations for enhanced security," European Commission, Ispra, Italy, 2020.

[4] LS Dyna support, "Contact Modelling in LS-Dyna",
<https://www.dynasupport.com/tutorial/ls-dyna-users-guide/contact-modeling-in-ls-dyna>

[5] Emily Owen, "Webinar: LS-DYNA Introduction to contacts",
<https://www.oasys-software.com/dyna/wp-content/uploads/2020/01/Intro-to-Contacts.pdf>

[6] J. Hallquist, "LS DYNA Theory Manual", Ansys, 2003

[7] LS Dyna support, "Contact Types",
<https://www.dynasupport.com/tutorial/contact-modeling-in-ls-dyna/contact-types>

[8] LS Dyna support, "Mass Scaling",
<https://www.dynasupport.com/howtos/general/mass-scaling>

[9] "SVS FEM",
<https://www.svsfem.cz/>

[10] M. Šebík and Zuzana Kodajková, "Generic vehicle model N2A & N3D", SVS FEM s.r.o., Brno, Czech Republic, 2023.

[11] CTS service, "Crash test Renault Midlum vs. Bollard: PAS 68 / IWA 14-1", <https://www.youtube.com/watch?v=Gwt73tduTZM>

[12] "Tracker Video Analisys and Modeling Tool"
<https://physlets.org/tracker/>

[13] FAAC, "FAAC J355 M50",
<https://faac.it/faac-j355-ha-m50-bollards-2/>

[14] DYNAmore GmbH, DYNAmore Swiss GmbH, DYNAmore Italia S.r.l., 2023
<https://www.dynamore.de/en/products/pre-and-postprocessors/prepost>

[15] Amco Les Escamotables, "ALE F16-100-C50"
<https://assets.ctfassets.net/wutvz7hlq4gn/3X57kv4d3RlT2zS1qmP973/53607f7cf513345bfad3ba7cd345b5ca/FT_ALE_F16-100-C50.pdf>